UNIVERSITY OF CALIFORNIA
RIVERSIDE

Theranostic Window to the Brain for Multispectral Light Delivery and Microcirculation Imaging

A Dissertation submitted in partial satisfaction
of the requirements for the degree of

Doctor of Philosophy

in

Mechanical Engineering

by

Nami Davoodzadeh

March 2020

Dissertation Committee:
Dr. Guillermo Aguilar, Chairperson
Dr. Lorenzo Mangolini
Dr. Suveen Mathaudhu

The Dissertation of Nami Davoodzadeh is approved:

_____

_____

_____

Committee Chairperson

University of California, Riverside

Acknowledgments

I am grateful to all those with whom I have had the pleasure of working on this and other related projects. Each of my Dissertation Committee members has provided me with extensive professional guidance and has taught me a great deal about scientific research. I would especially like to thank Dr. Guillermo Aguilar, the chairman of my committee. As my teacher and mentor, he has taught me more than I could ever give him credit for here.

I would like to thank my parents, whose love and guidance are with me in whatever I pursue. They are the ultimate role models.

ABSTRACT OF THE DISSERTATION

Theranostic Window to the Brain for Multispectral Light Delivery and Microcirculation Imaging

by

Nami Davoodzadeh

Doctor of Philosophy, Graduate Program in Mechanical Engineering
University of California, Riverside, March 2020
Dr. Guillermo Aguilar, Chairperson

Interest in using optical methods in the development of noninvasive clinical diagnostic and therapeutic techniques for brain diseases has widely increased due to their simplicity, safety, and affordability. The main limitations of light-based techniques used for brain theranostics are the strong light scattering in the scalp and skull, which cause decrease of spatial resolution, low contrast, and small penetration depth. To address this challenge, our group has previously introduced a transparent nanocrystalline yttria-stabilized-zirconia (nc-YSZ) cranial implant material which implant possesses the mechanical strength and biocompatibility that are prerequisites for a clinically-viable permanent cranial implant for patients.

This implant possesses the mechanical strength and biocompatibility that are prerequisites for a clinically-viable permanent cranial implant for patients. A potential benefit of this optical window is an improvement of light-based therapeutic techniques that rely on sufficient light penetration to a target embedded in tissue such as photobiomodulation, photodynamic therapy, and optogenetics. Another application of this optical window is noninvasive visualization of brain blood vessels, hematomas, and small pathologic structures (including cancerous growth) with high resolution. This is important for diagnosis and treatment of many diseases such as tumors of the brain, vascular pathologies, and so forth. In this dissertation, I investigated (1) characteristics and durability of transparent nc-YSZ implants; (2) feasibility of chronic brain imaging through the implant; (3) multimodal imaging across the implant to generate an arteriovenous vascular map; (4) through-scalp VIS-NIR light delivery and microvascular imaging.

Table of Contents

List of Figures

Chapter 1. Introduction

From the deep blue to the near-infrared (NIR) is the region among the wide spectrum of electromagnetic waves that we know as light. This delicate region has a distinct advantage for interrogating biological tissue due to its unique photon energy range of 0.5–3 eV. At energies above this range, C–C and C–H bonds dissociate and ionization can occur, while at energies below this range, water absorption dominates the transmittance, preventing any specific targeting of molecules[1]. The noninvasive interactions with tissue of photons within this energy range have been used in numerous approaches to assess brain health and treat its diseases. Some of these treatment practices have been used in clinical applications such as photobiomodulation (for wound healing, tissue repair, anti-inflammatory therapy[2], and chronic traumatic brain injury[3]) and photodynamic therapy (PDT) which is now clinically approved to treat brain cancer[4]. Optical dissection of brain circuits methods, known as optogenetic therapies, have resulted in the treatment of Parkinson[5], cocaine addiction[6], depression[7], chronic pain[8], and laryngeal paralysis[9] in animals and may one day be translated for use in humans. The poor penetration depth of light, particularly in the visible range, has limited the clinical applications of these photosensitizer activation-based methods. For instance, PDT is currently only used for the treatment of superficial lesions, or of lesions accessible during surgery or through endoscopy[4]. Therefore, bio-optical technologies for adequate delivery of light to the brain have been rapidly advancing[10].

Light-based techniques have also been used for brain health assessment. Numerous methods have been widely developed and applied in various brain disease diagnostics. Imaging of brain microcirculation (i.e. blood flow in vessels <150 μm in diameter), which plays a critical role in the physiological processes of tissue oxygenation and nutrient exchange, has enabled us to noninvasively extract morphological and functional information[11,12]. Morphological information provides vessel density, perfusion rate, vessel diameter, and dynamic measurements of microcirculatory blood flow velocity and blood cell concentration[11], while functional data provides information on blood oxygenation, changes in metabolism, regional chemical composition, etc[12]. Various imaging modalities have been developed which are capable of measuring blood flow. Although they have resulted in a number of discoveries, there are notable drawbacks which should be considered in developing a scalable and real-time method for routine and long-term brain microcirculation monitoring. Indocyanine green video angiography (ICGVA) requires injection of dyes and cannot provide continuous assessment of vessel perfusion[13,14]. Optical coherence tomography (OCT)[15], photoacoustic imaging (PAM)[16], and fluorescence microscopy approaches like confocal microscopy or the two-photon variant[17] are based on laser scanning, which is limiting to the temporal resolution and field of view[18], although recent technical improvements in OCT and PAM have been reported which provide sufficient temporal resolution for epileptic seizure monitoring[19–21]. Fast full-field laser Doppler perfusion imaging (ffLDPI)[17] cannot

simultaneously provide microvascular structural and functional information due to lack of adequate spatiotemporal resolution[22].

Analyzing intensity fluctuations in scattered laser light, i.e. speckles, has been reported to provide useful biological information. Laser Doppler, photon correlation spectroscopy, and time-varying speckle operate by analyzing speckles from a single point in the flow field and thus require some form of scanning to produce velocity maps, adding time to the procedure[17]. Laser speckle imaging (LSI), on the other hand, is a full-field, real-time, noninvasive, and noncontact imaging method which is sensitive to both the speed and morphological changes of the scattering particles, and is capable of mapping relative velocity in flow fields such as capillary blood flow[17]. By utilizing spatio-temporal statistics of speckle, LSI produces blood flow maps in a fraction of a second without the need for scanning, making it a true real-time technique[17]. Like LSI, ffLDPI can provide full field information in a short time, but LSI has the advantage of being relatively simple and inexpensive since it does not require a high-speed imaging array. This make LSI a scalable and compatible modality which has been used in wearable and routing brain monitoring applications[23], solely or coupled with other imaging modalities[17].

Proving theranostic optical access to the brain is complicated due to the static and dynamic effects of optical scattering and absorption by the inhomogeneous skull and scalp tissues. These effects drastically limit the achievable imaging field of depth and resolution. Therefore, brain imaging has been predominantly demonstrated in rodent

open-skull and thinned skull models. Likewise, in our research team prior studies we have found that optical imaging through the intact skull of mice diminishes detection of the intrinsic optical signals[24–27]. Moreover, the optical properties of the inhomogeneous cranial bone overlap with those of brain tissue and jointly these factors decrease the accuracy and reliability of the data. Studies in the literature have addressed this optical barrier with various approaches including imaging the brain directly with an opened skull[28], thinned and polished skull preparations[29,30], temporary optical clearing of the skull using optical clearing agents[31–33], and implanting glass or PDMS windows[34,35]. Glass and PDMS windows are powerful research techniques, but are not appropriate for human application as permanent cranial implants for patients. Like skull thinning and polishing techniques, glass-based windows compromise protection for the brain due to the extremely low fracture toughness of typical glasses (KIC = 0.7-0.9 MPa m1/2)[36] which increases potential for catastrophic failure by fracture, while the effect of skull optical clearing agents for long-term use on human skull is still unknown[24]. A number of biomedical considerations including biocompatibility, mechanical strength, and ageing should be examined in order to create an optical window for eventual clinical application[24]. Conventional cranial prosthesis including titanium, alumina, and acrylic[37], have not provided the requisite combination of transparency and toughness required for clinically-viable transparent cranial implants. To address this challenge, our group has previously introduced a transparent nanocrystalline yttria-stabilized-zirconia cranial implant material, which possesses the mechanical strength and biocompatibility which

are prerequisites for a clinically-viable permanent cranial implant for patients[24–27,38–46]. This implant has been referred to in the literature as the "Window to the Brain" (WttB) implant. Figure 1.1 shows an illustration of implant placement envisioned in eventual human application providing theranostic optical access for light delivery and high resolution and chronic brain monitoring without scalp removal.

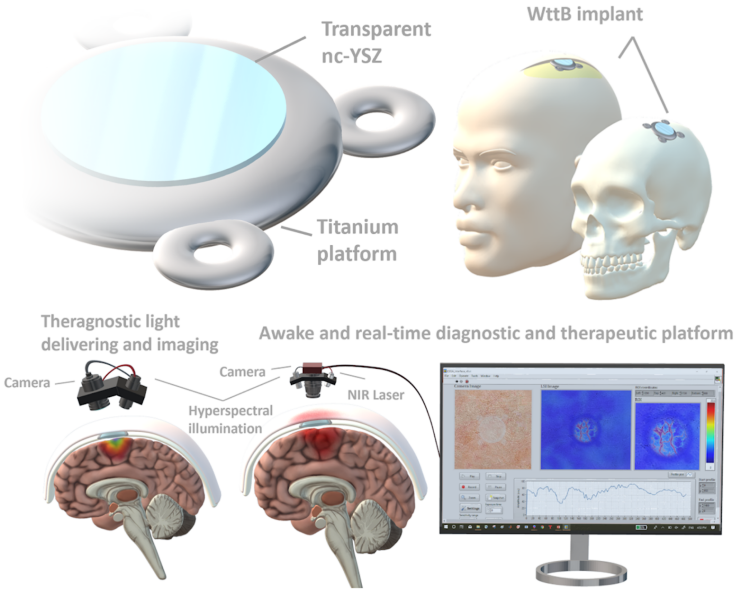

Figure 1.1. Illustration of the Window to the Brain cranial implant concept. The implant will be attached to the skull beneath the scalp. The application of optical clearing agents will allow for optical transmission to and from the brain without scalp removal.

My preliminary studies, reported in detail in chapter 2, have established the essential feasibility of the WttB concept by demonstrating the excellent ageing resistance of nc-YSZ implants and showing they can withstand long-term implantation conditions without exhibiting change in optical and mechanical properties.

We have previously shown that this implant allows for increased imaging depth and contrast compared to the native skull for optical coherence tomography (OCT)[39]. In chapter 3, I sought to expand upon previous indications that this WttB implant allows for improved LSI spatial resolution of brain blood flow compared to imaging through the native skull in mice[25]. In addition, our previous OCT study was acute in nature and did not assess whether imaging quality across the WttB implant is maintained over time. Therefore, Chapter 3 demonstrates repeated brain imaging using both OCT and LSI across the WttB implant over 4 weeks to determine if the WttB implant allows for chronic OCT imaging.

In chapter 4, I demonstrated that LSI combine with multispectral reflectance imaging (MSRI), allows for distinction between veins and arteries in the vascular flow maps produced by LSI. This creates an arteriovenous vasculare map, vein-artery separation, information which is of value scientifically and medically. By applying this combined technique to mouse cerebral vascular network in vivo, I compared imaging through the skull, to the brain directly through a craniectomy, and through a transparent cranial “Window to the Brain” (WttB) implant.

Some spectral regions in the Near Infrared (NIR) spectral range (800 to 2500 nm) offers low scattering and absorption as well as a deep penetration depth in tissue media[47–49]. Because of these features, some spectral windows within the NIR wavelength range have shown promising results for brain studies, including deep imaging, diagnostics and therapeutic applications in brain diseases[50–53]. Different optically

transparent spectral windows for head tissues have been identified within the NIR spectral range. These wavelength windows avoid light attenuation by the tissue due to water absorption peaks located at 1450 nm and 1940 nm[54–56]. In chapter 5, I reported on the enhancement in optical access provided by the transparent YSZ implant for brain studies in the NIR wavelength range. Because this cranial implant is sought as a means to obtain optical access for post-operatory and prolonged diagnostics and/or therapy purposes, scalp scattering must be overcome. In this context, I also evaluated the use of optical clearing agents (OCAs) in the scalp, particularly their effects on the optical transmittance in the NIR spectral range.

Visible wavelength range also shows promising features to facilitate various photosensitizer activation-based therapies. Photobiomodulation (600-1064 nm)[1,2,57–59], PDT(405-900 nm, mainly in red range)[4,60], optogenetic (400-630 nm)[5,9,61] are a few examples of optical techniques that could benefit from the improved light delivery offered by WttB implant and scalp optical clearing. In chapter 6, the enhancement in optical access to the brain using scalp optical clearing and WttB implant is evaluated through comparing *ex vivo* optical transmittance measurements and *in vivo* through-scalp brain hemodynamics imaging in mice.

Chapter 2. Characterization of transparent nanocrystalline yttria-stabilized zirconia implants

Background

Polycrystalline zirconia-based ceramics have become the focus of recent investigations because of their unique combination of properties. Their high hardness and chemical inertness (high temperature stability and corrosion resistance) make them important target materials for various applications. Well-proven biocompatibility, low thermal conductivity, and high oxygen diffusivity[62] have made zirconia-based ceramics a favorable option for biomedical applications. By decreasing the grain size of the polycrystalline ceramics to nano-scale, novel characteristics such as high density (low porosity), transparency/translucency, and high refractive index and Abbe number have been reported.[63–67]

Transparent nanocrystalline yttria-stabilized zirconia (nc-YSZ) ceramics developed by our research group as biomedical transparent cranial implants aim to provide chronic optical access to the brain[24,68–73] in order to facilitate the diagnosis and treatment of neurological diseases.[39] A recent study also demonstrated the ability of this implant to improve ultrasound imaging of the brain compared to imaging through skull.[40] The transparency of the nc-YSZ is achieved by using ultra-fine yttria-stabilized zirconia (YSZ) powder and an innovative ceramic processing method, current-activated pressure-assisted densification (CAPAD), leading to transparent nc-YSZ ceramics.[74] CAPAD enables reduction of the number of pores as well as reduction of their

dimensions to nanometric scale and at these length scales, porosity is sufficiently small to minimize scattering in the spectral range of interest for medical imaging and laser therapies of the brain.[63]

Although zirconia-based implants have been known for their excellent mechanical properties, the in vivo application was found to be affected by long-term failures for some samples with micrometric grain sizes, due to low temperature degradation (LTD). By contrast, YSZ with nanometric size grains are significantly more resistant to LTD.[66] LTD is due to a crystal phase transformation from tetragonal to monoclinic, which is associated with a volume increase of about 4 - 6%.[75] This expansion induces localized compressive stresses and eventually microcracks around the transformed zirconia particles.[76] These microcracks propagate through the sample bulk, and internal defects such as pores and crack surfaces.[77] Under such conditions, the material loses its cohesion and mechanical properties. Therefore, small amounts of porosity contributes to enhance the nucleation and propagation of the monoclinic phase, so the use of very dense implants is required to reduce the transformation rate.[76,78]

As a modest amount of transformation can change optical characteristics such as transparency, in Chapter 2, we investigated the optical properties of transparent nc-YSZ ceramics with different stabilizer contents (Yttria dopant levels) of 3, 6 and 8 mol% before and after extended accelerated ageing treatments. Further, because mechanical properties become compromised when LTD occurs, we also compared the hardness of our samples before and after the accelerated ageing treatments. The treatment simulates

in vivo ageing, according to the ISO 13356:2008 recommendations[77,79] (i.e. autoclave processing at 134 °C at a water partial pressure of 2–3 bar).

To my knowledge, this is the first study to compare the LTD of transparent nanocrystalline YSZ with differing stabilizer content (3, 6, and 8 mol% Yttria). Most studies conducted on LTD of zirconia-ceramic have involved opaque micrometric-grained YSZ. The objective of this current study is to assess the LTD of new nc-YSZ through simulated ageing protocols, to model how the WttB implant will perform optically and mechanically over decades of ageing in the body.

Methods

Implant fabrication and preparation

Commercial (Tosoh USA Inc., Grove City, Ohio) nanocrystalline 3YSZ, 6YSZ, and 8YSZ powders (respectively doped with 6, 12, and 16 mol% $YO_{1.5}$ nc-YSZ) with reported crystallite sizes of 55 nm, were densified via the CAPAD technique, to produce transparent Yttria-stabilized zirconia ceramics.[80] In the literature, this technique is often called spark plasma sintering (SPS). We used CAPAD here to emphasize the fact that it is complementary contributions of the current and an applied pressure that makes it successful.[80] During the fabrication processes of all samples for this work, 1.5000g ± 0.0001g of starting powder was poured into a graphite die of inner diameter measuring 19 mm, and secured between two plungers with the same outer diameter. The die, plungers, and powder assemblies were placed into the CAPAD apparatus and secured

between two graphite spacers and copper electrodes, all enclosed within a vacuum chamber. A vacuum of 1×10^{-3} Torr was attained in all cases.

All powder compacts were pre-pressed to a maximum load of 30 kN, applied linearly, to produce a nominal compressive pressure of 106 MPa on the sample, and held for 2 minutes to achieve a green body of appreciable density. The load was then released, and the green body subjected to another uniaxial compressive stress of 106MPa over a 3-minute interval. Once the set-point temperature was reached, a second load ramp ($kN.min^{-1}$) was applied. This ramp bringing the uniaxial pressuring on the sample up to 141 MPa, was maintained for 10 minutes, the duration of processing, and thereafter linearly released. In addition to the aforementioned load parameters, the green pellet was simultaneously heated to high temperature by applying electric current through the die and plunger assembly, consequently creating joule heating. All samples were processed at 1200 ℃, with an average heating rate of approximately 160 ℃/min, from room temperature, and held for 10 minutes.

The density of the samples was measured using the Archimedes method, and the ASTM standard designated B962-13 was followed.[81] Grain size measurements of the bulk sample made from fracture surfaces were evaluated using SEM.

The samples thicknesses were reduced by polishing with 30-micron diamond slurry on an automatic polisher (Pace Technologies, Tucson, Arizona USA). The two faces were then polished using progressively finer abrasives (from 30 μm diamond slurry down to 0.2 μm colloidal silica slurry) to reduce light scattering by the implant surfaces and

thus increase transparency as well as to create a uniform surface area between different samples. As ageing begins at surface and propagates into bulk, surface area is an important factor to control between samples when comparing ageing results. After preparation process, the polished samples underwent ageing tests.

Ageing test

The test for simulating in vivo ageing, per the ISO 13356:2008 recommendations (ISO, 2008), uses hydrothermal treatment at 134 °C, at a steam partial pressure of 2–3 bar which is known as autoclave processing. As seen in Figure 2.1, the samples were placed in a steel pressure chamber, and saturated high-pressure steam was generated by a boiler and sent to the sample chamber through an electronic valve. An electric heating jacket surrounded the chamber to prevent steam condensation and stabilize the temperature at 134 °C. Two K-type thermocouples were used to measure the sample chamber and the boiler temperature, and an electronic pressure sensor was connected to the pressure chamber. A microcomputer (Raspberry Pie 3) coupled to the sensors controlled the heating jacket power and the valve status. The ageing treatments were performed in cycles of 5, 10, 10, 25, 25, 25 h, for a total of 100 h for each sample. At the end of the treatments, the samples were cooled down to room temperature and dried.

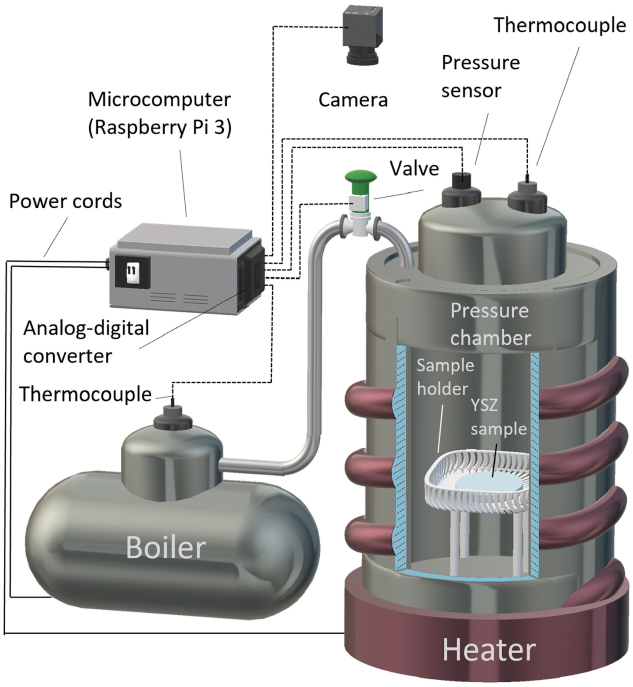

Figure 2.1. Hydrothermal treatment experimental setup schematic. Samples were placed inside a pressure chamber. Thermocouples and a pressure sensor coupled to a microcomputer maintained the temperature and pressure at 134°C and 2-3 bar.

Material characterization

X-ray diffraction (XRD) analysis was used to detect any phase transformation due to the ageing treatments (Figure 2.2(a)). Due to its simplicity, this technique has been considered as a first step to investigate the ageing sensitivity of a particular zirconia. However, this technique suffers some limitations, such as poor precision during the first stages of ageing (which have also been reported with a much higher sensitivity using grazing incidence angles of 1–5° (2θ)),[77,82] as well as the absence of local information on ageing processes.[83] Data were acquired on an X-ray diffractometer (PANalytical

Empyrean Series 2) using a step size of 0.03° (2θ) and an acquisition time of 5s per step. Various (hkl) planes were used to evaluate crystal structures, including cubic (111), tetragonal (101) and monoclinic ($\bar{1}11$ $\bar{1}11$ and 111) peaks at 30.2°, 30.2°, 28.2° and 31.5° (2θ), respectively. It must be noted that the distance between cubic and tetragonal peaks is smaller than the width of the peaks which makes them indistinguishable and detected at the same angle (30.2°).

Raman spectroscopy was additionally performed to investigate the impact of ageing on the phase transformation (Figure 2.2(b)). Raman spectroscopy has been reported to show higher sensitivity to the smaller trace of monoclinic phase,[84] associated with a higher lateral resolution than XRD. Micro-Raman spectrum were recorded by using a spectrometer (Horiba's LabRam) with acquisition time of 60s. The incident laser light with a wavelength of 532 nm was focused on the sample within a spot of 10 μm in diameter. Presence of monoclinic phase was assessed by comparing monoclinic doublet at 179 and 190 cm^{-1} in the Raman spectra.

Optical characterization

To qualitatively compare the transparency of the densified and polished 3YSZ, 6YSZ, and 8YSZ samples, photographs of a NBS 1963A resolution target (18 cycle/mm target, each black line width is 27.78 μm) through the ceramics were taken (Figure 2.3). For quantitative comparison, optical transmittance of the nc-YSZ samples were evaluated by optical spectrometry in visible and near-infrared light. The optical transmittance was measured using a white light source (HL2000 FHSA, Ocean Optics, FL) and a

spectrometer (SD2000, Ocean Optics, FL) in the 500-1000 nm wavelength range. The sampling system used for specular transmittance consists of a rail coupled with two fiber holders including collimating lenses (MP-74-UV, Ocean Optics, FL) with a wavelength range of 185-2500 nm. A space for placing the samples was incorporated on one of the fiber holders. After placing the sample, the fiber holders were fixed by screws to mitigate the effects of ambient light. A couple of multimodal optical fibers (P400-2-VIS-NIR, Ocean Optics, FL) were connected from the light source to the fiber holder and from the other fiber holder to the spectrometer. The spectra were acquired as an average of 10 measurements, with integration time of 100ms.

The normalized transmittance was calculated considering the ratio of light transmitted through the sample to the total light incident upon that sample (Eq. (2.1)).

$$T(\lambda) = \frac{S(\lambda) - D}{I(\lambda) - D} \tag{2.1}$$

Where T is transmittance, $S(\lambda)$ is the measured spectral intensity, $I(\lambda)$ is the total light incident, and D represents the reference in dark environment.

Mechanical characterization

To compare the mechanical properties between the pristine samples and aged samples, indentation tests were performed using a micro Vickers hardness tester (900-391A, Phase II Plus, NJ). The indentation was performed using loading force of 4.9 N and 15s duration. The instrument was re-calibrated before and after testing, by performing a series of indentations on a certified steel reference sample. The average

value and standard deviation of 10 indentations were calculated for each sample before and after the ageing treatments.

Results

Densified samples

The density of the CAPAD processed samples (discs of 1mm thickness and 19mm diameter) were 99.8%, 99.9%, and 99.9% for the 3YSZ, 6YSZ, and 8YSZ respectively. Grain size measurements of the bulk samples were made from fracture surface measurements of SEM micrographs and showed an average grain size (AGS) of 147±45 nm across all compositions. The polished sample thicknesses were 610±1μm, 584±1μm, and 601±1μm for 3YSZ, 6YSZ, and 8YSZ, respectively.

Material characterization

XRD patterns of samples before and after 50 and 100 h of accelerated ageing via hydrothermal treatment are shown in Figure 2.2(a). XRD patterns in the range of 28°-38° are shown in Figure 2.2(a). Only cubic (111) and tetragonal (101) (both peaks inseparably appeared at 30.2°) can be seen in the XRD patterns, confirming that there is no monoclinic phase present. The peaks and patterns remained the same for all samples following ageing treatments, indicating that no phase transformation occurred. The inset shows monoclinic picks appeared after 10h of ageing treatment in Axis Biodental dental implant control sample with a conventional microscale grain size. In Figure 2.2(b), the comparison of micro-Raman patterns in the 100-900 cm^{-1} region shows stability of

tetragonal and cubic phases after the treatments, further confirming that no phase transformation to monoclinic (doublet at 179 and 190 cm^{-1}) occurred.

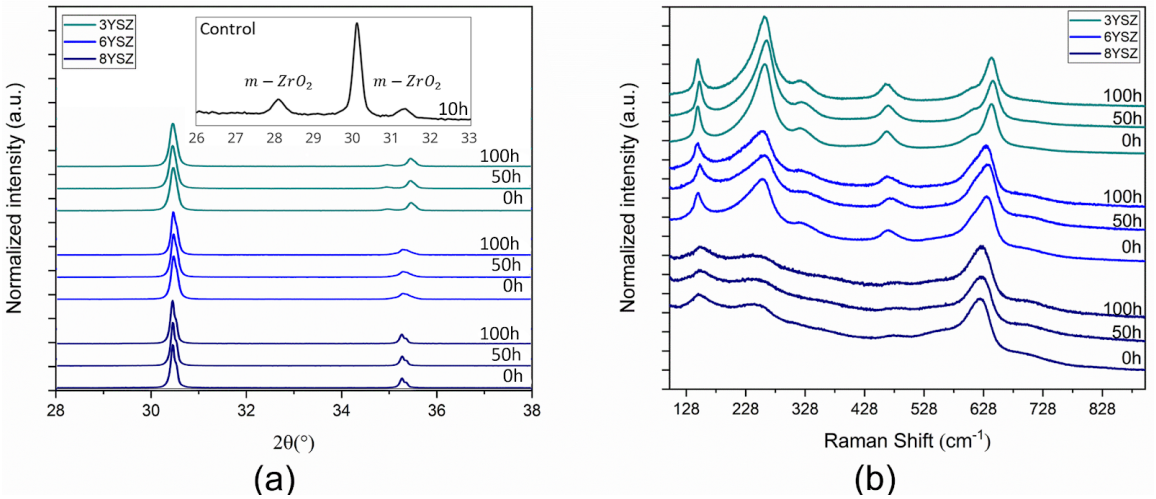

Figure 2.2. For 3YSZ, 6YSZ, and 8YSZ, XRD diffractogram (a) and micro-Raman patterns(b), obtained after up to 100 h of hydrothermal treatment at 134 °C. Monoclinic peaks in the control sample (after 10 h of treatment) are shown in the inset.

Optical characterization

Figure 2.3 shows images of a National Bureau of Standards (NBS) resolution target imaged through the transparent nc-YSZ samples. All of the samples clearly show the highest resolution (18 cycles/mm) on the resolution target when transmitted light is observed through them. As seen in Figure 2.3, all the samples transmit light and appear as different shades of orange.

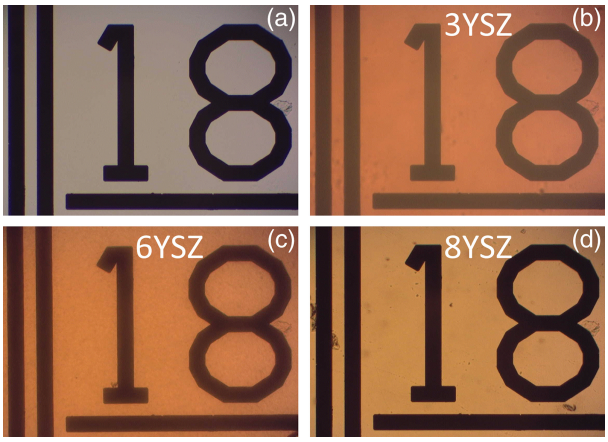

Figure 2.3. Photographs of an NBS 1963A resolution target (a) through the 3YSZ (b), 6YSZ (c), and 8YSZ (d) samples. The resolutions shown are the 18 cycle/mm target (each black line width is 27.78 μm).

To assess any change in optical properties due to the accelerated ageing hydrothermal treatment, optical transmittance of the transparent samples were measured over the wavelength range of 500-1000 nm at baseline and after 50h and 100h of ageing. Figure 2.4 presents the normalized optical transmittance, $T(\lambda)$, for both pristine and aged 3YSZ, 6YSZ, and 8YSZ samples. As shown in the figure, the transmittance curves for all three samples have approximately the same trend. However, for any given wavelength, the transmittance increases as the Yttria content is increased. In addition, the samples transmit a higher percentage of light as the wavelength of the incident light is increased. These results are consistent with our previous measurements, showing relatively low transmission in the blue-green end of spectrum caused by absorption of oxygen vacancy related defects.[74] The inset in Figure 2.4 shows the maximum difference between the

transmittance curves between pristine and aged samples. The changes in transmittance values after the treatments (compared to the pristine samples), were less than 3%.

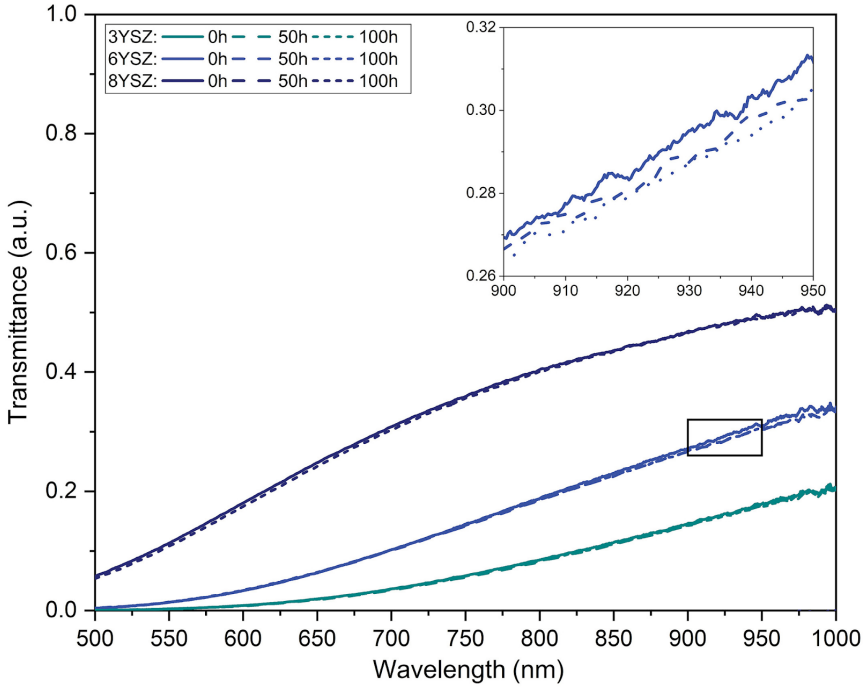

Figure 2.4. Mean T(λ) values obtained at wavelength range of 500-1000 nm to compare the transmittance values of various nc-YSZ samples (3YSZ, 6YSZ, and 8YSZ) before and after ageing. The inset shows the maximum difference in optical properties curves between the pristine and aged samples.

Hardness characterization

As the phase transformation to monoclinic compromises mechanical properties, we compared the hardness of 3YSZ, 6YSZ, and 8YSZ before and after ageing. The averaged results and the standard deviations calculated from 10 indentation experiments per sample are summarized in Table 1.1 as a function of ageing treatment time and Yttria content. For the pristine samples, the highest hardness value was obtained for 3YSZ

sample. The 6YSZ and 8YSZ samples had slightly lower hardness values (6.64% and 4.26%, respectively). For 3YSZ and 8YSZ samples, changes in hardness were not significant (paired two-tail t test), with t values greater than 0.05. For the case of 6YSZ, changes in hardness between pristine sample and sample after 50 or 100 hours of ageing treatment was found to be significant (t = 0.00094 and 0.0037, respectively), although these changes were small (less than 2% increase in hardness compared to pristine sample).

Table 1.1. Hardness of the pristine and aged samples. Data is given with standard deviation (statistical processing of multiple indentations for each sample).

Sample	Hardness (GPa)		
	Pristine	After 50 h	After 100h
3YSZ	13.84±0.20	13.80±0.16	13.71±0.21
6YSZ	12.92±0.10	13.16±0.11	13.13±0.13
8YSZ	13.22±0.12	13.16±0.18	13.17±0.13

Discussion

The transparent nc-YSZ ceramics evaluated in this study show promise for medical and non-medical applications. By performing biocompatibility tests and brain imaging studies, we have demonstrated the feasibility of this application.[24,39,40,68–73,85–87] Phase transformation (ageing) resistance and the effect of hydrothermal treatment on optical and mechanical properties of the ceramics are crucial to understand for any medical or non-medical application of the transparent nc-YSZ ceramics. Recently, fabrication of

translucent and transparent YSZ with grain size on the micro- and nano-scale have been reported.[63,86,88,89] However, a thorough investigation on preparation and evaluation of LTD and its influence on mechanical and optical properties in transparent nanocrystalline stabilized zirconia ceramics with various Yttria dopant levels of 3, 6, and 8 mol% have not been reported.

Ageing caused by the transition of the tetragonal-to-monoclinic phase represents a common problem of zirconia ceramics stabilized by acceptor dopants. The process is triggered by the hydroxyl groups (with bound –OH) which can penetrate into the lattice over time through oxygen vacancies resulting from the doping process.[74] Degradation due to this transformation has been known to propagate gradually to the bulk of the material.[75] Unlike the porosity of micrometric-structured stabilized zirconia ceramics, the nano-scale grain and high densities of our nc-YSZ have proven excellently effective in preventing the transformation, as shown by our results here as well as others.[90,91]

Considering the self-ionization of water, a greater number of OH^- ions produced at higher temperatures and pressures can accelerate the LTD process.[92] Accelerated ageing treatment has been a common method to evaluate zirconia ceramic LTD. Chevalier and Gremillard's evaluation based on actual observations of zirconia femoral heads implanted in vivo for 4 and 8 years, showed that 1h of autoclave treatment at 134 °C had a similar effect as a 3-4 years in vivo ageing.[77] They proved that the ISO standard recommendations for determining the long-term duration of prosthetic zirconia were inadequate[93] and the ISO recommendation was revised according to Gremillard's

suggestions.[94] Advances in grain size reduction resulted in YSZ ceramics that are more resistant against LTD, and for this reason Sanon et al. recommended to increase the ageing test up to 100 h for better observation of the LTD process. Our simulation was extended to 100 h following Sanon's proposal. Given the very high LTD resistance that nanostructured YSZ ceramics have shown compared to conventional microcrystalline YSZ ceramics, a new accelerated ageing simulation protocol will be needed to characterize any transformation and degradation which may occur in these samples.[95]

We have shown our 3YSZ, 6YSZ, and 8YSZ samples with AGS of 147 nm ±45 nm, prepared using CAPAD, satisfy the requirements for long-term performance as an optical implant. Indeed, for all the investigated samples the increase in monoclinic phase content was below the XRD and micro-Raman detection range, in agreement with our previous findings.[86] The ageing tests showed the ability of these materials to withstand common sterilization treatments as well. LTD resistant YSZ samples have been reported recently, however they are produced using the conventional zirconia doped 3 at% of Yttria,[90,96] often co-doped with other cations.[97] In these studies, the samples were sintered by pressure-less techniques with resulting grain sizes of hundreds of nanometers.[89,96,97] YSZ samples prepared by CAPAD (or spark plasma sintering (SPS)) with nanometric grain size have also been shown by others to have very high LTD resistance and density.[88,91] It should also be noted that YSZ samples with similar grain size, mechanical properties and aging resistance have been produced using more conventional multi-step sintering methods.[90]

Optical characterization of the pristine samples shows the optical transmittance is highly dependent on the Yttria dopant level. Higher transmittance was found for the samples with higher Yttria dopant content, although the spectral behaviors are similar for the three sample types (3YSZ, 6YSZ, and 8YSZ). This indicates the increase in the Yttria content which resulted in higher cubic content favors increased transparency.[63] Decreased symmetry of the tetragonal structure causes asymmetric scattering in the 3YSZ sample while the more isotropic structure in the 6YSZ and 8YSZ reduces light scattering.[63,98] This difference in crystal structure is the likely cause of the differences in light transmittance.8YSZ is the most transparent sample, allowing the transmittance of light in a wider wavelength range, starting on 610 nm. The 3YSZ sample is the least transparent. In addition, we have shown the optical property values have a maximum change of 3% after 100 h of the hydrothermal treatments in wavelength range of 500 to 1000 nm for all the samples. This small change is unlikely to be caused by surface crystal phase changes, and may instead be due to measurement error.

The hardness of our nanometric YSZ samples, both pristine and aged, compare well with similar YSZ materials reported in the literature.[91,99] A reduced yttrium (~3 mol% Yttria) content is generally associated with better mechanical properties. In samples with higher Yttria dopant contents, the hardness values are lower, whereas, the transparency is notably increased. The 3YSZ sample (tetragonal structure) showed the best mechanical hardness and 6YSZ and 8YSZ showed slightly lower hardness, due to higher Yttria dopant content which results in the presence of a mixed tetragonal-cubic

structure (6YSZ) and cubic structure (8YSZ). The changes in the averaged hardness values after the treatments for the 3YSZ and 8YSZ were not significant (paired two-tailed t test) while a slight increase (< 2%) was found for the hardness of 6YSZ after ageing treatment. Increased hardness due to ageing an unexpected result, and may be due to measurement error of the hardness of pristine 6YSZ, which was notably lower than the hardness of the other pristine sample compositions.

The combination of YSZ nanopowder and CAPAD offers a procedure for the preparation of high-density, transparent implant material suitable for the production of WttB cranial prosthesis. All the samples with Yttria dopant levels ranging between 3 and 8 mol%, showed a strong resistance to LTD due to nanostructuring, as demonstrated by extended ageing simulations performed following the ISO 13356:2008. The samples were able to sustain tens of hours of treatments at 134 °C; conditions equivalent to many decades of ageing in vivo. A higher Yttria dopant level (8YSZ) showed higher transmittance but presented slightly lower hardness. Finally, comparison of %monoclinic transformation, optical transparency, and mechanical properties of nc-YSZ samples at baseline and following up to 100h hydrothermal treatments shows our implants can withstand the extended ageing treatment.

Acknowledgements

I would like to acknowledge the contribution of my co-authors to this work: Mildred S. Cano-Velázquez, David L. Halaney, Ariana Sabzeghabae, Gottlieb Uahengo, Javier E. Garay, and Guillermo Aguilar. This work was supported by NSF award #1545852 and NSF award #1547014 to GA and JEG.

Chapter 3. Laser speckle imaging of the brain through the implant

Laser speckle imaging (LSI) is a widely used imaging technique which is capable of distinguishing between static and dynamic regions of a sample. Due to its high spatiotemporal resolution, this technique has proved useful for a range of applications such as object velocity measurements[100], blood flow sensing[101], laser vibrometry[102], surface roughness evaluation[103], and acousto-optic tomography[104,105], as well as imaging blood flow[101].

The first application of LSI to cerebral blood flow imaging[106] used LSI spatial contrast analysis[107]. Subsequently, LSI temporal contrast was developed[108,109], which allowed for reduced static noise and improved spatial resolution compared to LSI spatial contrast analysis, at the expense of temporal resolution. In LSI temporal contrast imaging, a coherent source is directed onto a roughened surface, and the scattered light produces a random interference pattern called speckle[110,111]. Movement of scattering particles within the random medium causes phase shifts in the scattered light and thus changes the random interference pattern, producing temporal fluctuations in the speckle pattern[110,111]. When this speckle pattern is imaged with a camera of limited exposure time, these temporal fluctuations in the speckle pattern corresponding to dynamic regions of the sample appear smoother than the surrounding static regions[112,113]. The degree of smoothness is measured as speckle contrast, and previous studies applying LSI to cerebral blood flow have shown that this speckle contrast correlates with blood flow velocity[110,112].

This improved method of LSI temporal contrast imaging was applied to intact rat skull[114], but the poor transparency of the skull resulted in limited spatial resolution of the underlying blood flow. Previous studies have addressed this challenge in animal models by applying LSI through thinned[115] or polished[116] skull, optically cleared the skull[31], or replaced a portion of skull with a transparent window made from glass or PDMS[35,117,118], which are powerful research techniques but which are not appropriate for human application as permanent cranial implants for patients. In Chapter 3, I sought to expand upon previous indications and show WttB implant allows for improved LSI spatial resolution of brain blood flow compared to imaging through the native skull in mice. Specifically, I investigated the stability of the WttB implant for LSI temporal contrast imaging by comparing the sharpness of mouse cerebral blood flow images over 28 days. I also compared LSI temporal contrast imaging between the WttB implant and native skull in a long-term mouse at 60 days post-implantation.

Methods

Implant preparation

Transparent nanocrystalline 8 mol% YO1.5 yttria-stabilized zirconia (nc-YSZ) implant samples were used in this study and fabricated as described in Chapter 2. The thickness of the resulting densified YSZ discs were reduced from 1 mm to ~300 μm by polishing with 30 μm diamond slurry on an automatic polisher (Pace Technologies, Tucson, Arizona USA). The samples were then polished with successively finer diamond and silica slurries ranging from 6 to 0.2 μm. Samples were sectioned into rectangles of

approximately 2.1 x 2.2 mm using a diamond lapping saw (DTQ-5, WEIYI, Qingdao, China), followed by sonication in acetone and thorough rinsing in water. Optical transmittance and reflectance spectra for the polished implants are shown in Figure 3.1.

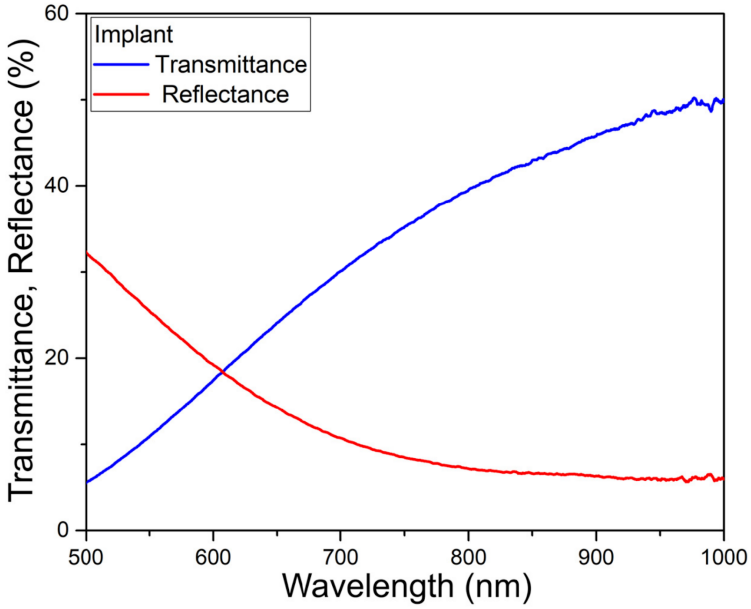

Figure 3.1. Reflectance and transmittance spectra of Window to the Brain implant.

Animals

All experimental procedures and humane care of mice were conducted in compliance with the University of California, Riverside Institutional Animal Care and Use Committee approval. The N = 4 8-12-week-old C57Bl/6 male mice (Jackson Laboratory) used in this study were housed under a 12-hour light and 12-hour dark cycle with *ad libitum* access to food and water.

Surgical procedures

Briefly, mice were anesthetized with isoflurane inhalation (0.2-0.5%), and given ketamine and xylazine (K/X) (80/10 mg/kg, i.p.). Additional anesthetic was administered as necessary. Hair was removed from the scalp using clippers and depilatory cream. Mice were then secured into stereotaxic frames to immobilize the head for surgery. Ophthalmic ointment was placed over the eyes, and the surgical site was sterilized with alternating application of betadine and 70% EtOH (3 times). Implants were also sterilized in 70% EtOH.

A sagittal incision was made to the left of the midline, and the scalp retracted to expose the skull. Periosteum was removed from the skull, and a craniectomy was performed with a surgical drill and carbide burr to remove a square section of skull over the right parietal lobe, with dimensions slightly larger than the implant. The YSZ implant was placed within the craniectomy directly on the intact dura mater, and dental cement was applied to each of the four corners of the implant to prevent displacement. Dental cement was cured with UV light exposure for 20 seconds. Figure 3.2(a) shows an illustration of implant placement envisioned in eventual human application, as well as implant placement used in mice in this study.

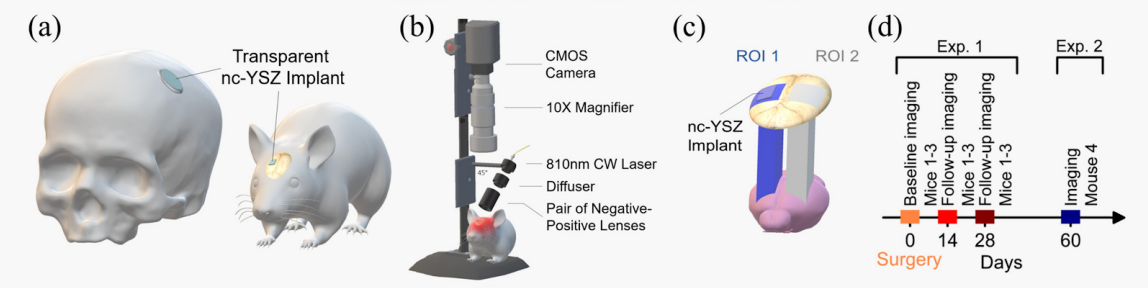

Figure 3.2. a) Illustration of the Window to the Brain concept in human and mouse skulls, b) Schematic of the experimental imaging setup, c) Schematic of the craniotomy location on murine cranium and regions of interest: ROI 1, the nc-YSZ implant and ROI 2, the left parietal bone, d) Timeline for imaging procedures.

Imaging with LSI was conducted immediately after the cranioplasty procedure, while the scalp was still open, as well as follow-up imaging at 14 and 28 days (for Mice 1-3), or 60 days (for Mouse 4) after the implantation surgery. For each follow-up imaging procedure, mice were anesthetized as described above, and the scalp was reopened to expose the implant. Periosteum overlying the implant (and skull for Mouse 4) was removed, and imaging was conducted in an identical manner to the baseline imaging. During imaging sessions, small amounts of saline was dropped onto the skull periodically to prevent drying. Following each imaging procedure, the scalp was closed with continuous suture, and triple antibiotic ointment was applied to the surgical site. Buprenorphine was administered (0.1 mg/kg, s.c.) for postoperative pain control. Mice were placed on a heating pad to aid recovery from anesthesia. A second buprenorphine injection was administered between 4 and 6 hours after surgery.

Laser speckle imaging

LSI and regular images of regions of interest (ROI) (Figure 3.2(c)) were acquired using a 12-bit CMOS camera (DCC1545M, Thorlabs, Newton, NJ, USA). For regular images, a diffuse IR source was used for illumination. For LSI, an 810 nm continuous wave NIR laser (Vari-Lase REF946, Vascular Solutions, Morrisville, NC, USA) was used to illuminate the ROI with incident power of 100 mW at a 45° incidence. While most LSI studies use visible wavelengths for illumination, we chose 810 nm to reduce reflectance and increase transmittance through the implant (see Figure 3.1). The 810 nm laser intensity was homogenized using a diffuser (ED1-C20-MD, Thorlabs) and was expanded using a pair of negative-positive lenses (KPC043, −25 mm EFL and KPX094, 100 mm EFL, Newport, Irvine, CA, USA). Collimated laser light was shown onto the cortex through the WttB implant (i.e. ROI 1 in Mice 1-3) or through both skull and implant (i.e. ROI 1 and ROI 2 in Mouse 4). A sequence of laser speckle images reflected from each illuminated region was captured by the CMOS camera, which was focused 0.2 mm below the cortical surface using a 10X zoom microscope (MLH-10X, 152.4 mm WD, Computar, Torrance, CA, USA). For each ROI, a sequence of n = 100 images were captured at each of four different exposure times (1, 2, 6, and 10 ms) at a speed of 14 frames per second. The aperture and magnification of the zoom microscope were carefully chosen to ensure that the speckle size at the image plane was approximate to the area of a single pixel in the CMOS chip[108,114]. A schematic of the LSI system is shown in Figure 3.2(b).

Experimental design

In this study, we conducted two separate experiments. Experiment 1 was conducted using mice 1-3, with LSI through the implant (i.e. ROI 1) at baseline immediately following implantation, and again after 14 and 28 days post-implantation. In Experiment 2, the LSI field of view was expanded to include both the implant (ROI 1) as well as native skull (ROI 2) in Mouse 4 at 60 days post-implantation. For both experiments, LSI imaging was conducted at 4 different exposure times. A timeline of imaging procedures for the two experiments is shown in Figure 3.2(d).

Image processing and data analysis

The contrast-resolved LSI images were constructed based on temporal statistical analysis of laser speckle which has been proven to preserve spatial resolution[108,114]. Experimental results have indicated that temporal speckle contrast analysis could expressively suppress the effect of the static laser speckle pattern formed by the stationary superficial reflection and scattering tissue on the visualization of blood flow[108,114]. Suppressing this effect makes temporal contrast analysis an ideal method for imaging cerebral blood flow through skull and the transparent nc-YSZ implant. The temporal contrast, *Kt*, of each image pixel in the time sequence was calculated using [108],

$$K_t(x,y) = \frac{\sigma_{(x,y)}}{\langle I_{(x,y)} \rangle} = \sqrt{\frac{1}{(N-1)} \left\{ \sum_{n=1}^{N} [I_{(x,y)}(n) - \langle I_{(x,y)} \rangle]^2 \right\}} \Big/ \langle I_{(x,y)} \rangle \tag{3.1}$$

where Ix,y(n) is the intensity at pixel (x,y) in the nth image, N is the number of images acquired, and Ix,y is the mean value of intensity at pixel (x,y) over the N images. We assessed the quality of the speckle contrast images over time in terms of signal to noise ratio (SNR) and vessel sharpness. To quantify signal to noise ratio for each exposure time and time point, the contrast intensity profile along a vertical line (across the blood vessels) was considered. The profile lines were chosen for each mouse such that 3 to 4 vessels were intersected, and remained the same between the time points and the exposure times. Figure 3.3(b) shows an example of the contrast intensity profile for 6 ms exposure time at day 0, 14 and 28 for Mouse 3. Equation (3.2) shows how SNR values were calculated for each exposure time and time point,

$$SNR = \Delta K / \sigma K_n \tag{3.2}$$

where ΔK is the depth of the vessel peak from the baseline (mean noise) and σKn is the standard deviation of the noise. A visual example of ΔK and σKn are shown in Figure 3.3(b). The SNR values were averaged over the mice (1, 2, and 3) and standard errors were calculated. The optimum SNR between the exposure times in each time point was chosen for the contrast images sharpness comparison. As an indicator of resolution, we compared the sharpness of the vessel edges in images by calculating fall distance (the number of pixels) of the edge of the vessel to go from 10% to 90% of ΔK value were calculated. A shorter fall distance corresponds to greater sharpness. The same sampled

contrast intensity profiles were considered for the fall distance calculation. Figure 3.3(b) shows an example trace and 10–90% fall distance measurement. In order to evaluate the change in sharpness over the time points in Experiment 1, relative change in fall distance over the time points day 14 and day 28 compared to day 0 baseline for each animal and vessel were evaluated using Eq. (3.3).

$$Relative\ fall\ distance = \frac{Fall\ distance - Fall\ distance_{Day}}{Fall\ distance_{Day0}} \tag{3.3}$$

To compare the blood vessel images through-skull and through-implant in Experiment 2, absolute fall distances with respect to the vessels size (FWHM) were determined. FWHM of the vessels in profiles were taken as the vessel diameter (Figure 3.3(b)).

Results

LSI image quality over time (Experiment 1)

The results from Experiment 1 are shown in Figures 3.3 and 3.4. Figure 3.3(a) shows regular images and LSI temporal contrast images at each of the 4 exposure times, for days 0, 14 and 28 from Mouse 3 (data for Mice 1-2 not shown). In the regular images, some tissue regrowth is visible at the implant edges at 14 and 28 days. It should also be noted that at day 0, blood flow is expected to be altered in response to the invasive cranioplasty surgery (e.g. due to potential reactive hyperemia (increased blood flow), changes in respiration, etc.). Due to these differences in the mouse biology and

physiology at different imaging time points, we sought to determine the optimal exposure time for LSI imaging at each time point, so that we could compare the images of highest SNR that could be acquired at each time point.

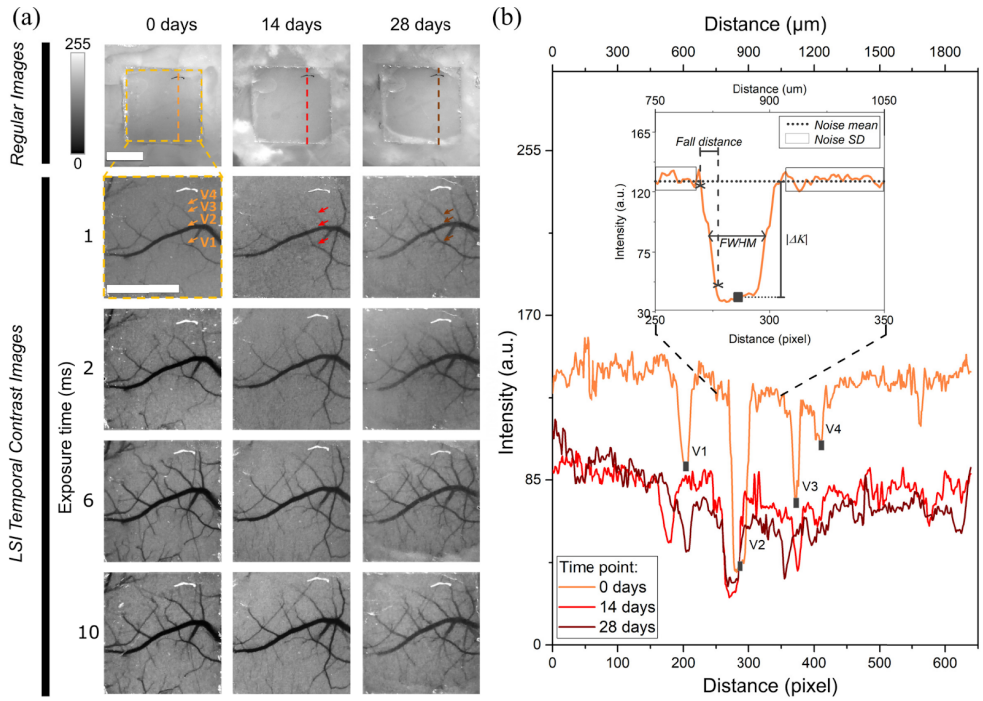

Figure 3.3 a) Regular images and LSI images for exposure times of 1, 2, 6, and 10 ms, at 0, 14 and 28 days post-surgery from Mouse 3 (scale bars = 1 mm). b) Contrast intensity profiles of lines across the images (shown as a dashed line in panel a) at 0, 14 and 28 days post-surgery from Mouse 3. The arrows in a) show the vessels that are intersected by the profile lines shown in b), labeled as V1 through V4 in day 0 image and profile (V4 arrow was not shown in day 14 and day 28 since the microvessel is not visible). The inset in b) shows how noise parameters, |ΔK|, FWHM and fall distance are determined from the line profiles.

Line intensity profiles like the example shown in Figure 3.3(b) were analyzed for all exposure times and imaging time points in Mice 1-3. From these intensity profiles, peak intensity and noise were determined (as described in the Methods section and

illustrated in the inset of Figure 3.3(b)), and signal-to-noise ratio (SNR) was calculated. Data for each time point and exposure time was averaged between the three mice, and is shown in Figure 3.4(a). As shown in the figure, an exposure time of 6 ms gave the highest SNR at 0 and 28 days, while 10 ms exposure time gave a higher SNR at 14 days.

Next, using the 9 LSI temporal contrast images corresponding to these optimal exposure times for days 0, 14 and 28 for Mice 1-3, we sought to compare the sharpness (i.e. fall distance) of the vessels in the images to determine if the images were becoming blurred and losing resolution over time since implantation. The relative change in fall distance between days 14 and 28 compared to day 0 baseline are shown in Figure 3.4(b), and was below a 13% increase for all vessels analyzed. On average, relative fall distance increased by 6.56% ± 1.03% by day 14, and 7.69% ± 1.2% by day 28 compared to day 0.

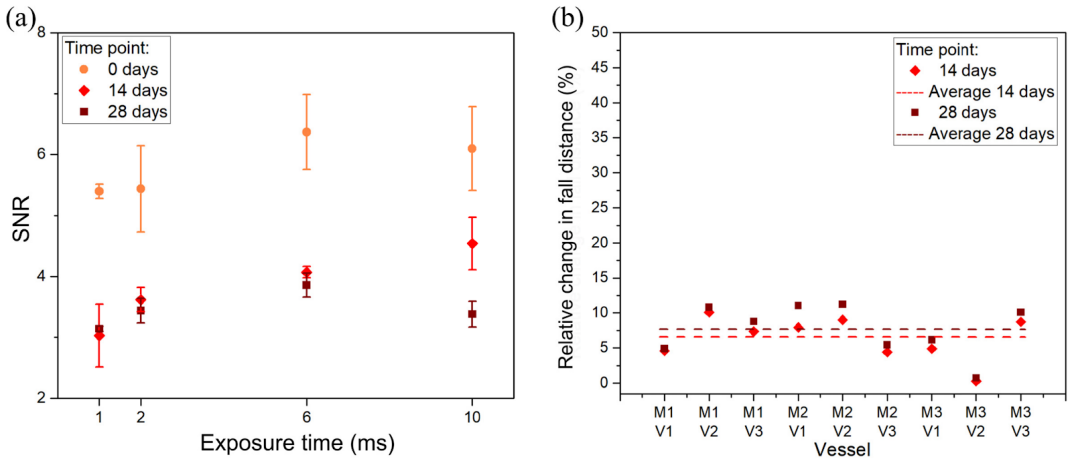

Figure 3.4. a) SNR for different exposure times and imaging time points (mean and standard error) and b) Relative change in fall distance between days 14 and 28 vs day 0 for 3 vessels each of Mice 1-3 (dashed lines represent mean change i5n fall distance for all 9 vessels).

LSI image quality through skull vs. chronic implant (Experiment 2)

As the goal of the WttB implant is to provide long-term optical access to the brain for imaging techniques such as LSI, we sought to compare LSI imaging through the native skull with imaging through a chronic implant which had been in the body long term. Thus, in Experiment 2, Mouse 4 was imaged with LSI 60 days post-implantation. To make a direct comparison between the implant and skull, the LSI field of view was expanded to include both ROI 1 (the implant over the right parietal lobe) and ROI 2 (corresponding region of skull over the left parietal lobe) in the same image. Figure 3.5(a) shows the LSI temporal contrast images for exposure times of 1, 2, 6 and 10 ms.

Unlike Experiment 1, where a given field of view was compared with itself over time, Experiment 2 compares two separate regions of the brain with different vessels. Thus, for this second experiment, 3 line profiles with taken for the implant and for the corresponding region of skull. To avoid selection bias, the location of these line profiles were chosen arbitrarily at the ROI mid- and quarter-points, as depicted in the regular image in Figure 3.5(b). As an example, Figure 3.5(c) shows the intensity profiles from the midline of both ROI 1 and ROI 2 for exposure time 6 ms.

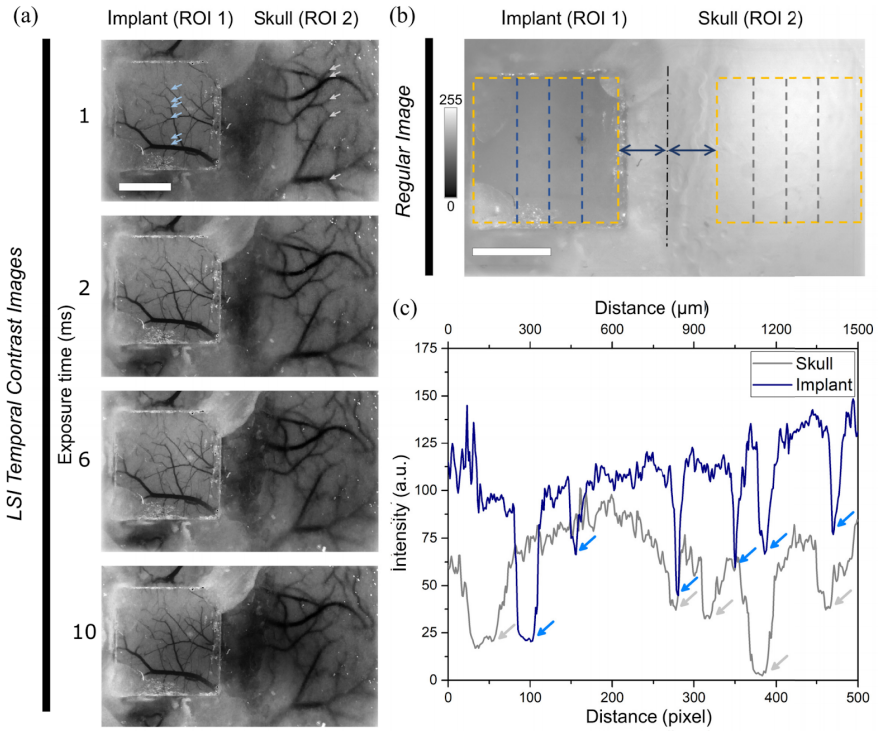

Figure 3.5. a) LSI temporal contrast images for 4 exposure times in Mouse 4. The left side of each image is the WttB implant (ROI 1), and ROI 2 is the corresponding region of skull on the right side of each image. b) Regular image of implant, showing the arbitrary locations where line profiles were taken. c) Example contrast intensity profiles along the midline of ROI 1 and 2 for exposure time 6 ms. The arrows in a) and c) show the vessels that are intersected by the midline intensity profiles. Scale bars = 1 mm.

Using the same analysis methods described in Experiment 1, we calculated the SNR from each line profile in ROI 1 and ROI 2 for each exposure time. The mean SNR for each exposure time is shown in Figure 3.6(a). The 6 ms exposure time LSI temporal contrast image resulted in the highest SNR for both implant and skull, and thus we used this image to compare the SNR and sharpness of detected vessels by LSI between native skull and a long-term WttB implant. By the same method used in Experiment 1, we analyzed the 3 line profiles across the WttB implant and 3 line profiles across the skull to determine the fall distance and SNR for each vessel. Additionally, the full-width half-max (FWHM) of each vessel in the line profiles were taken as vessel diameter[62]. Figure 3.6(b) shows a plot of all vessels intersected by the 6 profile lines, with SNR plotted against FWHM (i.e. vessel diameter). A plot of all vessels intersected by the 6 profile lines, with absolute fall distance (i.e. vessel sharpness) plotted against FWHM (i.e. vessel diameter) is shown in Figure 3.6(c).

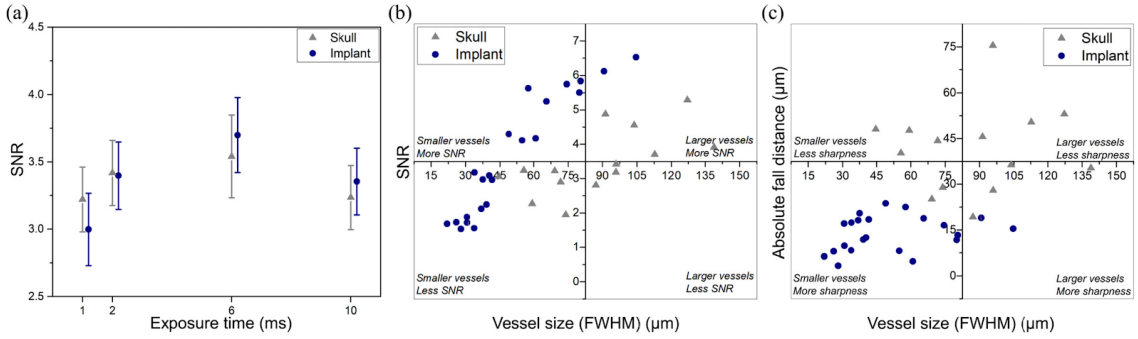

Figure 3.6. a) Mean SNR of contrast intensity along arbitrary line profiles on the implant and skull for 4 separate exposure times (error bars represent standard error), b) and c) SNR and sharpness (respectively) vs FWHM for all vessels intersected by arbitrary line profiles on the implant and skull for the LSI temporal contrast image acquired with 6 ms exposure time.

Discussion

As the goal of the WttB implant is to provide this access long-term, it is important that the optical access is not lost over time. In Chapter 3, I assessed LSI temporal contrast imaging quality (i.e. sharpness) of cerebral blood vessels imaged through the implant up to 60 days post-implantation.

In LSI temporal contrast imaging, the exposure time of the camera can have a large effect on image quality. As exposure time increases, both the contrast intensity and noise of the image increase[119]. While the contrast plateaus after some threshold, noise continues to increase with exposure time. Several sources of noise contribute to the measured noise, including physiological noise, hardware noise, environmental noise, and noise due to statistical uncertainties. The total noise of the speckle contrast signal is a combination of all of these sources and the relative contributions of each of these exhibit different characteristics with respect to the exposure time[119]. However, in our experiments, the physiologic noise (including noise due to implantation surgery) is the dominant source because it is the only one that is changing considerably over time. Physiologic noise arises from motion of the tissue such as heartbeat or respiration-induced pulsatile motion of the exposed cortex, baseline fluctuations in the cerebral blood flow, and possibly tissue regrowth and revascularization following implantation. This motion and blood flow fluctuations introduce additional velocity components to the measured signal and therefore cause speckle contrast fluctuations. Since the physiological noises will be different on different days, exposure time should

be optimized during each imaging session. To determine the optimal exposure time in this study, we compared the SNR of images taken at exposure times of 1, 2, 6, and 10 ms (Figure 3.4(a), Figure 3.6(a)), and each imaging session proceeded with the exposure time that maximized SNR. Indeed, our results found that the optimal exposure time differed between the imaging time points in Experiment 1, with maximum SNR for exposure time of 6 ms at days 0 and 28, and 10 ms at day 14. This may be explained by the differences in physiology between these time points. At day 0, altered blood flow due to the implantation surgery is expected, and elevated blood flow could give high contrast to the vessels. Thus, a lower exposure time (6 ms) can provide sufficient contrast of the blood flow, while keeping noise low. By day 14, flow would no longer be modified in response to the surgery, and thus a higher exposure time (10 ms) may be needed to increase contrast in the images. At time points beyond 14 days, flow remains low compared to day 0, but noise may increase due to healing processes (tissue regrowth, revascularization, etc.), and thus a shorter exposure time (6 ms) may provide the best compromise between increased contrast and reduced noise. It should be noted, however, that the modification of blood flow at the different time points, as evidenced by the different optimal exposure times, may also be due to several other confounding factors. Anesthetic agents (including isoflurane and ketamine used in this study) are known to modulate cerebral blood flow, and the concentration of these drugs in the blood stream was not kept constant over the imaging sessions. Respiration can cause noise in LSI, and its rate, along with arterial blood gas levels, can significantly alter blood flow. These

variables, in addition to the small sample size used in this study, make it difficult to attribute the observed differences in blood flow between the time points to a particular cause.

Image resolution (i.e. sharpness) was found to decrease by up to 13% over the 28 days compared to day 0 baseline in the 9 vessels analyzed from Mice 1-3 (Figure 3.4(b)). The relative increases in average fall distance between day 14 and day 28 compared to day 0 were 6.56% ± 1.03% and 7.69% ± 1.2%, respectively. It should be noted that while day 0 is considered as the baseline for comparison, it does not represent an unperturbed state of normal cerebral blood flow. It is likely that blood flow was altered in response to the invasive cranioplasty surgery, and thus the higher SNR and sharpness of the day 0 images compared with days 14 and 28 may be due in part to an elevated signal at day 0, rather than a loss of signal at days 14 and 28. SNR and sharpness stayed more stable between 14 and 28 days, consistent with this hypothesis. Additionally, new microvessels which were not visible in day 0 are visible at these later time points, which suggests revascularization may be occurring near the implant surface. Together, these results appear to indicate that image quality remains high up to 28 days post-implantation, but additional longer time points are needed to confirm this is the case. In Experiment 2, a day 60 time point shows that SNR is similar to the SNRs obtained at days 14 and 28 in Experiment 1 (SNR between 3 to 4 in both Figure 3.4(a) and Figure 3.6(a)), and microvessels are clearly visible at this later time point (Figure 3.5(a)).

Comparing imaging through the skull and a long-term (60 days) implant (Figure 3.5(a)), the skull had a higher SNR for lower exposure times (1 and 2 ms), and the implant SNR was higher at longer exposure times (6 and 10 ms) (Figure 3.6(a)). The higher SNR of the through-skull images compared with implant at short exposure times may be explained by the natural filtering-out of smaller vessels imaged through the skull. Imaging through the window, on the other hand, resolves small vessels which are more sensitive to exposure time. At low exposure time, the contrast of these small vessels is very low, contributing to the lower SNR through the window compared to skull. Exposure time of 6 ms gave the highest SNR for both skull and implant and was used for comparing SNR and sharpness of vessels imaged beneath each. Because this comparison was made between two different spatial regions of the brain, different vessels of varying diameter were compared. Thus, SNR and sharpness of vessels (fall distance) are plotted against the vessel diameter (FWHM of vessels in intensity profiles). As mentioned earlier a number of small vessels, associated with lower blood flow and accordingly SNR, were detected through the implant which were naturally filtered-out by the skull (Figure 3.6(b)). These detected small vessels decreased the averaged SNR shown in Figure 3.6(a). In Figure 3.6(c), interestingly, the data from the skull and implant fell into separate clusters, with vessels imaged through the implant having smaller FWHM and shorter fall distances, while vessels imaged through the skull have larger FWHM and higher fall distances. This data shows that vessels imaged through the implant appear smaller in diameter and have sharper borders compared to those imaged through the

skull. As the size of vessels and velocity of blood flow is not expected to differ on average between the two hemispheres of the mouse brain, the apparent increase in vessel diameter imaged through the skull vs implant is likely due to blurring of the image through the skull. In general, the light transmission to the brain and reflection from the brain are lower in the through-skull image. Additionally, the skull scattering disorders the speckle pattern that was created by the brain hemodynamics, making a less accurate speckle pattern. Both of the defects are caused by skull and the skull texture is not homogeneous, making image correction or enhancement very complex[114]. The reduction in border sharpness of the vessels imaged through the skull vs implant is consistent with this explanation, and the blurred nature of the through-skull image compared to the through-implant image is visually apparent in Figure 3.5(a). It should also be noted that while the SNR and sharpness of the through-implant images are an improvement over the through-skull images, the mouse skull is inherently transparent itself[114], which is not the case in larger animals or humans.

LSI temporal contrast imaging has become a useful tool for brain blood flow applications as the images it produces contain functional information (i.e. relative blood velocity) in addition to showing structure of the vessel networks. Figure 3.7 contains a color map version of the 6 ms LSI image from Mouse 4 (Figure 3.5(a)), where minimum relative velocity (i.e. static regions) appears blue and maximum relative velocity (i.e. maximum blood flow velocity) appears red. As seen in Figure 3.7, much more precise velocity information, particularly of microvessels, can be detected through the implant,

while the reduced sharpness of the vessels imaged through skull obscures precise flow determinations. Imaging microvessels (usually involving small arteries of less than 150 μm in diameter, arterioles, capillaries, and venules[120,121]) is important for many applications, as microcirculation plays a critical role in physiological processes such as tissue oxygenation and nutritional exchange. Monitoring the spatio-temporal characteristics of microcirculation is crucial for studying the normal and pathophysiologic conditions of tissue metabolism. It is also useful for assessing microcirculatory dysfunction due to disease conditions such as type 2 diabetes, peripheral vascular disease (PVD), atherosclerotic coronary artery disease, obesity, heart failure, Alzheimer's, schizophrenia and hypertension, among others. In addition, quantification of dynamic blood flow, angiogenesis, and vessel density are critical for monitoring the progression of wound healing. Although high resolution vascular network mapping is possible using imaging modalities such as computed tomography (CT), these approaches require injection of contrast agents and pose disadvantages such as radiation exposure. Existing non-invasive methodologies (including LSI through skull) are inadequate to study blood flow at microvessel resolution[122]. Windows such as the WttB implant are thus important tools for research, and in the case of the WttB implant, can become important enablers of clinical diagnostics and therapy involving cerebral microvessels.

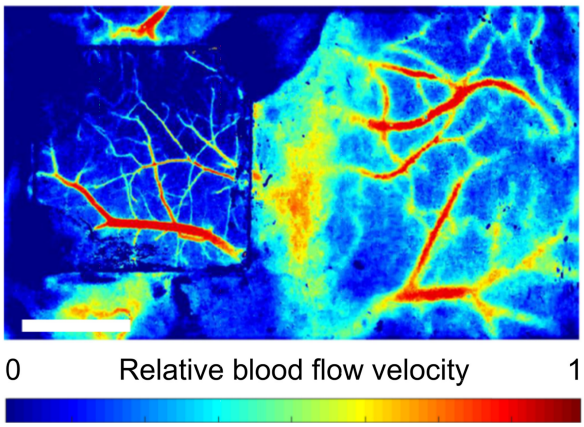

Figure 3.7. Relative blood flow velocity in the 6 ms exposure time LSI temporal contrast image from Mouse 4. Scale bar = 1 mm.

Acknowledgments

I would like to acknowledge the contribution of my co-authors to this work: Mildred S. Cano-Velázquez, David L. Halaney, Carrie R. Jonak, Devin K. Binder, and Guillermo Aguilar. This work was supported by National Science Foundation (NSF-PIRE) (1545852) and "Beca Mixta" from National Council of Science and Technology of Mexico (CONACYT) (741249). The authors would like to thank Gottlieb Uahengo for the fabrication of the YSZ samples.

Chapter 4. Optical Access to Arteriovenous Cerebral Microcirculation

Background

Microcirculation plays a critical role in the physiological processes of tissue oxygenation and nutrient exchange within the brain[11]. In recent years, the recognition that microcirculation is also involved in a number of pathophysiologic processes has further increased interest in its study[11]. Microcirculation can be measured in several ways, including (but not limited to) morphological imaging methods to measure vessel density, perfusion rate, vessel diameter, and dynamic measurements of microcirculatory blood flow velocity and blood cell concentration[11], as well as functional imaging methods to provide information on blood oxygenation, changes in metabolism, regional chemical composition, and so on[12].

In addition to information on vessel geometry and flow characteristics, distinction between arteries and veins is of great clinical importance. The ability to independently render veins and arteries on blood perfusion maps has a variety of potential applications in the head, neck, lungs, heart, abdomen, and lower extremities, and most critically in the cerebrovascular system including brain arteriovenous malformation and dural arteriovenous fistulas[123], cerebral hemorrhage, stroke, and aneurysm[124].

In this chapter, we utilized the wide light transmission range of WttB implant for a dual-modal imaging system of multispectral reflectance imaging (MSRI) and LSI. MSRI is a simple and low-cost method capable of distinguishing between veins and arteries based on differences in the optical absorption of oxyhemoglobin and deoxyhemoglobin.

This method has been developed in visible and near-infrared (NIR) wavelength range[125,126]. This method involves a white light source, optical filters, and a camera, and can easily be coupled with LSI[124]. Indeed, a single instrument combining laser speckle flowmetry and MSRI has been demonstrated in a rodent thinned skull model[126] for simultaneous relative cerebral blood flow and hemoglobin oxygen saturation changes during ischemia[127] and functional activation[128]. A thinned skull preparation was necessary due to the high scattering and absorption of the skull in the visible and NIR range, which limits the accessibility of MSRI wavelengths for detecting hemoglobin oxygenation information. When MSRI has been applied through the intact skull, only skull regions and not individual microvessels are visible. Likewise, in our own prior studies we have found that imaging through intact skull with LSI limits the size of vessels that can be detected, and precludes imaging of the microcirculation. Moreover, the absorption and reflectance features of the inhomogeneous cranial bone overlap with those of brain tissue, and the skull also has its own vessels. Together, these factors decrease the accuracy and reliability of the data.

Window to the Brain implant made of Yttria-stabilized zirconia (YSZ) represents an attractive alternative. Additional benefits of this material over imaging through skull include its stable optical behavior, as proven in Chapter 3, and lack of optical absorption by water and hemoglobin (Figure 3.1). We envision this implant as a potential future optical access to the brain allowing for real-time monitoring of arteriovenous cerebral blood flow (Figure 4.1).

In this present study, we performed cerebral arteriovenous microcirculation imaging by combining MSRI and LSI techniques. This method was applied in a mouse model, first through the closed skull, then to the dura mater and brain directly after a craniectomy was performed to remove a piece of skull, and finally through the WttB implant after the implant was placed within the craniectomy on the dura mater. The imaging obtained through the WttB implant and through the skull were compared to the imaging obtained through the open skull, which served as a reference. The goal of this study was to assess the improvement in brain imaging with MSRI-LSI when captured through the WttB implant versus imaging through the skull.

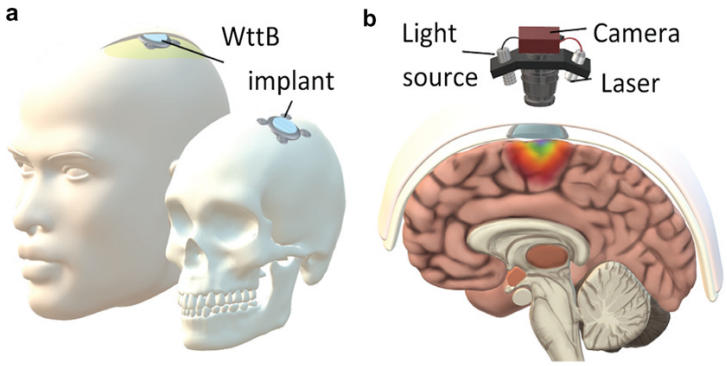

Figure 4.1. (a, b) Illustration of the Window to the Brain concept as envisioned for future human application, to allow for real-time monitoring of arteriovenous cerebral blood flow. (c) Transmittance spectra of Window to the Brain implant.

Methods

Animals

All experimental procedures and humane care of mice were conducted in compliance with the University of California, Riverside Institutional Animal Care and Use Committee approval. The N = 1 12-week-old C57Bl/6 male mouse (Jackson Laboratory, Bar Harbor, ME) used in this study was housed under a 12-hour light and 12-hour dark cycle with ad libitum access to food and water.

Surgical Procedures

The mouse was implanted with a WttB implant as described previously in Chapter 3. Imaging was conducted with the scalp open, before craniectomy with the skull closed (condition 1), immediately after craniectomy with the skull open (condition 2), and after the WttB implantation (condition 3).

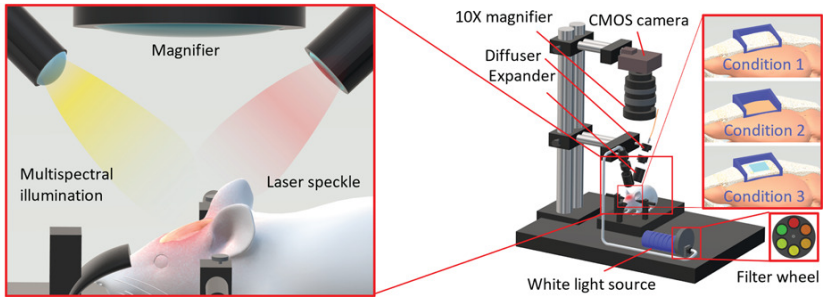

Figure 4.2. Schematic of the experimental imaging setup including laser speckle imaging (LSI) and multispectral reflectance imaging (MSRI). The inset shows a schematic of the imaging fields of view on murine cranium, with the blue tetragonals representing the imaging field.

MSRI and LSI

MSRI was performed by optically filtering a white-light source (MI-150; Dolan-Jenner, Boxborough, MA). Optical bandpass filters mounted on a fast-change filter wheel (FW103H; Thorlabs, Newton, NJ) were used to isolate different spectral components and provided a six-wavelength (560, 570, 580, 590, 600, and 610 nm) multispectral dataset, as shown in Figure 4.2. For LSI, an 810 nm continuous wave NIR laser (DL808-7W0-O; CrystaLaser, Reno, NV) was used to illuminate the region of interest with incident power of 100 mW at a 45° incidence. While most LSI studies use visible wavelengths for illumination, we chose 810 nm to reduce reflectance and increase transmittance through the WttB implant (see Figure 3.1). The 810 nm laser intensity was homogenized using a diffuser (ED1-C20-MD; Thorlabs) and was expanded using a pair of negative-positive lenses (KPC043, −25 mm EFL and KPX094, 100 mm EFL; Newport, Irvine, CA). Multispectral incoherent light and diffused laser light were sequentially shown onto the closed skull (i.e., condition 1), onto the dura mater and cortex after craniectomy (i.e., condition 2) and through the WttB implant (i.e., condition 3). The reflected light from the illuminated region was captured by a 12-bit complementary metal-oxide-semiconductor (CMOS) camera (DCC1545M; Thorlabs), which was focused at the cortical surface using a ×10 zoom microscope (MLH-10X, 152.4 mm WD; Computar, Torrance, CA). For each imaging condition, a sequence of six multispectral images and 100 laser speckle images were captured. Laser speckle images were acquired at exposure times of 6 ms (per our previous report on optimized LSI

exposure time[24]) at a speed of 14 frames per second. The aperture and magnification of the zoom microscope were carefully chosen to ensure that the speckle size at the image plane was approximate to the area of a two pixel in the CMOS chip. A schematic of the imaging system is shown in Figure 4.2. In image processing, each camera frame was registered to one another to ensure appropriate spatial alignment over the MSRI and LSI images. In MSRI, normalizing each individual wavelength to its corresponding white reference (WS-1; Ocean Optics, Oxford, UK) image compensated for variations in the illumination. The white reference images were captured through the WttB implant in condition 3.

Vein-Artery Separation Using MSRI

The MSRI approach relies on the distinctive absorption spectra of oxy- and deoxyhemoglobin (HbO2 and HbR). The hemoglobin in blood is the most significant absorber in the brain at visible and NIR wavelengths. HbR and HbO2 have different absorption spectra, and thus based on the Beer-Lambert law[129], measurements with different wavelengths of light can produce images that are preferentially sensitive to difference in the concentration of HbO2 and HbR. At isobestic points, the HbR and HbO2 optical extinction coefficient are similar (568 and 587 nm). At 560, 600, and 610 nm, areas with higher level of deoxy-hemoglobin C (e.g., the veins) leads to more optical extinction and thus makes the corresponding area darker (i.e., lower intensity values in the images), and therefore we can provide artery-vein separation. In this case, we assume that scattering in the brain does not change significantly during the

experiment. To separate the vein and arteries in MSRI images, the vasculature branches were detected and mapped manually for seven branches in regular white-light images (Figure 4.3(a)). Each vasculature branch was labeled by a number. To obtain the mean intensity of a branch, 10 samples of intensity (4 × 4 pixels) were extracted and averaged from each branch and called vessel branch intensity. The sample intensities of each branch were evenly distributed along the midline of the main vessel of the branch (Figure 4.3(a)). The samples locations were kept constant for each vasculature branch over the multispectral images. Then, normalized extinction was obtained over the wavelengths by calculating the difference in intensities of the white reference and the vessel branch, normalized by white reference intensity following Equation 4.1,

$$\text{Normalized extinction} = \frac{I_{n,\lambda} - I_{R,\lambda}}{I_{R,\lambda}} \tag{4.1}$$

where I(n,λ) is vessel branch number n, intensity at λ wavelength, and I(R,λ) is the mean value of the white reference intensity at λ wavelength.

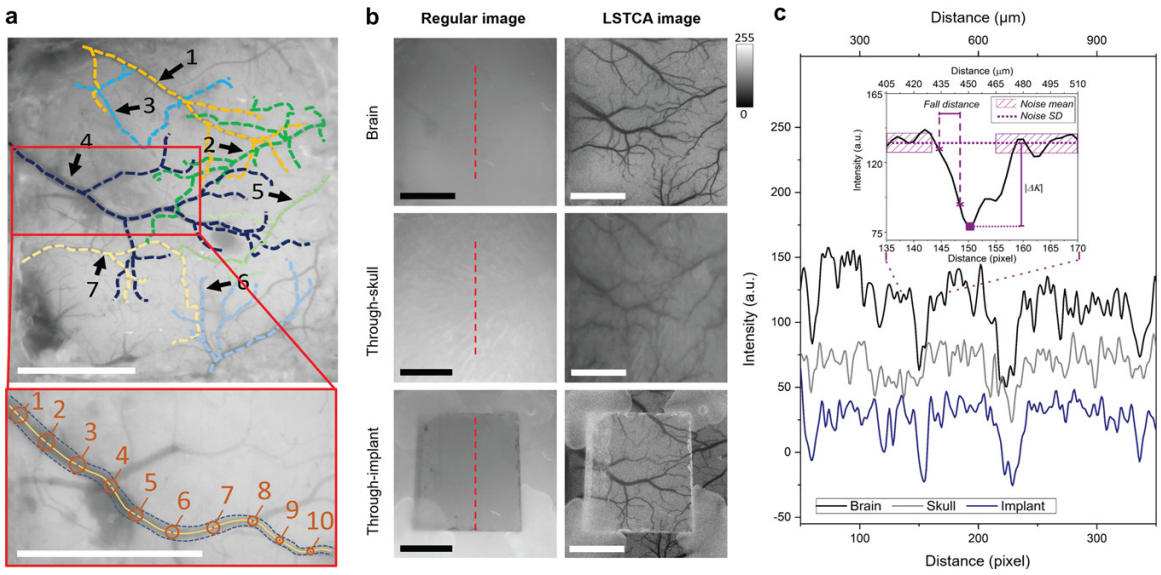

Figure 4.3. (a) Vessels branches of 1–7 indicated by different colors on a regular white-light image of the brain image through the open skull (condition 2). The inset shows an example of evenly distributed intensity samples along the midline of the main vessel of the branch 4, which were used to calculate the vessel branch intensity. (b) Regular white-light images and laser speckle imaging (LSI) images (scale bars = 1 mm). (c) Contrast intensity profiles of lines across the images (shown as a dashed line in panel (a). The inset in (c) shows how LSI noise parameters, |ΔK| and fall distances are determined from the line profiles.

Rebuilding Arteriovenous Cerebral Blood Flowmetry Map Based on MSRI-LSI

Step 1: Constructing a flow map using laser speckle temporal contrast analysis (LSTCA)

The contrast-resolved LSI images were constructed in the same manner as the Chapter 3, based on the temporal statistical analysis of laser speckle, which has been proven to preserve spatial resolution.

Step 2: Arteriovenous vasculature network

The vasculature network was extracted from the LSI image according to the difference in flow velocity between the vasculature and tissue. A Hessian-based filtering

algorithm was then used to enhance contrast and connectivity in the image of the vasculature[130]. In this step, vessels are detected using the eigenvalues of the image, and detection is sensitive to vessels in any orientation. Vessel detection was performed over multiple vessel scales (from ~20 to 400 μm in diameter), and the maximum filter response for each pixel was used. The resulting image was thresholded to produce a binary mask of the vasculature. The arteriovenous information obtained by MSRI was then registered on the vasculature network obtained by LSI, and veins and arteries were labeled on the vasculature network LSI images.

Step 3: Weighting the arteriovenous vasculature network by the blood flow map

Finally, the resulted arteriovenous vasculature network was weighted by the calculated LSTCA relative blood flow information.

Quantitative Analysis of the LSI Resolution and Contrast

We assessed the quality of the speckle contrast images in terms of signal to noise ratio (SNR) and vessel sharpness, in the same manner as Chapter 3. The profile lines were chosen based on the open-skull images such that four vessels were intersected. The same spatial location (i.e., same vessels) were analyzed in the through-skull and through-implant conditions as well. When imaging through skull, one of the four vessels was not visible and was omitted from the analysis of that condition. Figure 4.3(c) shows an example of the contrast intensity profile for the brain with open skull, through-skull, and through-implant. A visual example of ΔK (Signal) and σKn (Noise) are shown in Figure 4.3(c). The SNR values were averaged over the profile vessels and standard errors

were calculated. Sensitivity, which is considered as the ratio of the mean SNR to the mean SNR of the reference, was calculated using Equation 4.2

$$\text{Sensitivity} = \frac{\text{SNR}_{\text{imaging condition } n}}{\text{SNR}_{\text{imaging condition 2}}} \tag{4.2}$$

As an indicator of resolution, we compared the sharpness of the vessel edges in images by calculating the fall distance, (as explained in Chapter 3)[131]. A shorter fall distance corresponds to greater sharpness. Figure 4.3(c) shows an example trace and 10–90% fall distance measurement. To compare the blood vessel images through-skull and through-implant, the fall distances were determined and averaged over the profile vessels and the standard errors were calculated.

Results

Through-Skull and Through-Implant MSRI Images

The mapped vasculature branches and vein-artery separated network from open-skull imaging (i.e., condition 2) are shown in Figure 4.4(a) and 4.4(b), respectively. Figure 4.4(d) shows the spectral behavior of the branches. The dashed line in Figure 4.4(d) shows the mean optical extinction of all seven branches. Overall, optical extinction is relatively high for wavelengths of 560–580 nm. A drastic decrease in optical extinction happens at wavelengths of 590, 600, and 610 nm. Notably, the vessel branches 1 and 4 show a different trend compared to branches 2, 3, 5, 6, and 7. These two groups were labeled in red and blue and the mean (solid lines) and standard deviation (colored shadow) of each group were separately calculated and shown. The blue group including branches 1 and 4 resulted in higher optical extinction at 560 nm. At wavelengths of 570

and 580 nm, red group showed the extremum values. Optical extinction values of red group have a higher decrease than the blue group at 590 nm and show lower optical extinction values at wavelengths of 590, 600, and 610 nm than the blue group. Comparing the relation between red and blue groups to the reported configuration of oxyhemoglobin and deoxyhemoglobin chromophores, optical extinction coefficients in the wavelength range of 560–610 nm[132] illustrates the existence of a higher concentration of oxyhemoglobin and relatively lower concentration of deoxyhemoglobin in the red group (vessel branches 2, 3, 5, 6, and 7) than the blue group (vessel branches 1 and 4).

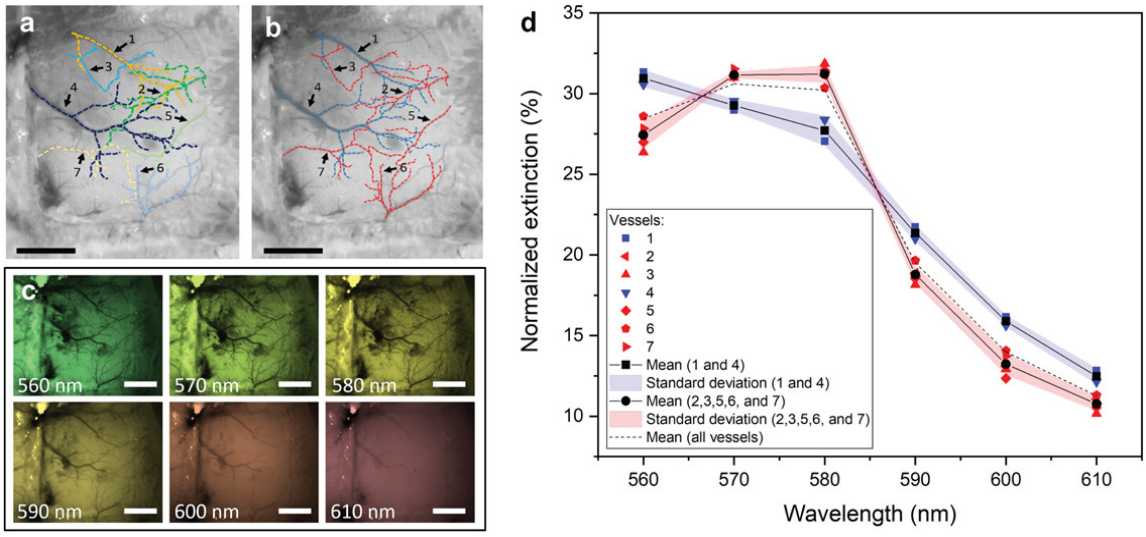

Figure 4.4. Cerebral arteries-veins separation using multispectral reflectance imaging (MSRI), in open skull imaging (i.e., condition 2). (a) Labeling the vasculature branches on a regular white-light image. The images were converted to gray color map to make the colored vasculature branches clear. (b) The separated veins (blue) and arteries (red) (scale bars = 1 mm). (c) Optical images of the brain illuminated by various wavelengths. (d) Relative optical absorption values plotted for each branch.

A regular white-light image of the closed mouse skull (i.e., condition 1) is shown in Figure 4.5(a). The MSRI images captured through the cranial bone of the mouse do not show the vasculature network. Consequently, we were not able to identify the vessels branches and their intensities over the multispectral images in Figure 4.5(b).

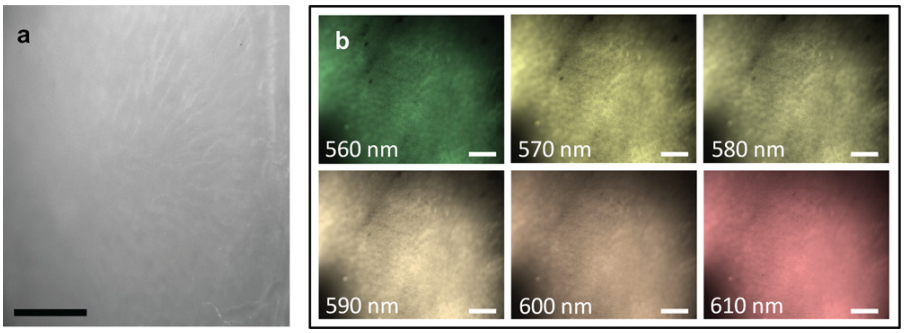

Figure 4.5. The multispectral reflectance imaging (MSRI) through closed skull (i.e., condition 1). (a) Regular white-light image of the skull. The image was converted to gray color map to increase contrast. (b) Optical images of the mouse skull illuminated by various wavelengths. As seen, the vasculature map is not evident when imaged through skull (scale bars = 1 mm).

Figure 4.6(a) shows mapped vasculature branches on a regular white-light image through the WttB implant (i.e., condition 3). Multispectral images as shown in Figure 4.6(c) resulted in a notable lower contrast compared with the references images (Figure 4.4(c)). The spectral behavior of the branches is plotted in Figure 4.6(d). The dashed line indicating the overall mean optical extinction for all seven branches shows a general decrease in the relative optical extinction compared with imaging the brain directly (Figure 4.4(c)), which is due to the reflected light from the WttB implant surface overcoming the vessels optical extinction. Similar to the direct brain images (imaging condition 2), the mean optical extinction (dashed line) is relatively high for wavelengths

of 560–580 nm, followed by a decrease at wavelengths of 590, 600, and 610 nm. Although there is a lower deviation between the optical extinction values, the separate trend of the vessel branches 1 and 4 compared with branches 2, 3, 5, 6, and 7 is still noticeable. Accordingly, these two groups were labeled in red and blue and the mean and standard deviation of each group were separately calculated and shown in Figure 4.6(d). The analysis of the images obtained through WttB implant (imaging condition 3), shows a similar conclusion to the reference data (imaging condition 2). Although the relative optical extinction values have a notably higher deviation (which affects the accuracy of the analysis) compared with imaging the brain directly, the vein-artery separation is indeed doable through the WttB implant.

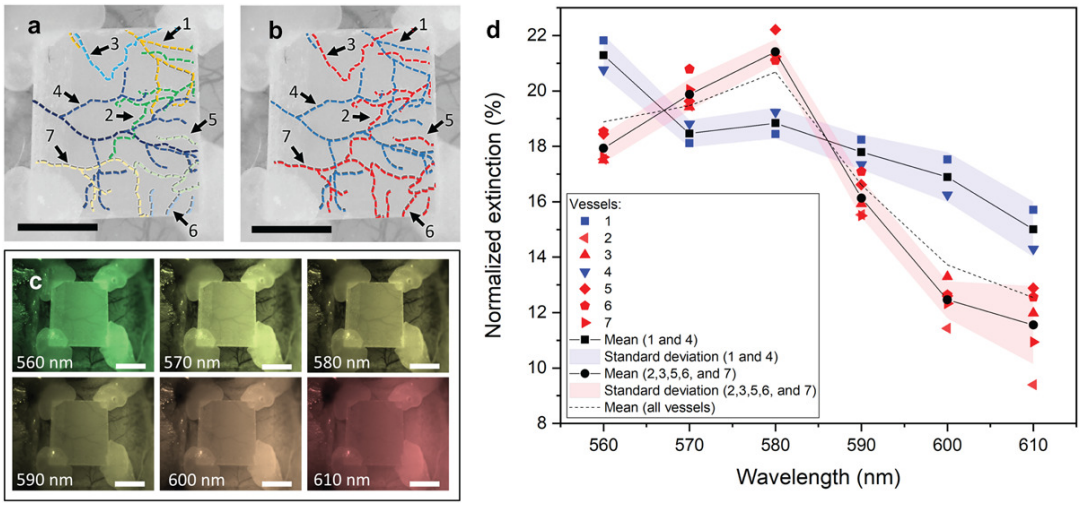

Figure 4.6. Cerebral arteries-veins separation using multispectral reflectance imaging (MSRI) through the Window to the Brain (WttB) implant (imaging condition 3). (a) Labeling the vasculature branches on a regular white-light image of the implantation region (condition 3). (b) The separated veins (blue) and arteries (red). (c) Optical images of the brain illuminated by various wavelengths. (d) Normalized mean intensity values plotted for each branch.

Through-Implant and Through-Skull LSI Images

Figure 4.3(b) shows regular white-light images and LSI temporal contrast images of brain, through-skull, and through-implant. It should also be noted that after the surgery, blood flow is expected to be altered in response to the invasive craniectomy surgery (e.g., due to potential reactive hyperemia[133] (increased blood flow), changes in respiration, etc.). We previously reported the optimal exposure time for LSI imaging at each time point, so that we could compare the images of highest SNR that could be acquired of the brain, through-skull, and through-implant.

Line intensity profiles like the example shown in Figure 4.3(c) were analyzed for the brain, through-skull, and through-implant contrast images. To avoid selection bias, the location of these line profiles were chosen arbitrarily at the region of interest (ROI) mid-points, as depicted in the regular white-light image in Figure 4.3(b). From these intensity profiles, peak intensity and noise were determined (as described in the Methods section and illustrated in the inset of Figure 4.3(c)), and SNR ratio was calculated. Data for each imaging condition was averaged between the vessels and the mean SNR for each imaging condition is shown in Figure 4.7(a). As expected, the brain contrast image shows the highest SNR (imaging condition 2). The through-implant contrast image (imaging condition 3) resulted in the higher SNR compared with the through-skull contrast image (imaging condition 1) by 17.59% (relatively).

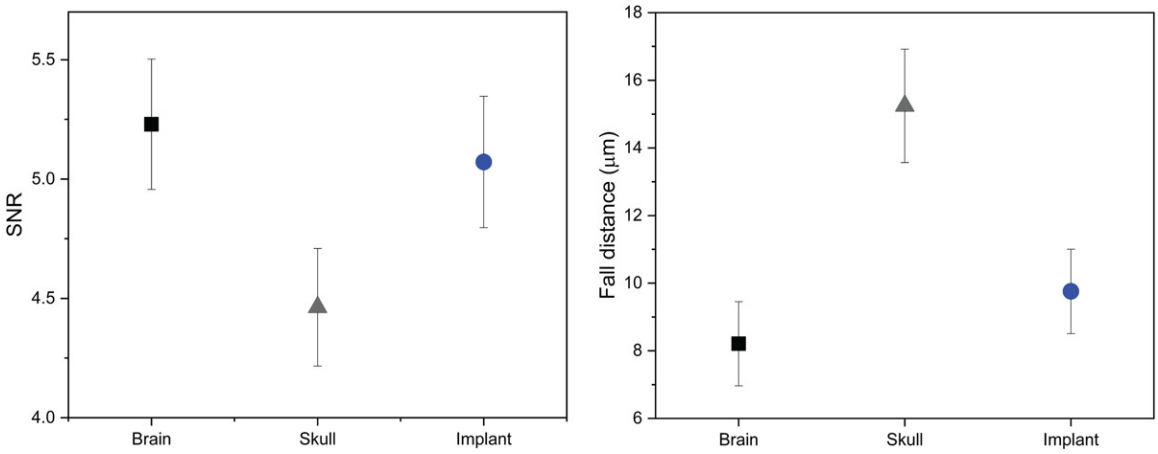

Figure 4.7. (a) Mean signal to noise ratio (SNR) of contrast intensity and (b) mean fall distance of contrast intensity along arbitrary line profiles on the brain, skull, and Window to the Brain (WttB) implant.

Sensitivity was calculated and resulted in 96.82% for the through-implant image (imaging condition 3) and 86.1% for the through-skull image (imaging condition 1). Then, we compared the sharpness (i.e., fall distance) of the vessels in the images to determine if the images were becoming blurred and losing resolution through the WttB implant. The mean fall distance for each imaging condition is shown in Figure 4.7(a). The through-implant contrast image (imaging condition 3) provided 5.7 μm lower fall distance (higher sharpness) when compared with the through-skull contrast image (imaging condition 1).

Assessing Arteriovenous Blood Flow Through-Implant

Figure 4.8 demonstrates the process of arteriovenous cerebral microcirculation image generation and the images obtained through each step. First, an LSI image is acquired, which contains information on vessel structures and relative flow velocities.

The LSI image is also thresholded to provide a contrasted vessel map as a reference vasculature network (step 1). Next, MSRI imaging allows for separating cerebral veins and arteries based on optical extinction spectra over the wavelengths 560–610 nm, and this arteriovenous information is overlaid on the vasculature network LSI image (step 2). Finally, the arteriovenous vasculature network image is weighted by the relative blood flow velocities obtained during the initial LSI imaging in step 1 (step 3).

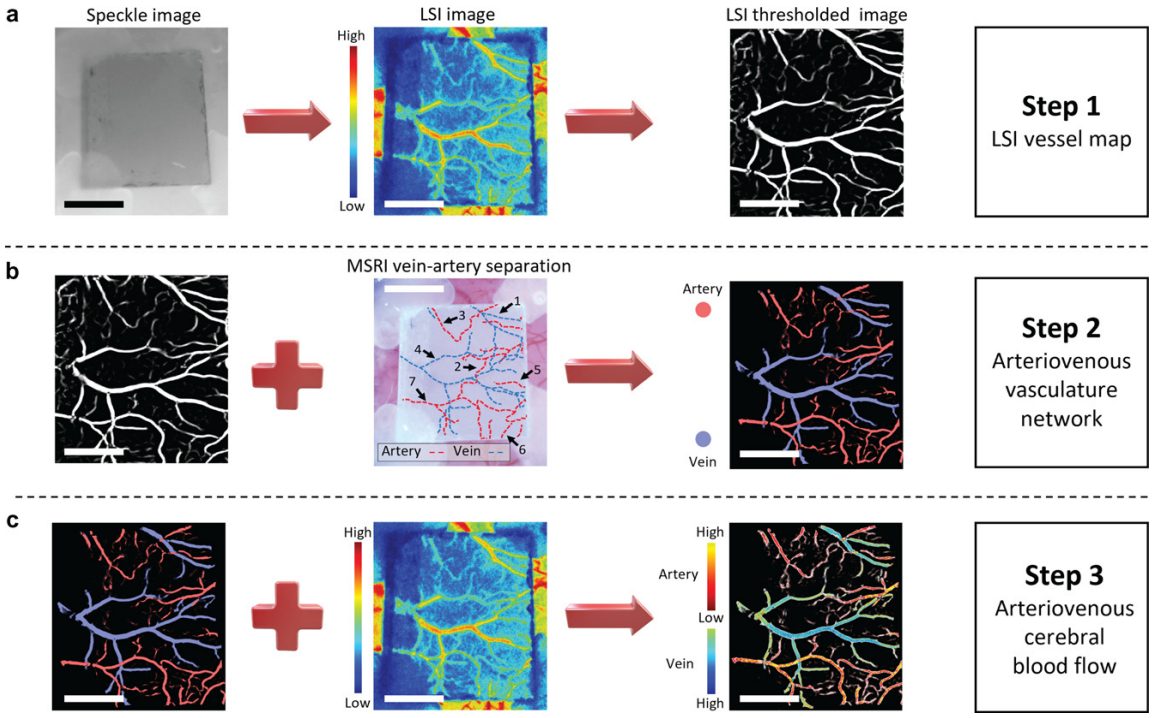

Figure 4.8. The steps of constructing an arteriovenous microcirculation image. (a) Laser speckle imaging (LSI) image obtained by temporal analysis of laser speckle images. The LSI images were then processed to generate the LSI vessel map, where bright is the vasculature network and dark is the non-vascular region (step 1). (b) Arteriovenous information from multispectral reflectance imaging (MSRI) is registered onto LSI vasculature network obtained using LSI (step 2). (c) Arteriovenous vascular network is weighted by the blood flow map (LSI image) (step 3). Bar = 1 mm.

Discussion

In this study we assessed the feasibility of MSRI-LSI imaging of the brain microcirculation through the WttB implant. Other studies have investigated various methods of vein-artery separation, including velocity-based[134], optical attenuation-based methods other than MSRI, and structural-based separation[135]. Besides the various proposed methods based on multi-wavelength imaging[136], like the MSRI approach we used in this present study, Miao et al. distinguished arteries and veins by vascular anatomical features and optical intensity profiles in single-wavelength laser speckle contrast imaging (SW-LSCI) images, but arteries and veins may be misclassified because of similar absorption to the cerebral cortex. Feng et al.[137] proposed an automatic vein-artery separation method based on imaging the exposed cerebral cortex using SW-LSCI, however, the absorption and scattering of underlying parenchyma would also influence the accuracy of the vein-artery separation. Our method for accessing the intrinsic information of blood using MSRI with six wavelengths utilizes more complex instrumentation than many of these other reported methods of vein-artery separation[138]. Our reason for choosing the MSRI method over less complex vein-artery separation methods was that MSRI allows for functional imaging, which can be useful in our future functional brain imaging studies through the WttB implant. However, limitations exist for extracting componential information from intrinsic optical signals (IOSs). Optical properties of blood constituents other than hemoglobin (Hb), may absorb or scatter light,

and these may alter the optical transmission of blood vessels, which can affect the measurement of hemoglobin.

The analysis of the MSRI images acquired through the open craniectomy (condition 2) clearly shows the different spectral behaviors of veins and arteries. For all vessels imaged, veins showed greater optical extinction in wavelengths of 560, 590, 600, and 610 nm, while arteries showed greater optical extinction at wavelengths of 570 and 580 nm. When the brain was imaged through skull (condition 1), only the main vessels were barely visible and analysis of MSRI for the microcirculation was not practical. On the other hand, the MSRI images obtained through the WttB implant (condition 3) resulted in a clear map of the vessels, although some of the microvessels were not visible. Comparing the vessel branches optical extinction shows similar results to the reference data (condition 2). Branches 1 and 4 were detected as vein with higher optical extinction at 560, 590, 600, 610 nm and branches 2, 3, 5, 6, and 7 resulting in higher optical extinction at 570 and 580 nm were thus identified as arteries. This result demonstrates that WttB implant can allow for reliable vein-artery separation imaging. It is worthwhile to mention that the images captured through the WttB implant have lower contrast, which limits the accuracy of the measurements when compared with imaging the brain directly. Lower average of optical extinction values in images through the WttB implant (16.98%) compared with open skull images (22.33%) shows this poorer contrast. Consequently, this lower contrast resulted in lower accuracy of the measurement shown by higher SD of

red and blue groups. Averaged SD of red and blues groups is relatively increased by 33% and 31%, respectively, compared with open skull images.

Temporal contrast imaging has become a useful tool for brain blood flow applications as the images it produces contain functional information (i.e., relative blood velocity) in addition to showing structure of the vessel networks. As we previously reported, exposure time of 6 ms gave the highest SNR for both skull and WttB implant and was used for comparing SNR and sharpness of vessels imaged beneath each. Unlike our previous study with compared two different spatial regions, here the comparison was made between three different imaging conditions. Thus, SNR and sharpness of vessels (fall distance) are evaluated for an identical target. Accordingly, we were able to compare the SNR values of through-implant and through-skull images to the reference image (open skull) to evaluate the sensitivity. This supplementary information to our previous study on SNR further demonstrates that the SNR of through-implant image is higher than that of through-skull imaging. Vessels imaged through the WttB implant have shorter fall distances, while vessels imaged through the skull have greater fall distances, indicating that vessels imaged through the implant have sharper borders compared to those imaged through the skull. As the size of vessels and velocity of blood flow is not expected to differ on average between the two imaging conditions, the apparent increase in vessel diameter imaged through the skull versus WttB implant is likely due to the blurring of the image through the skull. In general, the light transmission to the brain and reflection from the brain are lower in the through-skull image. Additionally, the skull scattering disorders

the speckle pattern that was created by the brain hemodynamics. The skull poses these same issues for the MSRI imaging as well, and because the skull texture is not homogeneous, image correction or enhancement is very complex[114]. The reduction in border sharpness of the vessels imaged through the skull versus WttB implant is consistent with this explanation, and the blurred nature of the through-skull image compared with the through-implant image is visually apparent in Figure 4.3(b). It should also be noted that while the SNR and sharpness of the through-implant images are an improvement over the through-skull images, the mouse skull is inherently transparent itself[114], which is not the case in larger animals or humans.

While vein-artery separation is possible by MSRI alone, in this study we combine MSRI with LSI. The combination with LSI has two major benefits. First, some of the microvessels are not visible through the WttB implant by MSRI since the transmitted light could not overcome the reflected light from the surface of the implant for these visible wavelengths (560–610 nm), and the microvessels have low contrast when compared with larger vessels. Registering the information from the MSRI to the LSI flow map, which does show the microvessels, helped to extend the arteriovenous information to the smaller vessel sizes, which were not visible by MSRI. Second, LSI imaging contains functional information (relative blood velocity), so combining these methods produces vasculature maps, which show relative velocities of flow within the separated arteries and veins. Figure 4.8 contains an example of how this method can produce arteriovenous vasculature network images weighted by relative blood flow velocity.

As seen in Figure 4.3(b), much more precise velocity information, particularly of microvessels, can be detected through the WttB implant, while the reduced sharpness of the vessels imaged through skull obscures precise flow determinations (Figures 4.3(b) and 4.7). Imaging microvessels (usually involving small arteries of less than 150 μm in diameter, arterioles, capillaries, and venules) is important for many applications, as microcirculation plays a critical role in physiological processes such as tissue oxygenation and nutritional exchange. Monitoring the spatiotemporal characteristics of microcirculation is crucial for studying the normal and pathophysiologic conditions of tissue metabolism. It is also useful for assessing microcirculatory dysfunction due to disease conditions such as type 2 diabetes, peripheral vascular disease, atherosclerotic coronary artery disease, obesity, heart failure, Alzheimer's, schizophrenia, and hypertension, among others[139]. In addition, quantification of dynamic blood flow, angiogenesis, and vessel density are critical for monitoring the progression of wound healing[140]. Although high-resolution vascular network mapping is possible using imaging modalities such as CT, these approaches require injection of contrast agents and pose disadvantages such as radiation exposure. Existing noninvasive methodologies (including LSI through skull) are inadequate to study blood flow at microvessel resolution[122]. Windows such as the WttB implant are thus important tools for research, and in the case of the WttB implant can become important enablers of clinical diagnostics and therapy involving cerebral microvessels.

There are several limitations to the current study. The sample size used was small ($n = 1$), and further experiments are needed to confirm the reproducibility of these findings. While a permanent cranial implant can allow for less invasive imaging of the brain at later time points, it requires an initial implantation surgery, which carries associated risks such as infection.

In conclusion, this study has demonstrated the ability to perform MSRI-LSI across a transparent cranial implant, to allow for cerebral vessel networks to be mapped, including microvessels. These images contain additional information such as vein-artery separation and relative blood flow velocities, information which is of value scientifically and medically. The WttB implant provided substantial improvements over imaging through the murine cranial bone, where microvessels are not visible and MSRI cannot be performed.

Acknowledgments

I would like to acknowledge the contribution of my co-authors to this work: Mildred S. Cano-Velázquez, David L. Halaney, Carrie R. Jonak, Devin K. Binder, and Guillermo Aguilar. This work was supported by National Science Foundation (NSF-PIRE) (1545852) and “Beca Mixta” from National Council of Science and Technology of Mexico (CONACYT) (741249). The authors would like to thank Gottlieb Uahengo for the fabrication of the YSZ samples.

Chapter 5. Enhanced near infrared optical access to the brain with WttB implant and scalp optical clearing

The brain is protected by different tissue layers, each of them having different optical properties (e.g., refractive index contrast, scattering and absorption); hence, the analysis of the spectral features provide information about these different layers[54]. Furthermore, it has been shown that physiological changes in the different head tissues produce variations in their optical properties thereby changing the spectral features of the transmitted and reflected light[47]. Compared to visible light, some spectral regions in the Near Infrared (NIR) spectral range (800 to 2500 nm) offers advantages such as reduced scattering and absorption as well as a deeper penetration depth in tissue media[48,49]. Because of these features, some spectral windows within the NIR wavelength range have shown promising results for brain studies, including deep imaging, diagnostics and therapeutic applications in brain diseases[51].

Different optically transparent windows for head tissues have been identified within the NIR spectral range. These wavelength windows avoid light attenuation by the tissue due to water absorption peaks located at 1450 nm and 1940 nm[55]. The first window NIR-I (~700−1000 nm), or conventional window, has been well characterized and studied for most tissues, including brain and other soft tissues. Two additional optical windows have been also identified: NIR-II (~1000−1350 nm) and NIR -III, or short -wave infrared SWIR, (~1550−1870 nm); the latter spectral region has shown to provide maximum light penetration for some kinds of tissues[141]. More recently, a fourth optical

window, SWIR-II (~2100−2300 nm) has allowed for improved optical studies of the brain and for deep brain imaging, particularly when compared to the NIR -II window[53]. All of these spectral regions have been explored for many biophotonic applications, although the NIR windows have particularly shown excellent potential for noninvasive through-skull *in vivo* brain imaging and spectroscopy[52]. Nonetheless, it is always desirable to reduce the highly scattering cranial bone over the cortex, which hinders the observation of optical signals deriving from deeper tissues and reduce the light penetration distance.

In this chapter, we report on the enhancement in optical access provided by the transparent YSZ implant for brain studies in the NIR wavelength range. Because this cranial implant is sought as a means to obtain optical access for post-operatory and prolonged diagnostics and/or therapy purposes, scalp scattering must be overcome. In this context, we also evaluate the use of optical clearing agents (OCAs) in the scalp, particularly their effects on the optical transmittance in the NIR spectral range. As shown in previous reports, OCAs provide greater optical probing depths and better contrast, as well as improved light focusing and spatial resolution[142–144]. Therefore, evaluation of the optical features of the YSZ implant together with the use of OCAs in the NIR spectral range will provide useful information for theranostics applications operating in this wavelength range (e.g., photobiomodulation[57–59], NIR and fluorescence imaging[145], cancer diagnosis[146] and brain edema[147]). Hence, we evaluate the enhancement in optical access to the brain upon comparing ex-vivo transmittance measurements of mice native skull and

the YSZ cranial implant coupled with scalp and OCAs. Using the transmittance data, the total attenuation lengths were calculated showing that this combination (YSZ and OCAs) offers the best option for gaining improved optical access to the brain.

Methods

Scalp and skull samples

The tissue samples were obtained from animals from the University of California, Riverside (UCR). All experimental procedures and humane care of mice were conducted under a protocol approved by UCR's Institutional Animal Care and Use Committee, and in conformance with the Guide for the Care and Use of Laboratory Animals published by the National Institutes of Health (NIH Publication No. 85-23, revised 1996). The N=9 8-12 week old C57Bl/6 male mice (Jackson Laboratory) used in this study were housed under a 12-hour light and 12-hour dark cycle with ad libitum access to food and water.

Surgical procedures

Craniectomy surgery was conducted as previously described. Briefly, mice were anesthetized with isoflurane inhalation (0.2-0.5%), and given ketamine and xylazine (K/X) (80/10 mg/kg, i.p.). Additional anesthetic was administered as necessary. Hair was removed from the scalp using clippers and depilatory cream. Mice were then secured into stereotaxic frames to immobilize the head for surgery. Ophthalmic ointment was placed over the eyes, and the surgical site was sterilized with alternating application of betadine and 70% EtOH (3 times). A sagittal incision was made to the left of the midline, and the scalp excised to expose the skull. Periosteum was removed from the skull, and a

craniectomy was performed with a surgical drill and carbide burr to remove a square section of skull over the right parietal lobe, with dimensions slightly larger than the implant (2.6 x 2.6 mm).

Optical clearing

A mixture of two biocompatible agents, PEG-400 (PEG) and Propylene Glycol (PG) (Fisher Scientific, California, US), were used as scattering reducer and penetration enhancer, respectively, at a volume ratio of 9:1[148,149]. The OCA was prepared and topically applied at room temperature. A thin layer of the OCA was applied on the sample and remained for 50 minutes[148]. Characterization experiments were performed before and immediately after applying the OCA; the increase in transmittance for each tissue used in the samples was monitored every minute over a 50-minute period. For our experimental conditions, the maxima in transmittance were achieved within 50 minutes.

Tissue characterization

Optical transmittance measurements of the different samples used in this study were obtained through optical spectrometry in the NIR. The setup used to obtain the transmittance spectra incorporates two multimode optical fibers (P400-2-VIS-NIR, Ocean Optics, FL) attached to individual fiber holders including VIS-NIR collimating lenses (MP-74-UV, Ocean Optics, FL, with focal length f = 10mm, lens diameter D = 5mm and N A = D/2 f = 0.4). As depicted in Figure 5.1, the holders were attached to a mechanical rail allowing to adjust the separation between the fibers and to allocate a sample holder. After the sample is fixed, the fiber holders were tightly joined together to

mitigate detrimental effects from ambient light and back reflections. The light source used for these measurements was a visible-NIR source (HL2000 FHSA, Ocean Optics, FL) launched into one of the optical fibers. The beam exiting the launching fiber then traverses the sample and is collected by the other fiber, which is connected to a solid-state spectrometer (NIRQUEST 520, Ocean Optics, FL) to obtain the optical transmission spectra. Spectra were acquired averaging 10 measurements, with an integration time of 300 ms, in the 900-2400 nm wavelength range.

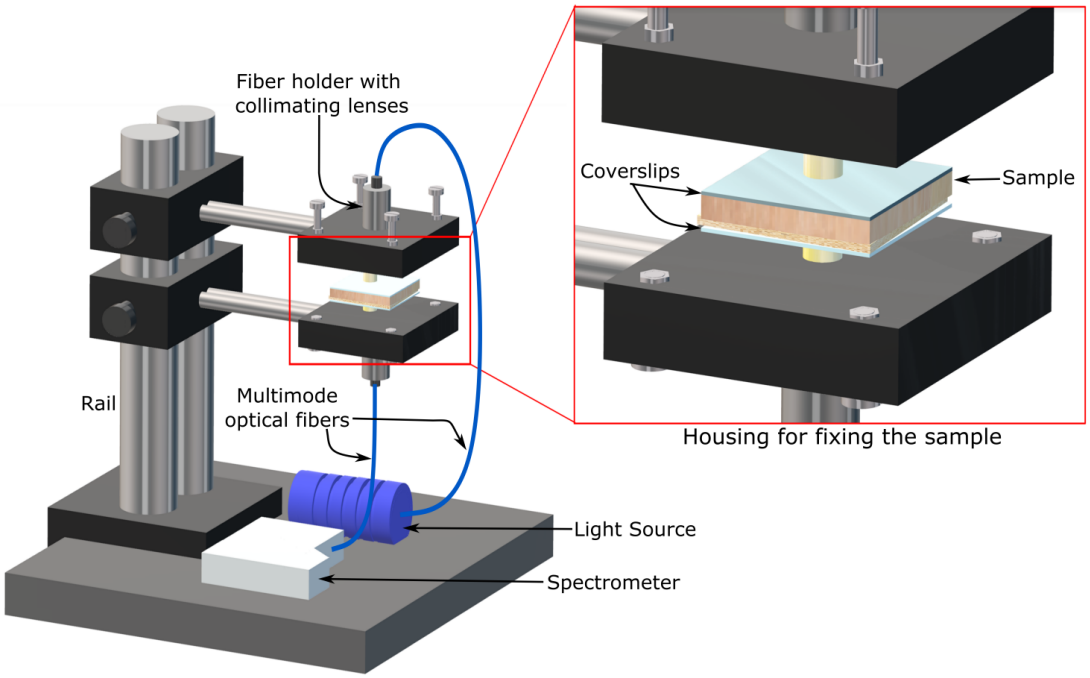

Figure 5.1. Collimated transmittance measurements setup. The inset shows the housing for fixing the sample, i.e., the fiber holders with the VIS-NIR collimating lenses. As seen in the inset, the samples are placed between coverslips (see text for further details).

For all the measurements, the collimated transmittance (T(λ)) was calculated as the ratio of light transmitted through the sample to the total incident light, i.e.:

$$T(\lambda) = \frac{S(\lambda) - D}{I(\lambda) - D} \tag{5.1}$$

where λ is the wavelength, S is the measured spectral intensity, I is the total light incident and D represents the reference reading under dark conditions (i.e., no light impinging on the sample). Basic models of light propagation in biological tissues are described in terms of radiation transport in a random inhomogeneous media, which includes ballistic and diffuse light. However, when using a collimated beam, and in the case of thin samples with large absorption coefficients and relatively small light scattering, the ballistic part plays a dominant role and the diffusive part is negligible[47,50,53,150]. We further consider that the ballistic photons in the scattering samples are governed by the Beer-Lambert law. Hence, for analyzing the influence of the sample thickness z in the spectral transmittance, the total attenuation length (lt(λ)) was calculated as[47,50,53,150]:

$$l_t(\lambda) = \frac{z}{-ln(T(\lambda))} \tag{5.2}$$

Note that the attenuation length takes into account the sample thickness and therefore provides a better insight of the light penetration through the samples. In particular, for our experiments, the thicknesses of the samples are: 440 ± 1μm, 159 ± 1μm and 710 ± 20μm for the YSZ implant, the mice skull and scalp, respectively. Hence, the YSZ implant is 2.5 times thicker than the mice skull.

Experimental method

The experimental procedure for measuring the ballistic transmittance through the different tissues and the implant was similar to those reported previously for spectroscopic measurements on soft tissue[47,50,53,150]. Transmittance measurements were obtained for three sets of samples arranged as the different scenarios illustrated in Figure 5.2. Spectra were obtained first for the skull and subsequently for the stacked array formed by the scalp placed on top of the skull. The OCAs were then applied on the scalp and the spectral transmittance was acquired once again. This set of measurements were also performed using the YSZ implant instead of the skull. The stacking arrangement used for this measurements allowed for evaluating the effects of each layer on the spectral features of the sample. This further allows for comparing the spectral features of the skull and the YSZ implant under similar conditions. Excised full thickness scalp and forehead cranial bone were rinsed briefly in saline solution to remove the excess blood and their thicknesses were measured before placing them in the stacked samples. These were finally placed between two glass microscope coverslips to obtain the transmittance spectra. The same procedure was followed for the YSZ implant. For the cleared skin measurements the scalps were topically exposed to PEG and PG as a scattering reducer and a penetration enhancer, respectively[148,149].

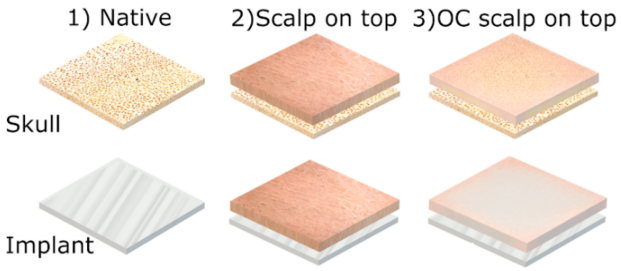

Figure 5.2. Stacked sample arrangement used to obtain the spectral transmittance of: 1) the native skull and YSZ implant, 2) the scalp on top of the skull and the YSZ implant, 3) optical cleared (OC) scalp on top of native skull and implant.

Results and Discussion

Figure 5.3 shows the transmittance (T(λ)) and the attenuation length (lt(λ)) calculated for the native skull and the implant. The transmittance measurements (Figure 5.3(a)) show that the YSZ implant is more transparent throughout the tested NIR range (900-2400 nm) including all of the optical windows commonly used for biophotonic applications (i.e., NIR I, NIR II, SWIR I and SWIR II). This is due to the significant reduction in scattering and absorption when using the YSZ implant. In terms of relative differences in the optical properties between skull and the implant, the latter improves the light transmission within the water absorption bands owing to its reduced water content compared to the native skull (70-75%). The skull transmittance shows the typical water absorption bands in the NIR spectral region (1450 nm and 1940 nm), while the YSZ implant shows improved transmittance in these bands. The water absorption peaks apparent in the implant spectrum are due to traces of the saline solution used for rinsing aiming at obtaining a fair comparison with the treated tissue samples. A simple

calculation of the increase of light transmitted in these bands using the YSZ implant compared to the native skull yields values of 47% at 1450 nm and 53% at 1940 nm. The resulting attenuation length shown in Figure 5.3(b) further indicates that, even for the spectral regions with the smallest increase in transmission (e.g., 3% at 1300 nm), light can penetrate deeper when compared to the native skull. Clearly, with exception of the second water absorption band, the attenuation length obtained with the implant increases at least by 1.3 mm, i.e., a four-fold increase in length compared to the skull The spectral regions covered by the water absorption peaks in the NIR have not been explored for through-skull techniques because of its high water content. Thus, the improved transmission obtained with the implant opens the possibility to explore new techniques in these wavelength ranges.

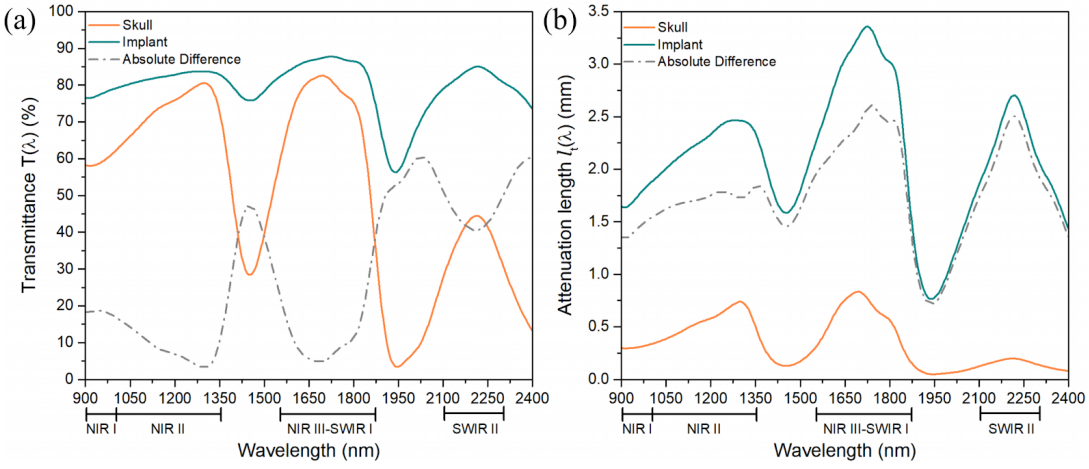

Figure 5.3. Transmittance (a) and total attenuation length (b) for the skull and the YSZ implant. The YSZ implant shows better transmittance throughout the full 900-2400 nm spectral range compared to the native skull.

The effect of the scalp on the spectra is evident in Figure 5.4(a), showing a considerable reduction in transmission owing to the increased scattering inherent to this tissue[47]. As shown in Figure 5.4(b), this leads to reduced attenuation lengths for both sample arrangements, i.e., scalp either on top of the skull or on the YSZ implant. Although for both cases the scalp stacking leads to a reduction in transmittance of at least 60%, the sample with the implant still provides the best performance, as confirmed by the attenuation length. Throughout all the spectral range, the sample formed with the scalp and the YSZ implant provides improved light penetration. Clearly, the scalp introduces large optical attenuation effects that must be overcome for the implant to become a convenient means to obtain access for non-invasive optical techniques for post-operatory diagnostics and/or therapeutic purposes. Hence, we evaluated the use of OCAs as a technique for improving the transmittance of the samples.

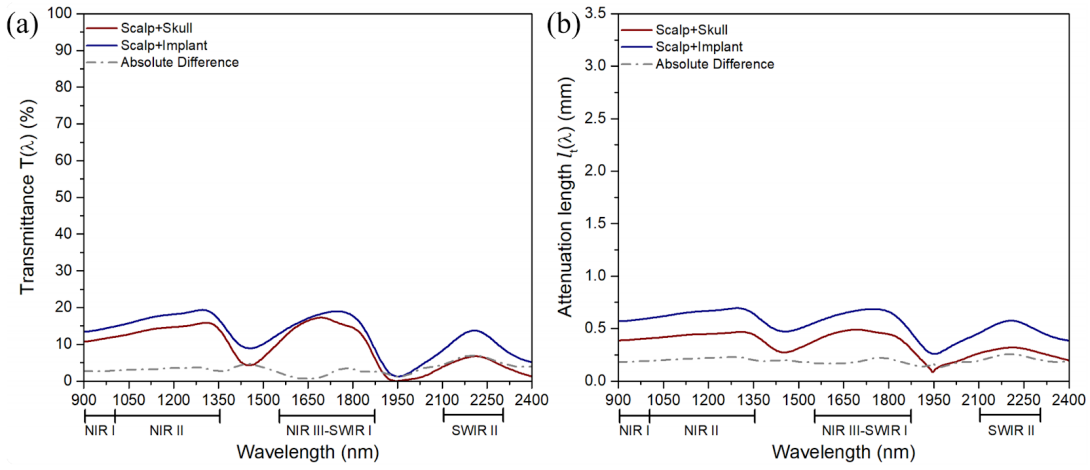

Figure 5.4. Transmittance (a) and total attenuation length (b) comparing the stacked samples of the scalp on top of the skull and on the YSZ implant. The sample with the YSZ implant still shows better transmittance and improved attenuation length compared to the sample with the native skull; however, the enhancement is only of 6% in the best case.

The effects of applying a layer of OCAs on the scalp are evident in Figure 5.5; the transmittance spectra increases by 20% for the sample with the skull, while for the YSZ implant the enhancement is 40% (Figure 5.5(a)). As shown in Figure 5.5(b), the attenuation length for both samples increases accordingly; when compared to the results shown in Figure 5.4(b), it is clear that the OCAs effectively enhance the light penetration yielding larger attenuation lengths throughout the whole NIR range for both samples. Further comparison of this parameter for the two samples show that the YSZ provides improved light penetration than attained with the skull (up to 1.8 mm more at 1717 nm). These results are consistent with previous reports involving OCAs[142–144], and further confirm that together with the YSZ implant, these biocompatible agents provide attractive features for optical access to the brain tissue without scalp removal.

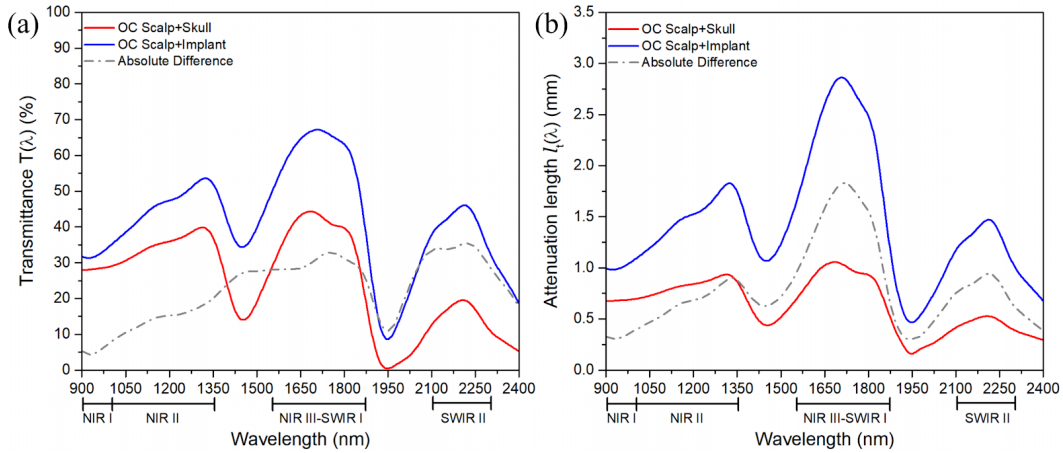

Figure 5.5. Transmittance (a) and total attenuation length (b) comparing the stacked samples of the scalp on top of the skull and on the YSZ implant after using the OCAs. The sample using the YSZ implant with optically cleared scalp (OC scalp) shows an increase of up to 30% in transmittance compared to the sample with the skull.

A better idea of the impact of our results in each of the NIR optical windows can be appreciated in Figure 5.6, showing a summary of the transmittances and attenuation lengths obtained from our experiments. Comparing all the scenarios, the YSZ implant provides the best option for optical access, showing the largest transmittance and attenuation length. Although the transmittance for the YSZ is seemingly comparable to that of the skull for the NIR II and NIR III windows, the attenuation lengths for the implant are clearly larger than those obtained for the skull (Figure 5.6(b)). In fact, for all the windows, the YSZ implant offers improved features and thus better potential for deeper optical access to the brain tissue, even when using the scalp on top. When using OCAs to reduce the scattering of the scalp, the YSZ implant offers improved transmittance and larger attenuation lengths than those observed for the skull. Remarkably, the attenuation lengths achieved with the OCAs and the YSZ show at least a two-fold increase for the last three windows (i.e., NIR II, NIR III-SWIR I and SWIR II). Evidently, the optical features offered by the YSZ implant together with the use of biocompatible agents to reduce scalp scattering pose new possibilities for probing brain tissue in spectral regions that are commonly discarded owing to the low penetration depths that can be commonly achieved[50]. Note that these results provide a direct comparison of the attenuation lengths achieved when replacing the mice skull by the YSZ implant. It is evident that the transparency of the YSZ implant improves the light penetration, but the ultimate increase in penetration depth achievable will depend on the scattering features of the specific bone tissue. Further considerations for the analysis of

the spectral transmission should include the diffuse light component, which is relevant when using thicker and more absorbent tissue samples (e.g., rat skull[50]).

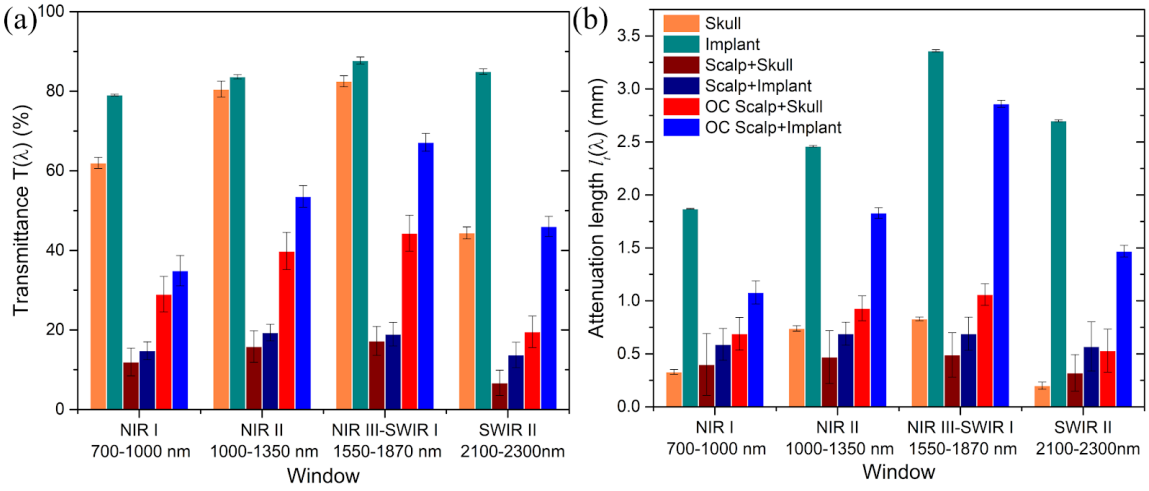

Figure 5.6. Summary of the registered transmittance (a) and total attenuation length (b) for the different samples tested in our experiments. Throughout the whole NIR spectral range the YSZ implant shows enhanced transmittance among all the samples. The use of OCAs on the scalp effectively increases both, the transmittance and the attenuation length, providing enhanced light penetration. The most favored optical window for the stacked sample of optically cleared scalp on top of the YSZ implant is the NIR III (1550-1870 nm, T=67%, lt= 2.86 mm). Error bars represent standard deviation (n=3).

The enhanced transparency of the YSZ implant coupled with the OCAs shows promising features to facilitate various NIR techniques for theranostics. Photobiomodulation (600-1064 nm), NIR and fluorescence imaging (700-1700 nm), as well as some types of cancer diagnosis (1500-1800 nm) and brain edema are a few examples of optical techniques that could benefit from the improved transmission in NIR spectral range offered by the YSZ implant. Additionally, any potential adhesion of biochemical agents and/or tissue growth on the implant (e.g., fibrotic tissue, proteins, cell

adhesion) could be potentially monitored over time using IR reflection techniques[25]. Imaging techniques (e.g., LSI, fluorescence, absorption) that have been successfully demonstrated to improve with clearing and thinning skull methods[33], may also benefit from the combination of the OCAs and a transparent YSZ implant.

We have evaluated the optical transmission and attenuation length of a novel YSZ-based implant intended for chronic optical access to the brain performing ex-vivo transmittance measurements. In addition, the use of OCAs to overcome the low transparency of the scalp was explored together with the implant. Direct comparison of the YSZ implant with mouse skull in different stacked arrangements showed that this ceramic material offers enhanced transmission throughout the NIR spectral range. Furthermore, since OCAs effectively reduce the scattering features of the scalp, the use of these biocompatible agents together with the YSZ implant provide improved optical features. In particular, when compared to a typical arrangement comprised of scalp and native skull, the use of the YSZ implant yields an increase in transmittance of up to 50% and attenuation lengths of up to 2.4 mm (i.e., a five-fold increase in light penetration). These experimental results show evidence that the YSZ implant, when used together with the OCAs, offers the best option for gaining improved optical access to the brain. This novel approach seeks to provide new opportunities for monitoring brain conditions on a chronically recurring basis, without requiring repeated craniotomies or scalp removal. Although this study represents only the first step towards the application of NIR optical

techniques for brain theranostics through an implant, it offers a relevant insight of the opportunities that this transparent material may eventually provide.

Acknowledgments

I would like to thank the first author of this study, Mildred S Cano-Velázquez. I also thank contributions of the coauthors: David Halaney, Carrie R. Jonak, Devin K. Binder, Juan Hernández-Cordero, and Guillermo Aguilar. The authors would like to thank Gottlieb Uahengo for the fabrication of the YSZ samples. This study was supported by Conacyt-FONCICYT (246648); Conacyt-'Beca Mixta'(741249); and National Science Foundation (NSF) (NSF-PIRE 1545852, NSF-EAGER 1547014).

Chapter 6. Through-Scalp Light Delivery and Microcirculation Imaging

Background

Providing optical access in visible (VIS) wavelength range to the human brain for light delivery and microcirculation imaging is complicated due to the static and dynamic effects of optical scattering and absorption (particularly in hemoglobin absorption picks) by the inhomogeneous skull and scalp tissues. Therefore, VIS light-based brain studies has been predominantly demonstrated in rodent open-skull and thinned skull models. In this Chapter I report on the VIS light delivery through the WttB implant. The enhancement in optical access to the brain using scalp optical clearing and WttB implant is evaluated through *ex vivo* optical transmittance measurements. We also performed *in vivo* brain microcirculation imaging in mice using laser speckle imaging (LSI).

Methods

Transparent stabilized-zirconia cranial implants

Transparent nanocrystalline 8 mol% $YO_{1.5}$ yttria-stabilized zirconia (nc-YSZ) implant samples were produced as explained in Chapter 2[63]. The thickness of the resulting densified YSZ discs were reduced from 1 mm to ~440 μm by polishing with 30 μm diamond slurry on an automatic polisher (Pace Technologies, Tucson, Arizona, USA). The samples were then polished with successively finer diamond and silica slurries ranging from 6 to 0.2 μm. Samples were sectioned into rectangles of approximately 2.1 x 2.2 mm using a diamond lapping saw (WEIYI DTQ-5, Qingdao,

China), followed by sonication in acetone and thorough rinsing in water. Optical, mechanical, and ageing properties of the material were reported previously [38,63,74].

Animals

N=12 C57BL/J6 WT (#000664) mice were obtained from Jackson Laboratories. Animals were maintained under a 12-hour light/dark cycles and were provided food and water *ad libitum*. All experiments were performed with approval from the University of California Animal Care and Use Committee and in accordance with the National Institute of Health Animal Care and Use Guidelines. Males between 8 – 12 weeks of age were used in this study.

Preoperative surgical preparation and anesthesia

Mice were anesthetized with isoflurane inhalation (0.2-0.5%) and given an i.p. injection of ketamine and xylazine (K/X) (80/10 mg/kg). Mice were aseptically prepared for surgery and secured in a stereotaxic apparatus. Artificial tear ointment was applied to the eyes to prevent drying. Toe pinch reflex was used to measure anesthetic depth throughout the experiment, and supplemental doses of K/X were administered as needed.

Optical clearing agent

A mixture of two biocompatible chemicals, PEG-400 (PEG) and Propylene Glycol (PG) (Fisher Scientific, California, US), were used as scattering reducer and penetration enhancer, respectively, at a volume ratio of 9:1 at room temperature[148,149].

Ex vivo proof of concept: optical transmittance measurements

Scalp and skull tissue acquisition and preparation

A sagittal incision was made to the left of the midline, and a square section of the scalp was excised. Periosteum was removed from the skull, and a craniectomy was performed with a surgical drill and carbide burr to excise a square section of skull over the right parietal lobe, with dimensions of 2.6 x 2.6 mm. Excised full thickness scalp and cranial bone from above the right parietal lobe were rinsed briefly in saline solution to remove excess blood. The thicknesses of the samples were measured to be 440 ± 1μm, 159 ± 1μm and 710 ± 20μm for the YSZ implant, the mice skull and scalp, respectively. Hence, the YSZ implant is 2.5 times thicker than the mouse skull. Following excision of tissue, mice were euthanized by intraperitoneal (I.P.) injection of pentobarbital solution.

Optical transmittance measurement setup

Optical transmittance measurements of the different samples used in this study were obtained through optical spectrometry. The setup used to obtain the transmittance spectra incorporates two multimode optical fibers (P400-2-VIS-NIR, Ocean Optics, FL) attached to individual fiber holders including visible-NIR collimating lenses (MP-74-UV, Ocean Optics, FL, with focal length f = 10mm, lens diameter D = 5mm and NA = D / 2f = 0.4). As depicted in Figure 5.2(b), the holders were attached to a mechanical rail allowin0g for adjustment of the distance between the fibers and to incorporate a sample holder. After the sample was secured within the holder, the fiber holders were tightly joined together to mitigate detrimental effects from ambient light and back reflections.

The light source used for these measurements was a visible-NIR source (HL2000 FHSA, Ocean Optics, FL) launched into one of the optical fibers. The beam exiting the launching fiber then traverses the sample and is collected by the other fiber, which is connected to a solid-state spectrometer (SD2000, Ocean Optics, FL) to obtain the optical transmission spectra. Spectra were acquired averaging 10 measurements, with an integration time of 300 ms, in the 450-900 nm wavelength range. For all the measurements, the collimated transmittance (T(λ)) was calculated as the ratio of light transmitted through the sample to the total incident light (Equation 5.1). Equation 6.1 shows how relative change in transmittance was calculated,

$$\textit{Relative transmittance change}\ (\%) = \frac{\left|T(\lambda) - T(\lambda)_{Reference}\right|}{T(\lambda)_{Reference}} \tag{6.1}$$

A set of photographs of a resolution target imaged through a scalp tissue was also captured before and up to 40 minutes after applying the OCA using a metallurgical microscope (MT 8530, Meiji Techno, Japan).

Experimental design

The procedure used for measuring the ballistic transmittance through the different tissues and the implant was similar to procedures reported previously for spectroscopic measurements on soft tissue [53,150,151]. Three sessions of measurements were performed. In each session, optical measurements were repeated n=3 times using freshly excited samples from 3 new mice. All of the samples were placed between two glass microscope coverslips to obtain the transmittance spectra. In the first session, scalp and skull samples

were excised (from Mice 1-3) and optical transmittance of single layer samples were measured (Figure 6.1(a), left column). After obtaining implant, skull, and scalp spectra, a thin layer of the OCA was applied on the scalp and the optical transmittance of optical cleared scalp (OCS) was measured every minute over a 50-minute period [148,149]. Stacking arrangements were then used for the second and third sessions of measurements allowing for evaluating the effects of each layer on the spectral features of the sample. This further allows for comparing the spectral features of the skull and the YSZ implant under similar conditions. In the second session, 3 new scalp and skull samples were excised (from Mice 4-6) and spectra were obtained for the stacked arrays of the scalp placed on top of the skull (Figure 6.1(a), middle column). Then, the OCA was applied on the scalp and samples (OCS+skull) were measured over time. In the third session of measurements, 3 new scalp samples were excised (from Mice 7-9) and the stacked array of the scalp placed on top of the implant was measured (Figure 6.1(a), right column). Then, the OCA was applied on the scalp and samples (OCS+implant) were measured over time.

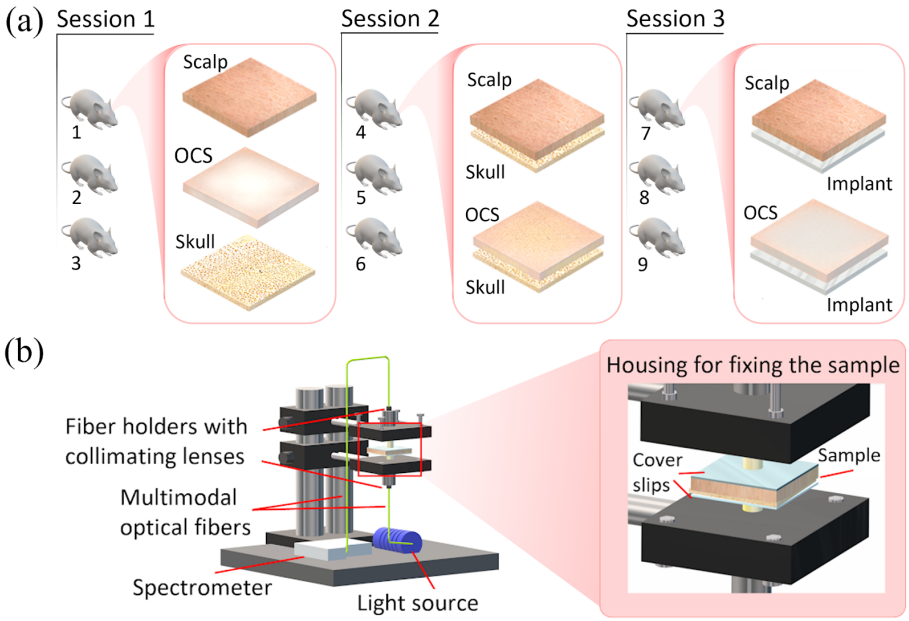

Figure 6.1. Optical characterization experimental setups. a) Samples used in the *ex vivo* optical characterization including single layer samples of skull, scalp, and OCS (left column); stacked sample arrangement of scalp/OCS+skull (middle column); and stacked sample arrangement of scalp/OCS+implant (right column). b) Collimated transmittance measurements setup. The inset shows the housing for fixing the sample placed between coverslips.

In vivo LSI Imaging of Microvasculature

Mouse model preparation

The mouse model for this study was designed to provide optical access to the right parietal lobe of the brain through the OCS and WttB implant (Figure 6.2(a)). A sagittal incision was made to the left of the midline, and the scalp retracted to expose the skull (Figure 6.2(a)). Periosteum was removed from the skull, and a craniectomy was performed with a surgical drill and carbide burr to remove a square section of skull over the right parietal lobe, with dimensions slightly larger than the implant (Figure 6.2(a), inset I and II). The YSZ implant was placed within the craniectomy directly on the intact

dura mater, and dental cement was applied to each of the four corners of the implant to prevent displacement (Figure 6.2(a), inset III). Dental cement was cured with blue light exposure for 20 seconds. Imaging with LSI was conducted before and after opening the scalp (imaging conditions 1 and 2, respectively), immediately after the craniectomy procedure, while the scalp was still open (imaging condition 3), and after the implantation (imaging condition 4). Then, the retracted scalp was placed back over the implant and a ring-shape barrier (for holding OCA) was made on top of the scalp using dental cement and cured with blue light (Figure 6.2(a), inset IV). LSI imaging was conducted before and immediately after carefully adding a drop of OCA inside the dental cement holder (imaging conditions 5 and 6, respectively).

Laser speckle imaging setup

For LSI, an 810 nm continuous wave NIR laser (DL808-7W0-O, CrystaLaser, Reno, NV, USA) was used to illuminate the region of interest with an incident power of 100 mW at a 45° incidence. While most LSI studies use visible wavelengths for illumination, we chose 810 nm to reduce reflectance and increase transmittance through the WttB implant [24]. The 810 nm laser was expanded using a pair of negative-positive lenses (KPC043, −25 mm EFL and KPX094, 100 mm EFL, Newport, Irvine, CA, USA) and speckles were generated and homogenized using an engineered diffuser (ED1-C20-MD, Thorlabs, Newton, NJ, USA). Diffused laser light was shown onto the intact scalp (i.e. condition 1), onto the intact skull (i.e. condition 2), onto the dura mater and cortex after craniectomy (i.e. condition 3), through the WttB implant (i.e. condition

4), onto the closed scalp (i.e. condition 5), and onto the closed scalp after applying the OCA (i.e. condition 6). The crossed polarized (LPVIS100, Thorlabs, Newton, NJ, USA) reflected light from the illuminated region was captured by a 12-bit CMOS camera (DCC1545M, Thorlabs, Newton, NJ, USA) equipped with a 10X zoom microscope (MLH-10X, 152.4 mm WD, Computar, Torrance, CA, USA). The aperture and magnification of the zoom microscope were carefully chosen to ensure that the speckle size at the image plane was approximate to the area of two pixels in the CMOS chip. A schematic of the imaging system is shown in Figure 6.2(b). For each imaging condition, a sequence of 100 laser speckle images were captured at exposure time of 6ms (per our previous report on optimized LSI exposure time) [24] at a speed of 14 frames per second. Then, the laser speckle images were analyzed to obtain the contrast image.

Image processing and data analysis

The contrast-resolved LSI images were constructed based on temporal statistical analysis of laser speckle which has been proven to preserve spatial resolution [114]. Experimental results have indicated that temporal speckle contrast analysis could expressively suppress the effect of the static laser speckle pattern formed by the stationary superficial reflection and scattering tissue on the visualization of blood flow [108,114,152]. Suppressing this effect makes temporal contrast analysis an ideal method for imaging cerebral blood flow, and in this study we assess whether this method can resolve blood flow across the skull, scalp, OCS, and implant. The temporal contrast, K_t, of each image pixel in the time sequence was calculated using Equation (6.2) [108],

$$K_t(x,y) = \frac{\sigma_{(x,y)}}{\langle I_{(x,y)} \rangle} = \sqrt{\frac{1}{(N-1)}\left\{\sum_{n=1}^{N}[I_{(x,y)}(n) - \langle I_{(x,y)} \rangle]^2)\right\}} \Big/ \langle I_{(x,y)} \rangle \quad (6.2)$$

where $I_{x,y}(n)$ is the CMOS counts at pixel (x,y) in the nth image, N is the number of images acquired, and $\langle I_{x,y} \rangle$ is the mean value of CMOS counts at pixel (x,y) over the N images. The raw images were process to obtain the contrast image. The contrast images across the height positions were compared to find the correctly focused plane (associated with the highest contrast) for each imaging condition.

We assessed the quality of the speckle contrast images over the imaging conditions in terms of signal-to-noise ratio (SNR) and vessel sharpness. To quantify signal to noise ratio for each imaging condition, the contrast intensity profile along a vertical line (across the blood vessels) was considered. To avoid selection bias, the location of these line profiles were chosen arbitrarily at the region of interest (ROI) mid-points. The midlines intersected 3 to 4 vessels, and remained the same between the imaging conditions. Equation (6.3) shows how SNR values were calculated for each imaging condition,

$$SNR = \Delta K / \sigma K_n \quad (6.3)$$

where ΔK is the depth of the vessel peak from the baseline (mean noise) and σK_n is the standard deviation of the noise. The SNR values were averaged over the mice (10, 11, and 12) and standard error (SE) were calculated. Sensitivity, which is considered as the

ratio of the mean SNR to the mean SNR of the reference, was calculated using Equation (6.4).

$$Sensitivity = \frac{SNR_{imaging\ condition\ n}}{SNR_{imaging\ condition\ 3}} \tag{6.4}$$

As an indicator of resolution, we compared the sharpness of the vessel edges in images by calculating fall distance (the number of pixels multiplied by the pixel size (~3 μm)) of the edge of the vessel to go from 10% to 90% of ΔK value [131]. A shorter fall distance corresponds to greater sharpness. The same sampled contrast intensity profile lines were considered for the fall distance calculation. To consider the vessel sizes while comparing SNR and fall distance, full-width half-max (FWHM) of the vessels in profiles were taken as the vessel diameter [153].

Experimental design

A session of *in vivo* brain imaging using LSI was performed on 3 new mice (referred to hereafter as Mice 10-12) (Figure 6.2(a)). *In vivo* LSI through the six imaging conditions of intact scalp (i.e. condition 1), intact skull (i.e. condition 2), direct-brain (i.e. condition 3), implant (i.e. condition 4), scalp+implant (i.e. condition 5), and OCS+implant (i.e. condition 6) were performed in succession in each of the mice (n=3).

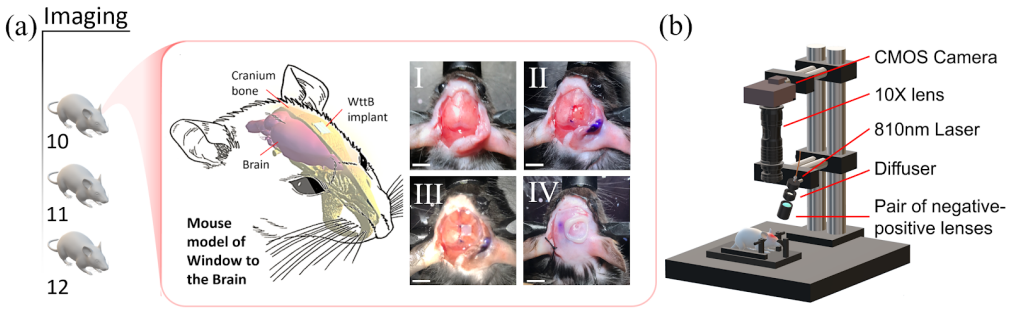

Figure 6.2. a) The mouse model used for LSI *in vivo* imaging. In the inset, a schematic of the mouse head illustrating the location of the optical access is shown. Surgical preparation steps including retracted scalp to expose the skull (I), craniotomy and implantation (II, III), and replacing the scalp and making a ring-shaped OCA holder (IV) are also shown in the inset (scale bars = 4 mm). b) Experimental imaging setup.

Statistical analysis

Data from *ex vivo* optical transmittance measurements and *in vivo* imaging were expressed as mean and SE and tested statistically by a two-sided t-test through the software Origin 2018 for Windows. The significance level was set at $p < 0.05$.

Results

Ex vivo proof of concept: optical transmittance measurements

Figure 6.3(a) illustrates the spectrotemporal effect of OCA on scalp. Absolute change in the optical transmittance spectra (referenced to baseline before applying OCA) for up to 50 minutes after applying OCA is shown in Figure 6.3(a). A primary change in optical transmittance is noticeable immediately upon applying the OCA (minute-0). A sudden significant increase then occurs after 10 minutes ($p < 0.02342$ in 450-900 nm) which then gradually decreases. The curved black lines on the 3D figure depict transparency increases by 3.5%. A maximum optical transmittance of 90% (41% increase

above baseline values) was obtained after 11 minutes from applying OCA for the wavelength of 889 nm. The upper 2D map in the figure also reflects the spectrotemporal behavior of OCS, showing the ideal time to optically access the brain across the OCS. As an example, the dashed line represents the temporal change at a wavelength of 810 nm (the wavelength used for *in vivo* LSI). A time-window of ~13 minutes for using the OCS was evaluated, in which the OCS transparency (at 810 nm) is ~36% higher than the untreated scalp tissue ($p < 0.05$) (Figure 6.3(b)). The top 3% of optical transmittance improvement was achieved within minutes 5 to 18 after applying OCA, associated with an absolute change from 33% up to 36%. Figure 6.3(c) shows the temporal change in optical properties of the scalp tissue from the moment OCA was applied (minute-0) up to 40 minutes after application. A higher light transmission and transparency is noticeable at minute-10 which gradually decreases with time.

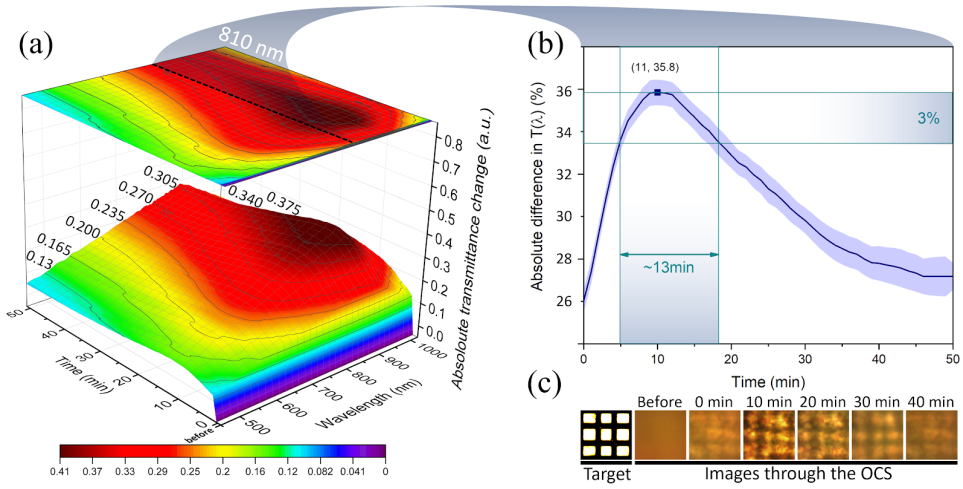

Figure 6.3. Temporal effect of OCA on scalp. a) Spectrotemporal behavior of OCS, absolute change in optical transmittance is shown versus wavelength and time. b)

Temporal change in optical transmittance at a wavelength of 810 nm (mean and SE values). A time-window of 13 minutes is augmented to the plot showing the duration of time transmittance is highest in the OCS. c) Visual comparison of photographs of a resolution target captured through scalp tissue before, immediately after (minute-0), and up to 40 minutes after applying OCA. The distance between the lines in the target is ~150 μm.

A set of photographs of an NBS 1963A resolution target imaged through the implant, skull, and scalp provides a visual comparison of the light transmittance and image quality over the samples (Figure 6.4(a)). Optical transmittance of skin, skull, and implant are shown in Figure 6.4(b). All three of the scalp, skull, and implant show an increasing trend in transmittance as the wavelength increases. The implant has higher optical transmittance compared to the skull in the range of 450-890 nm (significantly higher in 450-815 nm, $p < 0.05$). In the range of 525 - 600 nm, skull shows a drop in the transmittance which was not observed in the implant spectra. The same change in the slope at 525 - 600 nm, appeared in the scalp tissue as well. A comparison between the mouse scalp and skull optical transmittance shows that optical extinction by the scalp is notably higher than that of the skull ($p < 0.05$ in 450-900 nm), revealing that the scalp is the primary limiting factor here. The optimum effect of OCA was considered for the comparisons in Figure 6.4(c-f)). Figure 6.4(c) shows a significant relative increase of 100% (gray dashed line) in optical transmittance at 450 nm in OCS ($p = 0.0209$) which gradually decreased to 41% at 889 nm ($p = 0.0061$). Optical transmittance of the scalp+skull stack is shown in Figure 6.4(d) (dark green line). As expected, it resulted in a similar optical transmittance to the scalp (limited by the high optical extinction in the

scalp). OCS+skull optical transmittance showed a relative increased (gray line) of 61% (at 450 nm) and 46% (at 889 nm). The scalp+implant stack also has a similar optical behavior to the scalp alone (Figure 6.4(e)). A significant relative increase of 270% at 450 nm ($p = 0.02547$) was obtained by OCS+implant. Maximum optical transmittance of 89% was obtained at 889 nm which is 77% relatively higher compared to scalp+implant ($p = 0.0003$). Figure 6.4(f) compares light transmission through OCS+implant and scalp+skull. The bars show the maximum optical transmission of OCS+implant in various wavelength ranges including 89% in NIR range (700-900 nm), 50% in red range (565-700 nm), 24% in green range (485-565 nm), and 20% in blue range (450-485 nm). A maximum relative change of 151% (at 450 nm) in the optical transmittance was obtained using OCS+implant compared to scalp+skull ($p = 0.0043$).

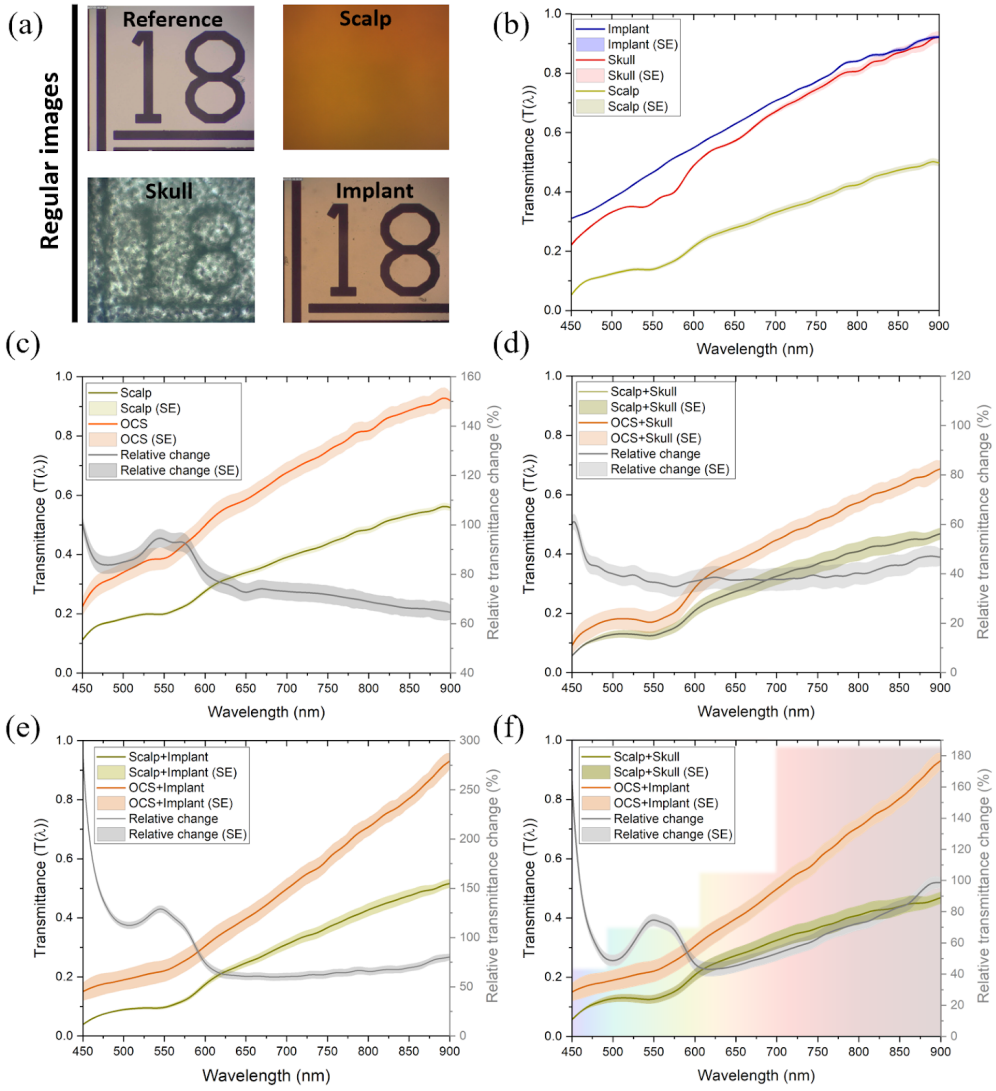

Figure 6.4. a) Visual comparison of light transmission using photographs of an NBS 1963A resolution target through the WttB implant, skull, and scalp. The resolutions shown are the 18 cycle/mm target (each black line width is 27.78 μm). b) Optical transmittance of scalp, skull, and implant. c) Comparison of optical transmittance through scalp and OCS. d-f) Comparison of the effect of optical clearing on optical transmittance of the tissue sample stacks; d) scalp+skull vs. OCS+skull, e) scalp+implant vs. OCS+implant, f) scalp+skull vs. OCS+implant.

In vivo LSI Imaging of Microvasculature

The results from *in vivo* LSI imaging are shown in Figure 6.5, 6.6, and 6.7. Figure 6.5(a) shows regular images (showing the LSI field of view) and LSI contrast images at each imaging condition for Mouse 10 (data for Mice 11-12 not shown). Line intensity profiles were analyzed for the intact scalp (i.e. condition 1), intact skull (i.e. condition 2), direct-brain (i.e. condition 3), implant (i.e. condition 4), scalp+implant (i.e. condition 5), and OCS+implant (i.e. condition 6) contrast images. To avoid selection bias, the location of these line profiles were chosen arbitrarily at the ROI mid-points, as depicted in the LSI images in Figure 6.5(a). The midlines intersected 3 to 4 vessels like the example shown with arrows in Figure 6.5(b) for Mouse 10. From these intensity profiles, peak intensity and noise (ΔK and σK_n) values were determined (as described in the Methods section and illustrated in the inset of Figure 6.5(b)). Then SNR and fall distance were calculated (see Figure 6.5(b) for an example trace with the 10–90% fall distance measurement illustrated). The scalp and scalp+implant did not visualize any vessels which could be considered for comparing SNR, sensitivity, and fall distance.

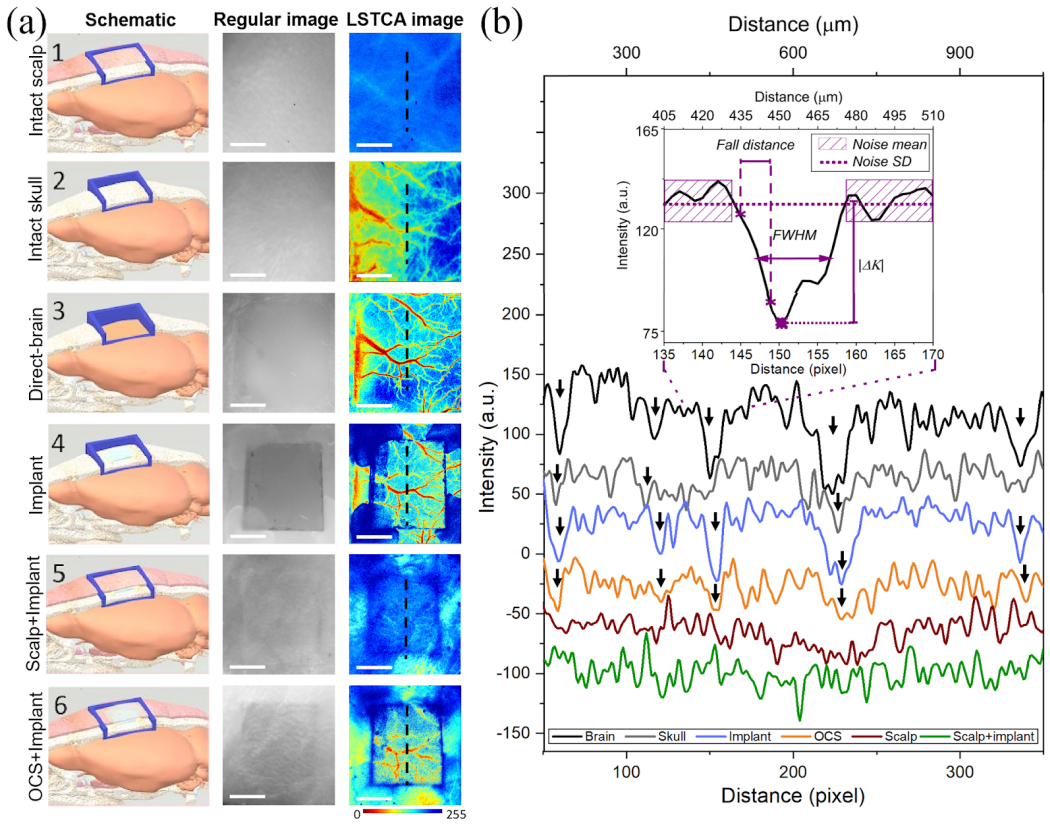

Figure 6.5. *In vivo* brain microcirculation images over the imaging conditions. a) The left column presents the schematics of the imaging conditions 1-6, with the blue tetragonals representing the imaging fields of view on murine cranium. The middle column shows regular images of the ROI which remain the same over the imaging conditions. The corresponding LSI temporal contrast images for 6 imaging conditions of Mouse 10 were shown in the right column. The dashed lines show the consistent location along the midline of ROI where line profiles were taken. b) Example contrast intensity profiles in imaging conditions of 1-6. The arrows in b) show the vessels that are intersected by the midline intensity profiles. Scale bars = 1 mm.

Data for each imaging condition was averaged between the vessels and the mean SNR for each imaging condition is shown in Figure 6.6(a). As shown in the Figure, the direct-brain gave the highest SNR, and implant, intact skull, and OCS+implant have lower SNR values respectively; while the intact scalp and scalp+implant did not show detectable vessels. Figure 6.6(b) shows a plot of vessels intersected by the profile line across the imaging conditions, with SNR plotted against FWHM (i.e. vessel diameter). Next, using the 15 LSI temporal contrast images corresponding to these imaging conditions for Mice 10-12, we sought to compare the sharpness (i.e. fall distance) of the vessels in the images to compare the image resolution. Values for each imaging condition were averaged between the vessels and the mean fall distance for each imaging condition is shown in Figure 6.6(c). Direct brain provided the lowest fall distance (highest sharpness) and intact skull resulted in the highest fall distance (lowest sharpness). OCS+implant showed slightly higher fall distance than implant alone ($p = 0.6721$). A plot of all vessels intersected by the profile line, with fall distance (i.e. vessel sharpness) plotted against FWHM (i.e. vessel diameter) is shown in Figure 6.6(d).

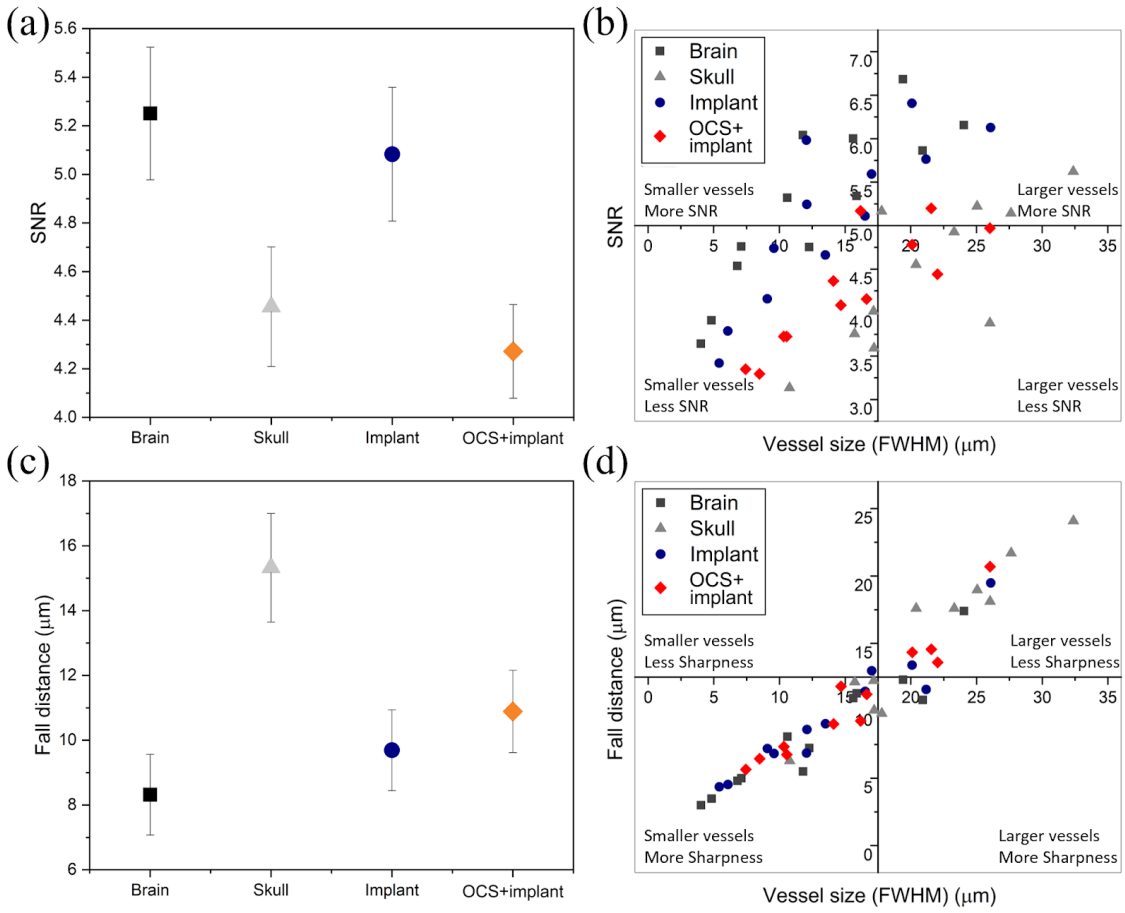

Figure 6.6. Comparison of LSI image quality over the imaging conditions. a) Mean SNR of contrast intensity along midline profiles on the imaging conditions. b) SNR vs FWHM for all vessels intersected by line profiles. c) Mean fall distance along the line profiles over the imaging conditions. d) Fall Distance vs FWHM for all vessels intersected. Error bars represent standard error.

Considering the temporal effect of OCA on scalp tissue optical transparency, we sought to quantitatively evaluate this effect on the LSI imaging quality. Figure 6.7(a) shows LSI images of OCS+implant (imaging condition 6) immediately after and up to 40 minutes after applying the OCA for Mouse 10 (data for Mice 11-12 not shown). The LSI images visually show the temporal change in scalp transparency. Line intensity profiles like the example shown in Figure 6.5(a) and 6.5(b) were analyzed to determine peak intensity and noise to calculate SNR and fall distance. Data for each time point (minutes 0, 10, 20, 30, and 40) was averaged between the vessels and the mean SNR for each time point after applying OCA (imaging condition 6) is shown in Figure 6.7(b). The minute-10 contrast image shows the highest SNR ($p < 0.05$) (imaging condition 6) which then gradually decreases at minutes 20 and 30 and approximately equals to the initial value (minute-0) at minute-40. Figure 6.7(c) shows a plot of vessels intersected by the profile line across the imaging conditions, with SNR plotted against FWHM (i.e. vessel diameter). Alongside, using the 15 LSI images corresponding to these time points for Mice 10-12, we compared the sharpness (i.e. fall distance) of the vessels in the images to compare the image resolution. Fall distances for each imaging time point were averaged between the vessels and the mean fall distance is shown in Figure 6.7(d). A plot of all vessels intersected by the profile line, with fall distance (i.e. vessel sharpness) plotted against FWHM (i.e. vessel diameter) is shown in Figure 6.7(e).

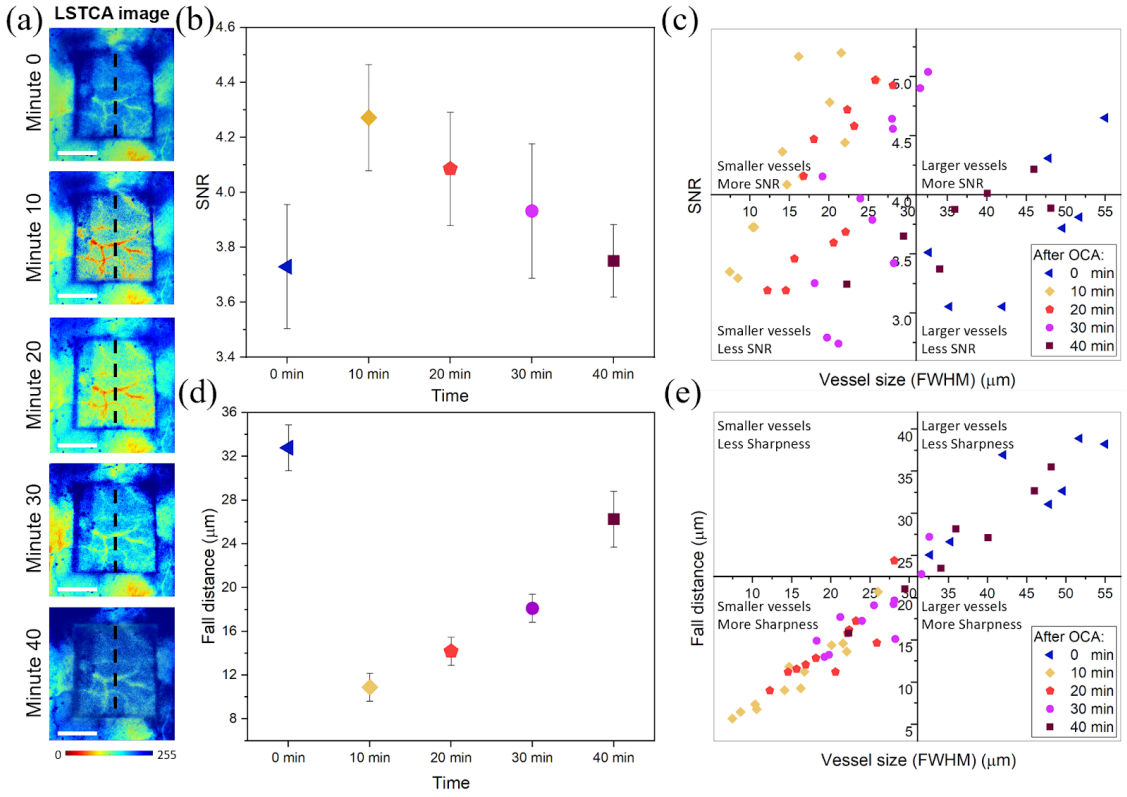

Figure 6.7. a) *In vivo* brain microcirculation LSI images of OCS+implant (imaging condition 6) immediately after and up to 40 minutes after applying the OCA. LSI images show the arbitrary locations where line profiles along the midline of ROI were taken. Scale bars = 1 mm. b-e) Comparison of LSI image quality of OCS+implant (imaging condition 6). Mean SNR of contrast intensity along line profiles on LSI images (Imaging condition 6) immediately after and up to 40 minutes after applying the OCA (b). SNR vs FWHM for all vessels intersected by line profiles (c). Mean fall distance along the line profiles over the time points (d). Fall Distance vs FWHM for all vessels intersected. Error bars represent standard error (e).

Discussion

The application of transparent cranial implants coupled with scalp optical clearing holds the transformative potential for facilitating the diagnosis and treatment of a wide variety of brain pathologies and neurological disorders. PEG, reported as a biocompatible OCA, has been widely used in various applications such as dermal blood flow imaging [124,149,154,155]. Although the effect of this OCA diminishes 10-20 minutes after the application, the optical access can be obtained repeatedly and chronically [124,155]. In this pilot study, we assessed the light delivery improvement by WttB implant coupled with OCS in a set of *ex vivo* optical characterization measurements. Additionally, we evaluated the feasibility of through-scalp brain microcirculation imaging *in vivo*. There are several limitations to the current study. The sample sizes used were small (n = 3), and further experiments are needed to confirm the reproducibility of these findings. While our proposed approach can allow for noninvasive imaging of the brain at later time points, it requires an initial implantation surgery which carries associated risks such as infection.

Ex vivo proof of concept: optical transmittance measurements

The scalp optical clearing results, shown in Figure 6.3 and Figure 6.4(c), were in agreement with the previous reports of using PG-PEG agent [142–144]. More effective OCAs have been introduced recently and although they have shown higher transparency, they have not been widely accessible and used [148]. The optimum effect resulted within 10-20 minutes after OCA application. The maximum optical transmission was obtained at minute-11 and wavelength of 889 nm. OCA provided 13 minutes of transparency in the

highest zone (33% - 36% increase in transparency) for wavelengths in the range of 800-900 nm. Since our optical measurements are based on collimated light transmittance we can not directly compare our results to the previous works. Therefore, our results were used to relatively compare optical transmittance values in the difference conditions. In Figure 6.4(a), the implant appears as a shade of orange indicating its higher light transmission in longer wavelengths. This nc-YSZ implant can be also optimized for various wavelength ranges [74]. The skull tissue transmits the light, although the texture of the cranial bone notably decreases the spatial resolution. The pristine scalp tissue has a very low light transmission and does not visualize the resolution target. It should also be noted that while the optical transmittance of the implant is an improvement over the skull, shown in Figure 6.4(a) and 6.4(b), the mouse skull is inherently transparent itself [114], which is not the case in larger animals or humans. The hemoglobin optical absorbance signature (520-620 nm) in scalp and skull tissues limiting the access in that wavelength range [54,156,157] is significantly improved through OCS+implant. In Figure 6.4(f), relative increase in transmittance (gray line) of up to 151% in blue (450-485 nm), 75% in green (485-565 nm), 55% in red (565-700 nm), and 99% in NIR (700-900 nm) wavelength ranges obtained through OCS+implant compared to scalp+skull. This shows promising features to facilitate various photosensitizer activation-based therapies. Photobiomodulation (600-1064 nm) [1,2,57–59], PDT(405-900 nm, mainly in red range) [4,60], optogenetic (400-630 nm) [5,9,61] are a few examples of optical techniques that could benefit from the improved light delivery offered by WttB implant and scalp optical clearing.

In vivo LSI Imaging of Microvasculature

It should be mentioned that blood flow is expected to be altered in response to the invasive cranioplasty surgery (e.g. due to potential reactive hyperemia [133], changes in respiration, and anesthesia depth).

The direct-brain image had the highest average SNR of 5.25. As the size of vessels and velocity of blood flow is not expected to differ on average between the imaging conditions, the apparent increase in SNR and vessel diameter imaged through the scalp, skull, implant, and OCS+implant is likely due to the blurring of the image. OCS+implant showed SNR of 4.25 and Sensitivity of 81% while intact scalp images did not show any detectable vessels. Implant and intact skull images had SNR values of 5.08 and 4.45, respectively ($p = 0.0047$). Imaging sensitivities for implant and intact skull were, respectively, 96% and 84%. In Figure 6.6(a), implant image vessels showed a similar pattern to the direct-brain vessels although they are slightly shifted toward lower SNR and higher size.

The OCS+implant showed fall distance of 11μm (see Figure 6.6(c)) while intact scalp did not visualize any brain vessels. The implant images had a lower fall distance of 9.6 μm (sharper image) compared to intact skull image with fall distance of 15.3 μm ($P < 0.001$). The skull and OCS scattering both disorder the speckle pattern that was created by the brain hemodynamics. The reduction in border sharpness of the vessels imaged through the intact skull vs OCS+implant suggests that the skull has a higher blurring effect as seen in Figure 6.5(a) and Figure 6.6(c). The direct-brain images with fall

distance of 8.2 μm showed the highest vessel sharpness ($p < 0.05$). In Figure 6.6(d), the data from OCS+implant, implant, and direct-brain fell into a similar cluster placed mostly in the lower left quadrant associated with lower vessel size and higher sharpness. On the other hand, a half of intact skull vessels were detected in the high vessel size and low sharpness quadrant.

In Figure 6.7(b), the change in SNR values from minute-0 to minutes-40 is in agreement with *ex vivo* optical transmittance measurements (Figure 6.3(b,c)) and also previous studies on LSI and OCAs [124,158]. In Figure 6.7(c), the vessels at minutes 10, 20, and 30 fell in the smaller vessel size quadrants (left half) covering both lower and higher SNR quadrants. On the other hand, the vessel at minutes 0 and 40 mostly fell in the lower SNR quadrants (lower half) including the smaller and larger vessel size quadrants. This suggests that within the time points with higher effect of OCA (minutes 10, 20, 30), the effect on detected vessel size is more obvious than the effect on the SNR value. In Figure 8(d), a significant increased sharpness is visible in minute-10 ($p < 0.05$). Additionally, the separated clusters of imaged vessels at minutes 10 and 20 in Figure 6.7(e) fell in the lower size and higher sharpness suggests that the OCA effect is more noticeable in sharpness (resolution) of the image than SNR.

Microcirculation plays a critical role in physiological processes such as tissue oxygenation and nutritional exchange [11,159]. Monitoring the spatiotemporal characteristics of microcirculation is crucial for studying the normal and pathophysiologic conditions of tissue metabolism. For example, microcirculation monitoring is useful for assessing

microcirculatory dysfunction due to disease conditions such as type 2 diabetes, peripheral vascular disease (PVD), atherosclerotic coronary artery disease, obesity, heart failure, Alzheimer's, schizophrenia and hypertension, among others [139,160,161]. In addition, quantification of dynamic blood flow, angiogenesis, and vessel density are critical for monitoring the progression of wound healing [140]. Although high-resolution vascular network mapping is possible using imaging modalities such as computed tomography (CT), these approaches require injection of contrast agents and pose disadvantages such as radiation exposure. Existing non-invasive methodologies (including LSI through skull) are inadequate to study brain blood flow at microvessel resolution [122]. To the best of our knowledge there have been no report of through-scalp brain microcirculation optical imaging. Optical accesses such as OCS coupled with WttB implant are thus important tools for research and can become important enablers of clinical diagnostics and therapy involving cerebral microvessels. Figure 6.8 visually illustrates the enhancement in optically accessing the brain microcirculation through OCS+implant. An example region in the flowmetric image shown with dashed line was compared to direct-brain and intact scalp images. The vessel intersected by the black line (V1) has a width of 22.5 μm and the vessel intersected by the purple line (V2) has a width of 16.8 μm. Precise velocity information, particularly of microvessels, appeared through the OCS+implant, while the inhibited signal through intact scalp and skull obscures flow determinations.

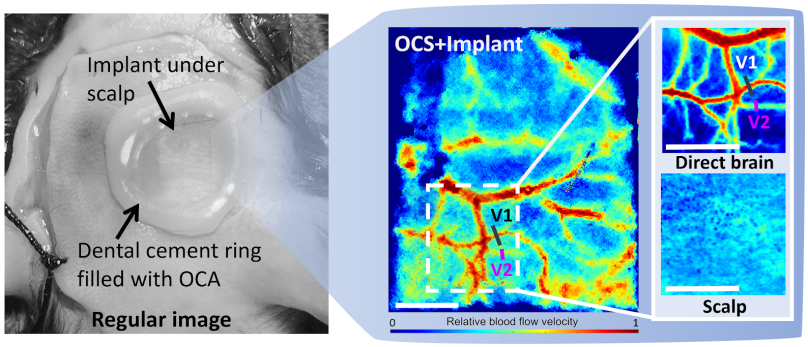

Figure 6.8. A regular image of Mouse 10 head showing the provided brain flowmetric imaged obtain through scalp. The implanted WttB prosthesis and a drop of OCA on the closed scalp was able to provide access to the brain microcirculation. An example region in the flowmetric image (shown with dashed line) was compared to the reference (direct-brain) and intact scalp images. The vessel intersected by the black line (V1) has a width of 22.5 µm and the vessel intersected by the purple line (V2) has a width of 16.8 µm. Scale bar = 500 µm.

Creating novel windows for brain studies has been gaining attention recently [35,162–164]. Some of these studies, involving OCAs applied to the scalp overlying native skull, have shown limited success due to optical losses and scattering in the skull [32]. Future studies by our group will explore this combined OCA-WttB strategy for chronic imaging in awake and behaving animals through closed scalp, to study cerebrovascular hemodynamic responses to a photoactivation stimulation.

In this study, a through-scalp optical access to the brain in wavelength range of blue to NIR (450-900nm) was reported. Application of a transparent cranial implant and optical clearing of the scalp shows promising features to facilitate various photosensitizer activation-based therapies. Additionally, transmittance peaked at 89% at 810 nm allowed for laser speckle imaging of brain microcirculation. Strategies for providing

through-scalp optical access to the brain without repeated craniectomy and/or scalp retraction, like the one presented in this chapter, could one day improve clinical imaging and optical diagnosis and treatment of brain diseases without the need for repeated craniectomy or retraction of the scalp .

Acknowledgments

I would like to acknowledge the contribution of my co-authors to this work: , Mildred S Cano-velázquez, Carrie R Jonak, David L Halaney, Devin K Binder, Juan A Hernándezcordero, and Guillermo Aguilar. This study was supported by National Science Foundation (NSF-PIRE, 1545852 & NSF-EAGER, 1547014), “Beca Mixta” from National Council of Science and Technology of Mexico (CONACYT) (741249), and DGAPA-PAPIIT (Grant IG100519). Also, the authors would like to acknowledge Gottlieb Uahengo for fabricating the YSZ samples.

Chapter 7. Conclusions and Recommendations for Future work

In this dissertation, I illustrated that transparency of WttB implant provides an excellent opportunity for light-based theranostics since light could be easily transmitted through it without undergoing excessive attenuation. In addition, transmission of visible and near infrared light through transparent cranial implants would not only open a "window" through which detailed brain features could be imaged and deep targets could be therapeutically treated, but would also facilitate through-scalp prolonged post-operatory interventions.

The feasibility of long term application of nc-YSZ implants with various dopant levels was demonstrated in this dissertation. In chapter 2, I showed WttB implant can withstand extended accelerated ageing tests and preserve its excellent optical and mechanical properties. Then, this implant was applied for chronic brain imaging on mice. In chapter 3, image quality stability up to 60 days post-implantation was shown. Since WttB implant allows light transmission for a wide range of wavelengths, I developed and applied a multispectral imaging coupled with LSI. This study, demonstrated in chapter 4, showed arteriovenous imaging of brain microvessels through WttB implant is possible and visuals a unique vascule map which is not possible through intact skull. Since WttB cranial implant is developed to provide optical access for post-operative theranostic purposes without scalp removal, in Chapters 5 and 6 I illustrated the use of an optical clearing agent (OCA) in the scalp of mice to provide a through-scalp optical access to the brain. In vivo laser speckle imaging experiments of mouse cerebral blood vessels allowed

for through-scalp visualization of microvessels, which was not possible through the uncleared scalp and intact skull.

It will be beneficial to investigate the potential of nc-YSZ implant for facilitating non-invasive, LSI-based early detection of ischemic stroke as it is the 5th leading cause of death in the United States and the leading cause of serious long-term disability. LSI can be used to monitor the brain microcirculation through WttB implant to regionally identify ischemic cerebrovascular blood flow and determine stereotaxic locations for the ischemic core, penumbra, oligemia and peri-infarct normal tissue.

In conclusion, replacing repeated craniotomies with one-time placement of nc-YSZ implants will prevent expensive and highly invasive craniotomies. This would eventually facilitate clinical light-based therapeutic techniques such as photobiomodulation, photodynamic therapy, and optogenetics and noninvasively diagnosis of hematomas, and small pathologic structures with a high resolution.

References

1. Yun, S. H. & Kwok, S. J. J. Light in diagnosis, therapy and surgery. *Nat Biomed Eng* **1**, (2017).

2. Chung, H. *et al.* The nuts and bolts of low-level laser (light) therapy. *Ann. Biomed. Eng.* **40**, 516–533 (2012).

3. Naeser, M. A. *et al.* Significant improvements in cognitive performance post-transcranial, red/near-infrared light-emitting diode treatments in chronic, mild traumatic brain injury: open-protocol study. *J. Neurotrauma* **31**, 1008–1017 (2014).

4. Agostinis, P. *et al.* Photodynamic therapy of cancer: an update. *CA Cancer J. Clin.* **61**, 250–281 (2011).

5. Gradinaru, V., Mogri, M., Thompson, K. R., Henderson, J. M. & Deisseroth, K. Optical deconstruction of parkinsonian neural circuitry. *Science* **324**, 354–359 (2009).

6. Creed, M., Pascoli, V. J. & Lüscher, C. Addiction therapy. Refining deep brain stimulation to emulate optogenetic treatment of synaptic pathology. *Science* **347**, 659–664 (2015).

7. Ramirez, S. *et al.* Activating positive memory engrams suppresses depression-like behaviour. *Nature* **522**, 335–339 (2015).

8. Iyer, S. M. *et al.* Virally mediated optogenetic excitation and inhibition of pain in freely moving nontransgenic mice. *Nat. Biotechnol.* **32**, 274–278 (2014).

9. Bruegmann, T. *et al.* Optogenetic control of contractile function in skeletal muscle. *Nat. Commun.* **6**, 7153 (2015).

10. Gutruf, P. & Rogers, J. A. Implantable, wireless device platforms for neuroscience research. *Curr. Opin. Neurobiol.* **50**, 42–49 (2018).

11. Schwartz, W. J. *et al.* Metabolic mapping of functional activity in the hypothalamo-neurohypophysial system of the rat. *Science* **205**, 723–725 (1979).

12. Gusnard, D. A., Raichle, M. E. & Raichle, M. E. Searching for a baseline: functional imaging and the resting human brain. *Nat. Rev. Neurosci.* **2**, 685–694 (2001).

13. Towle, E. L., Richards, L. M., Kazmi, S. M. S., Fox, D. J. & Dunn, A. K. Comparison of indocyanine green angiography and laser speckle contrast imaging for the assessment of vasculature perfusion. *Neurosurgery* **71**, 1023–30; discussion 1030–1 (2012).

14. Scerrati, A. *et al.* Indocyanine green video-angiography in neurosurgery: a glance beyond vascular applications. *Clin. Neurol. Neurosurg.* **124**, 106–113 (2014).

15. Jonathan, E., Enfield, J. & Leahy, M. J. Correlation mapping method for generating

microcirculation morphology from optical coherence tomography (OCT) intensity images. *J. Biophotonics* **4**, 583–587 (2011).

16. Hu, S., Maslov, K., Tsytsarev, V. & Wang, L. V. Functional transcranial brain imaging by optical-resolution photoacoustic microscopy. *J. Biomed. Opt.* **14**, 040503 (2009).

17. Leahy, M. J. *Microcirculation Imaging*. (John Wiley & Sons, 2012).

18. Devor, A. *et al.* Frontiers in optical imaging of cerebral blood flow and metabolism. *J. Cereb. Blood Flow Metab.* **32**, 1259–1276 (2012).

19. Tsytsarev, V., Rao, B., Maslov, K. I., Li, L. & Wang, L. V. Photoacoustic and optical coherence tomography of epilepsy with high temporal and spatial resolution and dual optical contrasts. *J. Neurosci. Methods* **216**, 142–145 (2013).

20. Gottschalk, S., Fehm, T. F., Deán-Ben, X. L., Tsytsarev, V. & Razansky, D. Correlation between volumetric oxygenation responses and electrophysiology identifies deep thalamocortical activity during epileptic seizures. *Neurophotonics* **4**, 011007 (2017).

21. Zhang, Q. *et al.* Wide-field optical coherence tomography based microangiography for retinal imaging. *Sci. Rep.* **6**, 22017 (2016).

22. Klein, K. U. *et al.* Measurement of cortical microcirculation during intracranial aneurysm surgery by combined laser-Doppler flowmetry and photospectrometry. *Neurosurgery* **69**, 391–398 (2011).

23. Miao, P. *et al.* Chronic wide-field imaging of brain hemodynamics in behaving animals. *Biomed. Opt. Express* **8**, 436–445 (2017).

24. Davoodzadeh, N. *et al.* Evaluation of a transparent cranial implant as a permanent window for cerebral blood flow imaging. *Biomed. Opt. Express* **9**, 4879–4892 (2018).

25. Davoodzadeh, N. *et al.* Laser speckle imaging of brain blood flow through a transparent nanocrystalline yttria-stabilized-zirconia cranial implant. in *Dynamics and Fluctuations in Biomedical Photonics XV* vol. 10493 1049303 (International Society for Optics and Photonics, 2018).

26. Davoodzadeh, N. *et al.* Optical Access to Arteriovenous Cerebral Microcirculation Through a Transparent Cranial Implant. *Lasers Surg. Med.* (2019) doi:10.1002/lsm.23127.

27. Davoodzadeh, N. & Cano-Velázquez, M. S. Evaluation of a transparent cranial implant for multi-wavelength intrinsic optical signal imaging. *Neural Imaging and* (2019).

28. Sakadžić, S. *et al.* Simultaneous imaging of cerebral partial pressure of oxygen and blood flow during functional activation and cortical spreading depression. *Appl. Opt., AO* **48**, D169–D177 (2009).

29. Bouchard, M. B., Chen, B. R., Burgess, S. A. & Hillman, E. M. C. Ultra-fast multispectral optical imaging of cortical oxygenation, blood flow, and intracellular calcium dynamics.

Opt. Express **17**, 15670–15678 (2009).

30. Parthasarathy, A. B., Kazmi, S. M. S. & Dunn, A. K. Quantitative imaging of ischemic stroke through thinned skull in mice with Multi Exposure Speckle Imaging. *Biomed. Opt. Express* **1**, 246 (2010).

31. Wang, J., Zhang, Y., Xu, T. H., Luo, Q. M. & Zhu, D. An innovative transparent cranial window based on skull optical clearing. *Laser Phys. Lett.* **9**, 469 (2012).

32. Zhang, C. *et al.* A large, switchable optical clearing skull window for cerebrovascular imaging. *Theranostics* **8**, 2696–2708 (2018).

33. Zhao, Y.-J. *et al.* Skull optical clearing window for in vivo imaging of the mouse cortex at synaptic resolution. *Light Sci Appl* **7**, 17153 (2018).

34. Chen, B. R., Bouchard, M. B., McCaslin, A. F. H., Burgess, S. A. & Hillman, E. M. C. High-speed vascular dynamics of the hemodynamic response. *Neuroimage* **54**, 1021–1030 (2011).

35. Heo, C. *et al.* A soft, transparent, freely accessible cranial window for chronic imaging and electrophysiology. *Sci. Rep.* **6**, 27818 (2016).

36. Smith, S. S., Magnusen, P. & Pletka, B. J. Fracture toughness of glass using the indentation fracture technique. in *Fracture Mechanics for Ceramics, Rocks, and Concrete* (ASTM International, 1981).

37. Hulbert, S. F. THE USE OF ALUMINA AND ZIRCONIA IN SURGICAL IMPLANTS. in *An Introduction to Bioceramics* vol. 1 25–40 (WORLD SCIENTIFIC, 1993).

38. Davoodzadeh, N., Uahengo, G., Halaney, D., Garay, J. E. & Aguilar, G. Influence of low temperature ageing on optical and mechanical properties of transparent yittria stabilized-zirconia cranial prosthesis. in *Design and Quality for Biomedical Technologies XI* vol. 10486 104860A (International Society for Optics and Photonics, 2018).

39. Damestani, Y. *et al.* Transparent nanocrystalline yttria-stabilized-zirconia calvarium prosthesis. *Nanomedicine* **9**, 1135–1138 (2013).

40. Gutierrez, M. I. *et al.* Novel Cranial Implants of Yttria-Stabilized Zirconia as Acoustic Windows for Ultrasonic Brain Therapy. *Adv. Healthc. Mater.* **6**, (2017).

41. Cano-Velázquez, M. S. *et al.* Evaluation of Optical Access to the Brain in the Near Infrared Range with a Transparent Cranial Implant. in *Latin America Optics and Photonics Conference* Tu5C.2 (Optical Society of America, 2018).

42. Davoodzadeh, N., Cuando, N., Aminfar, A. H., Cano, M. & Aguilar, G. ASSESSMENT OF BACTERIA GROWTH UNDER TRANSPARENT NANOCRYSTALLINE YTTRIASTABILIZED-ZIRCONIA CRANIAL IMPLANT USING LASER SPECKLE IMAGING. in *LASERS IN SURGERY AND MEDICINE* vol. 50 S5–S6 (WILEY 111 RIVER

ST, HOBOKEN 07030-5774, NJ USA, 2018).

43. Davoodzadeh, N. *et al.* Characterization of ageing resistant transparent nanocrystalline yttria-stabilized zirconia implants. *J. Biomed. Mater. Res. B Appl. Biomater.* (2019) doi:10.1002/jbm.b.34425.

44. Cano-Velázquez, M. S. *et al.* Enhanced near infrared optical access to the brain with a transparent cranial implant and scalp optical clearing. *Biomed. Opt. Express, BOE* **10**, 3369–3379 (2019).

45. Halaney, D. L. & Jonak, C. OPTICAL COHERENCE TOMOGRAPHY AND LASER SPECKLE IMAGING OF THE BRAIN THROUGH A TRANSPARENT CRANIAL IMPLANT IN A …. *LASERS IN* (2018).

46. Davoodzadeh, N. LOW-TEMPERATURE AGEING OF TRANSPARENT NANOCRYSTALLINE YTTRIA-STABILIZED-ZIRCONIA CALVARIUM PROTHESIS. *Lasers Surg. Med.* (2017).

47. Sordillo, L. A., Pu, Y., Pratavieira, S., Budansky, Y. & Alfano, R. R. Deep optical imaging of tissue using the second and third near-infrared spectral windows. *J. Biomed. Opt.* **19**, 056004 (2014).

48. Hong, G., Antaris, A. L. & Dai, H. Near-infrared fluorophores for biomedical imaging. *Nature Biomedical Engineering* **1**, 0010 (2017).

49. Bashkatov, A. N. *et al.* Measurement of tissue optical properties in the context of tissue optical clearing. *J. Biomed. Opt.* **23**, 1–31 (2018).

50. Golovynskyi, S. *et al.* Optical windows for head tissues in near-infrared and short-wave infrared regions: Approaching transcranial light applications. *Journal of Biophotonics* vol. 11 e201800141 (2018).

51. Madsen, S. J. *Optical Methods and Instrumentation in Brain Imaging and Therapy*. (Springer Science & Business Media, 2012).

52. Hong, G. *et al.* Through-skull fluorescence imaging of the brain in a new near-infrared window. *Nat. Photonics* **8**, 723–730 (2014).

53. Shi, L., Sordillo, L. A., Rodríguez-Contreras, A. & Alfano, R. Transmission in near-infrared optical windows for deep brain imaging. *J. Biophotonics* **9**, 38–43 (2016).

54. Jacques, S. L. Optical properties of biological tissues: a review. *Phys. Med. Biol.* **58**, R37–61 (2013).

55. Curcio, J. A. & Petty, C. C. The Near Infrared Absorption Spectrum of Liquid Water. *J. Opt. Soc. Am., JOSA* **41**, 302–304 (1951).

56. Tsai, C.-L., Chen, J.-C., Wang, W.-J. & Others. Near-infrared absorption property of biological soft tissue constituents. *J. Med. Biol. Eng.* **21**, 7–14 (2001).

57. Salehpour, F. *et al.* Near-infrared photobiomodulation combined with coenzyme Q10 for depression in a mouse model of restraint stress: reduction in oxidative stress, neuroinflammation, and apoptosis. *Brain Research Bulletin* vol. 144 213–222 (2019).

58. Caldieraro, M. A. & Cassano, P. Transcranial and systemic photobiomodulation for major depressive disorder: A systematic review of efficacy, tolerability and biological mechanisms. *J. Affect. Disord.* **243**, 262–273 (2019).

59. Hamblin, M. R. Photobiomodulation for traumatic brain injury and stroke. *J. Neurosci. Res.* **96**, 731–743 (2018).

60. Quirk, B. J. *et al.* Photodynamic therapy (PDT) for malignant brain tumors--where do we stand? *Photodiagnosis Photodyn. Ther.* **12**, 530–544 (2015).

61. Dufour, S. & De Koninck, Y. Optrodes for combined optogenetics and electrophysiology in live animals. *Neurophotonics* **2**, 031205 (2015).

62. Nakamura, K., Kanno, T., Milleding, P. & Ortengren, U. Zirconia as a dental implant abutment material: a systematic review. *Int. J. Prosthodont.* **23**, 299–309 (2010).

63. Casolco, S. R., Xu, J. & Garay, J. E. Transparent/translucent polycrystalline nanostructured yttria stabilized zirconia with varying colors. *Scr. Mater.* **58**, 516–519 (2008).

64. Xiong, Y., Fu, Z., Pouchly, V., Maca, K. & Shen, Z. Preparation of Transparent 3 Y-TZP Nanoceramics with No Low-Temperature Degradation. *J. Am. Ceram. Soc.* **97**, 1402–1406 (2014).

65. Rosenflanz, A. *et al.* Bulk glasses and ultrahard nanoceramics based on alumina and rare-earth oxides. *Nature* **430**, 761–764 (2004).

66. Anselmi-Tamburini, U., Woolman, J. N. & Munir, Z. A. Transparent Nanometric Cubic and Tetragonal Zirconia Obtained by High-Pressure Pulsed Electric Current Sintering. *Advanced Functional Materials* vol. 17 3267–3273 (2007).

67. Grasso, S., Kim, B.-N., Hu, C., Maizza, G. & Sakka, Y. Highly Transparent Pure Alumina Fabricated by High-Pressure Spark Plasma Sintering. *Journal of the American Ceramic Society* vol. 93 2460–2462 (2010).

68. Cano-Velázquez, M. S. *et al.* Evaluation of Optical Access to the Brain in the Near Infrared Range with a Transparent Cranial Implant. in *Latin America Optics and Photonics Conference* Tu5C.2 (Optical Society of America, 2018).

69. Davoodzadeh, N., Cuando, N., Aminfar, A. H., Cano, M. & Aguilar, G. ASSESSMENT OF BACTERIA GROWTH UNDER TRANSPARENT NANOCRYSTALLINE YTTRIASTABILIZED-ZIRCONIA CRANIAL IMPLANT USING LASER SPECKLE IMAGING. in *LASERS IN SURGERY AND MEDICINE* vol. 50 S5–S6 (WILEY 111 RIVER ST, HOBOKEN 07030-5774, NJ USA, 2018).

70. Davoodzadeh, N., Halaney, D. & Jonak, C. R. Laser speckle imaging of brain blood flow through a transparent nanocrystalline yttria-stabilized-zirconia cranial implant. *and Fluctuations in …* (2018).

71. Aminfar, A., Davoodzadeh, N., Aguilar, G. & Princevac, M. Application of optical flow algorithms to laser speckle imaging. *Microvasc. Res.* **122**, 52–59 (2019).

72. Davoodzadeh, N. *et al.* Evaluation of a transparent cranial implant for multi-wavelength intrinsic optical signal imaging. in *Neural Imaging and Sensing 2019* vol. 10865 108650B (International Society for Optics and Photonics, 2019).

73. Halaney, D. L. *et al.* OPTICAL COHERENCE TOMOGRAPHY AND LASER SPECKLE IMAGING OF THE BRAIN THROUGH A TRANSPARENT CRANIAL IMPLANT IN A CHRONIC MOUSE MODEL. in *LASERS IN SURGERY AND MEDICINE* vol. 50 S10–S10 (WILEY 111 RIVER ST, HOBOKEN 07030-5774, NJ USA, 2018).

74. Alaniz, J. E., Perez-Gutierrez, F. G., Aguilar, G. & Garay, J. E. Optical properties of transparent nanocrystalline yttria stabilized zirconia. *Optical Materials* vol. 32 62–68 (2009).

75. Chevalier, J., Cales, B. & Drouin, J. M. Low-temperature aging of Y-TZP ceramics. *J. Am. Ceram. Soc.* **82**, 2150–2154 (1999).

76. Lughi, V. & Sergo, V. Low temperature degradation-aging-of zirconia: A critical review of the relevant aspects in dentistry. *Dent. Mater.* (2010).

77. Chevalier, J., Gremillard, L. & Deville, S. Low-Temperature Degradation of Zirconia and Implications for Biomedical Implants. *Annu. Rev. Mater. Res.* **37**, 1–32 (2007).

78. Muñoz-Saldaña, J. & Balmori-Ramírez, H. Mechanical properties and low-temperature aging of tetragonal zirconia polycrystals processed by hot isostatic pressing. *Proc. Inst. Mech. Eng. Part L J. Mat. Des. Appl.* (2003).

79. Deville, S., Chevalier, J. & Gremillard, L. Influence of surface finish and residual stresses on the ageing sensitivity of biomedical grade zirconia. *Biomaterials* **27**, 2186–2192 (2006).

80. Garay, J. E. Current-Activated, Pressure-Assisted Densification of Materials. *Annual Review of Materials Research* vol. 40 445–468 (2010).

81. for Testing, A. S., on Metal Powders, M. C. B. & Products, M. P. *Standard Test Methods for Density of Compacted or Sintered Powder Metallurgy (PM) Products Using Archimedes' Principle*. (ASTM International, 2009).

82. Keefer, K. D. & Michalske, T. A. Determination of Phase Transformation Depth Profiles with Synchrotron Radiation. *J. Am. Ceram. Soc.* **70**, 227–231 (1987).

83. Chevalier, J. What future for zirconia as a biomaterial? *Biomaterials* **27**, 535–543 (2006).

84. Kim, D.-J., Jang, J.-W. & Lee, H.-L. Effect of tetravalent dopants on Raman spectra of tetragonal zirconia. *J. Am. Ceram. Soc.* **80**, 1453–1461 (1997).

85. Damestani, Y., Galan-Hoffman, D. E., Ortiz, D., Cabrales, P. & Aguilar, G. Inflammatory response to implantation of transparent nanocrystalline yttria-stabilized zirconia using a dorsal window chamber model. *Nanomedicine* **12**, 1757–1763 (2016).

86. Aguilar, G., Davoodzadeh, N., Halaney, D., Uahengo, G. & Garay, J. E. Influence of low temperature ageing on optical and mechanical properties of transparent yittria stabilized-zirconia cranial prosthesis. *Design and Quality for Biomedical Technologies XI* (2018) doi:10.1117/12.2287296.

87. Davoodzadeh, N. LOW-TEMPERATURE AGEING OF TRANSPARENT NANOCRYSTALLINE YTTRIA-STABILIZED-ZIRCONIA CALVARIUM PROTHESIS. in *LASERS IN SURGERY AND MEDICINE* vol. 49 440–440 (WILEY 111 RIVER ST, HOBOKEN 07030-5774, NJ USA, 2017).

88. Xiong, Y., Fu, Z., Pouchly, V., Maca, K. & Shen, Z. Preparation of Transparent 3Y-TZP Nanoceramics with No Low-Temperature Degradation. *J. Am. Ceram. Soc.* **97**, 1402–1406 (2014).

89. Zhang, F. *et al.* Highly-translucent, strong and aging-resistant 3Y-TZP ceramics for dental restoration by grain boundary segregation. *Acta Biomater.* **16**, 215–222 (2015).

90. Wei, C. & Gremillard, L. Towards the prediction of hydrothermal ageing of 3Y-TZP bioceramics from processing parameters. *Acta Materialia* vol. 144 245–256 (2018).

91. Tredici, I. G. *et al.* Low temperature degradation resistant nanostructured yttria-stabilized zirconia for dental applications. *Ceram. Int.* **42**, 8190–8197 (2016).

92. Pitzer, K. S. Self-ionization of water at high temperature and the thermodynamic properties of the ions. *J. Phys. Chem.* **86**, 4704–4708 (1982).

93. Perrichon, A. *et al.* A testing protocol combining shocks, hydrothermal ageing and friction, applied to Zirconia Toughened Alumina (ZTA) hip implants. *J. Mech. Behav. Biomed. Mater.* **65**, 600–608 (2017).

94. ISO 13356:2008 - Implants for surgery -- Ceramic materials based on yttria-stabilized tetragonal zirconia (Y-TZP). https://www.iso.org/standard/40166.html.

95. Sanon, C., Chevalier, J., Douillard, T. & Cattani-Lorente, M. A new testing protocol for zirconia dental implants. *Dent. Mater.* (2015).

96. Lucas, T. J., Lawson, N. C., Janowski, G. M. & Burgess, J. O. Effect of grain size on the monoclinic transformation, hardness, roughness, and modulus of aged partially stabilized zirconia. *Dent. Mater.* **31**, 1487–1492 (2015).

97. Zhang, F. *et al.* Effect of cation dopant radius on the hydrothermal stability of tetragonal

zirconia: Grain boundary segregation and oxygen vacancy annihilation. *Acta Mater.* **106**, 48–58 (2016).

98. Kodera, Y., Hardin, C. L. & Garay, J. E. Transmitting, emitting and controlling light: Processing of transparent ceramics using current-activated pressure-assisted densification. *Scr. Mater.* **69**, 149–154 (2013).

99. Luo, J. & Stevens, R. Porosity-dependence of elastic moduli and hardness of 3Y-TZP ceramics. *Ceram. Int.* (1999).

100. Asakura, T. & Takai, N. Dynamic laser speckles and their application to velocity measurements of the diffuse object. *J. Phys. D Appl. Phys.* **25**, 179–194 (1981).

101. Fujii, H., Nohira, K., Yamamoto, Y., Ikawa, H. & Ohura, T. Evaluation of blood flow by laser speckle image sensing. Part 1. *Appl. Opt.* **26**, 5321–5325 (1987).

102. Halkon, B. J. & Rothberg, S. J. Synchronized-scanning laser vibrometry. *Sixth International Conference on Vibration Measurements by Laser Techniques: Advances and Applications* (2004) doi:10.1117/12.579759.

103. Fujii, H., Asakura, T. & Shindo, Y. Measurement of surface roughness properties by using image speckle contrast. *J. Opt. Soc. Am., JOSA* **66**, 1217–1222 (1976).

104. Tang, M.-X., Elson, D. S., Li, R., Dunsby, C. & Eckersley, R. J. Photoacoustics, thermoacoustics, and acousto-optics for biomedical imaging. *Proc. Inst. Mech. Eng. H* **224**, 291–306 (2010).

105. Li, J., Ku, G. & Wang, L. V. Ultrasound-modulated optical tomography of biological tissue by use of contrast of laser speckles. *Appl. Opt.* **41**, 6030–6035 (2002).

106. Dunn, A. K., Bolay, H., Moskowitz, M. J. & Boas, D. A. Spatially resolved cerebral blood flow imaging using laser speckle. *Optical Diagnostics of Living Cells IV* (2001) doi:10.1117/12.426780.

107. Briers, J. D. & Webster, S. Laser speckle contrast analysis (LASCA): a nonscanning, full-field technique for monitoring capillary blood flow. *J. Biomed. Opt.* **1**, 174–179 (1996).

108. Cheng, H. *et al.* Modified laser speckle imaging method with improved spatial resolution. *J. Biomed. Opt.* **8**, 559–564 (2003).

109. Liu, Q., Wang, Z. & Luo, Q. Temporal clustering analysis of cerebral blood flow activation maps measured by laser speckle contrast imaging. *J. Biomed. Opt.* **10**, 024019 (2005).

110. Boas, D. A. & Dunn, A. K. Laser speckle contrast imaging in biomedical optics. *J. Biomed. Opt.* **15**, 011109 (2010).

111. Briers, J. D. Laser speckle contrast imaging for measuring blood flow. *Optica Applicata* **37**, (2007).

112. Konishi, N. & Fujii, H. Real-time visualization of retinal microcirculation by laser flowgraphy. *Organ. Ethic.* **34**, 753–758 (1995).

113. Aizu, Y., Ambar, H., Yamamoto, T. & Asakura, T. Measurements of flow velocity in a microscopic region using dynamic laser speckles based on the photon correlation. *Opt. Commun.* **72**, 269–273 (1989).

114. Li, P., Ni, S., Zhang, L., Zeng, S. & Luo, Q. Imaging cerebral blood flow through the intact rat skull with temporal laser speckle imaging. *Opt. Lett.* **31**, 1824–1826 (2006).

115. Parthasarathy, A. B., Shams Kazmi, S. M. & Dunn, A. K. Quantitative imaging of ischemic stroke through thinned skull in mice with Multi Exposure Speckle Imaging. *Biomedical Optics Express* vol. 1 246 (2010).

116. Shih, A. Y., Mateo, C., Drew, P. J., Tsai, P. S. & Kleinfeld, D. A polished and reinforced thinned-skull window for long-term imaging of the mouse brain. *J. Vis. Exp.* (2012) doi:10.3791/3742.

117. Roome, C. J. & Kuhn, B. Chronic cranial window with access port for repeated cellular manipulations, drug application, and electrophysiology. *Front. Cell. Neurosci.* **8**, 379 (2014).

118. Zuluaga-Ramirez, V., Rom, S. & Persidsky, Y. Craniula: A cranial window technique for prolonged imaging of brain surface vasculature with simultaneous adjacent intracerebral injection. *Fluids Barriers CNS* **12**, 24 (2015).

119. Yuan, S., Devor, A., Boas, D. A. & Dunn, A. K. Determination of optimal exposure time for imaging of blood flow changes with laser speckle contrast imaging. *Appl. Opt.* **44**, 1823–1830 (2005).

120. Roustit, M. & Cracowski, J.-L. Assessment of endothelial and neurovascular function in human skin microcirculation. *Trends Pharmacol. Sci.* **34**, 373–384 (2013).

121. Rizzoni, D. *et al.* How to assess microvascular structure in humans. *High Blood Press. Cardiovasc. Prev.* **18**, 169–177 (2011).

122. Eriksson, S., Nilsson, J. & Sturesson, C. Non-invasive imaging of microcirculation: a technology review. *Med. Devices* **7**, 445–452 (2014).

123. Zhao, L., Li, Y., Lu, H., Yuan, L. & Tong, S. Separation of cortical arteries and veins in optical neurovascular imaging. *J. Innov. Opt. Health Sci.* **07**, 1350069 (2014).

124. Shi, R., Chen, M., Tuchin, V. V. & Zhu, D. Accessing to arteriovenous blood flow dynamics response using combined laser speckle contrast imaging and skin optical clearing. *Biomed. Opt. Express* **6**, 1977–1989 (2015).

125. Ba, A. M. *et al.* Multiwavelength optical intrinsic signal imaging of cortical spreading depression. *J. Neurophysiol.* **88**, 2726–2735 (2002).

126. Dunn, A. K. *et al.* Simultaneous imaging of total cerebral hemoglobin concentration, oxygenation, and blood flow during functional activation. *Opt. Lett.* **28**, 28–30 (2003).

127. Jones, P. B. *et al.* Simultaneous multispectral reflectance imaging and laser speckle flowmetry of cerebral blood flow and oxygen metabolism in focal cerebral ischemia. *J. Biomed. Opt.* **13**, 044007 (2008).

128. Dunn, A. K., Devor, A., Dale, A. M. & Boas, D. A. Spatial extent of oxygen metabolism and hemodynamic changes during functional activation of the rat somatosensory cortex. *Neuroimage* **27**, 279–290 (2005).

129. Robles, F. E., Chowdhury, S. & Wax, A. Assessing hemoglobin concentration using spectroscopic optical coherence tomography for feasibility of tissue diagnostics. *Biomed. Opt. Express, BOE* **1**, 310–317 (2010).

130. Frangi, A. F., Niessen, W. J., Vincken, K. L. & Viergever, M. A. Multiscale vessel enhancement filtering. *Medical Image Computing and Computer-Assisted Intervention — MICCAI'98* 130–137 (1998) doi:10.1007/bfb0056195.

131. Fauver, M. *et al.* Three-dimensional imaging of single isolated cell nuclei using optical projection tomography. *Opt. Express* **13**, 4210–4223 (2005).

132. Hillman, L. W. & Denninghoff, K. R. Absorption Spectra of Hemoglobin with Intermediate Oxygenation. *Frontiers in Optics* (2005) doi:10.1364/fio.2005.ftuaa6.

133. Gourley, J. K. & Heistad, D. D. Characteristics of reactive hyperemia in the cerebral circulation. *Am. J. Physiol.* **246**, H52–8 (1984).

134. Dufour, S. *et al.* Evaluation of laser speckle contrast imaging as an intrinsic method to monitor blood brain barrier integrity. *Biomed. Opt. Express* **4**, 1856–1875 (2013).

135. Wang, Y., Hu, D., Liu, Y. & Li, M. Cerebral artery-vein separation using 0.1-Hz oscillation in dual-wavelength optical imaging. *IEEE Trans. Med. Imaging* **30**, 2030–2043 (2011).

136. Narasimha-Iyer, H., Beach, J. M., Khoobehi, B. & Roysam, B. Automatic identification of retinal arteries and veins from dual-wavelength images using structural and functional features. *IEEE Trans. Biomed. Eng.* **54**, 1427–1435 (2007).

137. Feng, N. *et al.* Simultaneous automatic arteries-veins separation and cerebral blood flow imaging with single-wavelength laser speckle imaging. *Opt. Express* **19**, 15777–15791 (2011).

138. Hu, D., Wang, Y., Liu, Y., Li, M. & Liu, F. Separation of arteries and veins in the cerebral cortex using physiological oscillations by optical imaging of intrinsic signal. *J. Biomed. Opt.* **15**, 036025 (2010).

139. Sokolnicki, L. A., Roberts, S. K., Wilkins, B. W., Basu, A. & Charkoudian, N. Contribution of nitric oxide to cutaneous microvascular dilation in individuals with type 2 diabetes

mellitus. *Am. J. Physiol. Endocrinol. Metab.* **292**, E314–8 (2007).

140. Gnyawali, S. C. *et al.* High-resolution harmonics ultrasound imaging for non-invasive characterization of wound healing in a pre-clinical swine model. *PLoS One* **10**, e0122327 (2015).

141. Tsukasaki, Y. *et al.* Synthesis and optical properties of emission-tunable PbS/CdS core–shell quantum dots for in vivo fluorescence imaging in the second near-infrared window. *RSC Adv.* **4**, 41164–41171 (2014).

142. Tuchin, V. V. Tissue Optics: Light Scattering Methods and Instruments for Medical Diagnosis. (2015) doi:10.1117/3.1003040.

143. Tuchin, V. V. *et al.* Light propagation in tissues with controlled optical properties. *Photon Propagation in Tissues II* (1996) doi:10.1117/12.260832.

144. Genina, E. A., Bashkatov, A. N., Sinichkin, Y. P., Yu. Yanina, I. & Tuchin, V. V. Optical Clearing of Tissues: Benefits for Biology, Medical Diagnostics, and Phototherapy. *Handbook of Optical Biomedical Diagnostics, Second Edition, Volume 2: Methods* doi:10.1117/3.2219608.ch10.

145. Hemmer, E., Benayas, A., Légaré, F. & Vetrone, F. Exploiting the biological windows: current perspectives on fluorescent bioprobes emitting above 1000 nm. *Nanoscale Horizons* **1**, 168–184 (2016).

146. Xue, Z., Zeng, S. & Hao, J. Non-invasive through-skull brain vascular imaging and small tumor diagnosis based on NIR-II emissive lanthanide nanoprobes beyond 1500 nm. *Biomaterials* **171**, 153–163 (2018).

147. Thiagarajah, J. R., Papadopoulos, M. C. & Verkman, A. S. Noninvasive early detection of brain edema in mice by near-infrared light scattering. *Journal of Neuroscience Research* vol. 80 293–299 (2005).

148. Shi, R. *et al.* A useful way to develop effective in vivo skin optical clearing agents. *J. Biophotonics* **10**, 887–895 (2017).

149. Zhu, D., Larin, K. V., Luo, Q. & Tuchin, V. V. Recent progress in tissue optical clearing. *Laser Photon. Rev.* **7**, 732–757 (2013).

150. Filatova, S. A., Shcherbakov, I. A. & Tsvetkov, V. B. Optical properties of animal tissues. *J. Biomed. Opt.* **22**, 35009 (2017).

151. Golovynskyi, S. *et al.* Optical transparence windows for head tissues in near and short-wave infrared regions. in *International Conference on Photonics and Imaging in Biology and Medicine* W3A.122 (Optical Society of America, 2017).

152. Li, N. *et al.* High spatiotemporal resolution imaging of the neurovascular response to electrical stimulation by in vivo temporal laser speckle contrast. *Journal of Neuroscience*

Methods vol. 176 230–236 (2009).

153. Hutchinson, E. B., Stefanovic, B., Koretsky, A. P. & Silva, A. C. Spatial flow-volume dissociation of the cerebral microcirculatory response to mild hypercapnia. *Neuroimage* **32**, 520–530 (2006).

154. Khan, M. H., Choi, B., Chess, S., Kelly, K. M. & McCullough, J. Optical Clearing of in Vivo Human Skin: Implications for Light-Based Diagnostic Imaging and Therapeutics [2]. (2004).

155. Wang, J., Shi, R. & Zhu, D. Switchable skin window induced by optical clearing method for dermal blood flow imaging. *J. Biomed. Opt.* **18**, 061209 (2013).

156. Optical Absorption of Hemoglobin. https://omlc.org/spectra/hemoglobin/.

157. Zonios, G., Bykowski, J. & Kollias, N. Skin melanin, hemoglobin, and light scattering properties can be quantitatively assessed in vivo using diffuse reflectance spectroscopy. *J. Invest. Dermatol.* **117**, 1452–1457 (2001).

158. Zhu, D., Wang, J., Zhi, Z., Wen, X. & Luo, Q. Imaging dermal blood flow through the intact rat skin with an optical clearing method. *J. Biomed. Opt.* **15**, 026008 (2010).

159. Ghaffari, H., Grant, S. C., Petzold, L. R. & Harrington, M. G. Regulation of cerebrospinal fluid and brain tissue sodium levels by choroid plexus and brain capillary endothelial cell sodium-potassium pumps during migraine.

160. Fowkes, F. G. R. *et al.* Comparison of global estimates of prevalence and risk factors for peripheral artery disease in 2000 and 2010: a systematic review and analysis. *Lancet* **382**, 1329–1340 (2013).

161. Khalil, Z., LoGiudice, D., Khodr, B., Maruff, P. & Masters, C. Impaired Peripheral Endothelial Microvascular Responsiveness in Alzheimer's Disease. *Journal of Alzheimer's Disease* vol. 11 25–32 (2007).

162. Costantini, I. *et al.* A versatile clearing agent for multi-modal brain imaging. *Sci. Rep.* **5**, 9808 (2015).

163. Li, H. *et al.* Disposable ultrasound-sensing chronic cranial window by soft nanoimprinting lithography. *Nat. Commun.* **10**, 4277 (2019).

164. Koletar, M. M., Dorr, A., Brown, M. E., McLaurin, J. & Stefanovic, B. Refinement of a chronic cranial window implant in the rat for longitudinal in vivo two–photon fluorescence microscopy of neurovascular function. *Sci. Rep.* **9**, 5499 (2019).